Alma Mater Studiorum – Università di Bologna

Dipartimento di Fisica e Astronomia
Corso di Laurea magistrale in Astrofisica e Cosmologia

Constraining FIR size, dust temperature and dust mass in ALPINE galaxies at redshift 4<z<6

Presentata da:
Michele Gavarente

Relatore:
Chiar.ma Prof.ssa Francesca Pozzi

Correlatori:
Dr. Francesco Calura
Dr. Quirino D'Amato

Anno accademico 2021/2022
Appello IV

Abstract

The study of galaxies at high redshift plays a crucial role to understand the mechanism of galaxy formation and evolution. At redshifts just after the epoch of re-ionization ($4 < z < 6$), we witness the transformation of galaxies from being newly-formed objects to mature and more complex structures. In a few hundred $Myrs$, galaxies increase their stellar mass, change their morphological type and progressively become more obscured due to increased dust attenuation of the UV light. In parallel, galaxies becomes luminous in the far-infrared (FIR) regime, where the photons absorbed in the UV/optical regime are absorbed by dust and thermally re-emitted. Therefore, determining physical parameters regarding dust, such as the size of the emitting region, its temperature and mass, is essential to trace the star formation rate (SFR) of galaxies and provide constrains on their star formation history.

The main purpose of this thesis is to determine the spatial extent of the dust emission in high-redshift galaxies and to provide a lower limit on dust temperature, to constrain the dust mass. This is achieved by studying 23 FIR-continuum detected main-sequence galaxies of the ALMA Large Program to INvestigate (ALPINE) survey, performed at high redshift ($4 < z < 6$). Moreover, we compare the spatial extent of the dust emission, i.e. the dust size, with the stellar and gas distribution, traced by the UV and [CII] emission, respectively. Finally, we put these results in a broader context, by studying the dust size evolution as a function of cosmic time.

We derive dust size measurements via a Gaussian fit in the image plane of the ALMA data, and for sources detected with a $SNR > 5$, we perform an additional Gaussian fit in the uv plane, which we find to be more accurate. Out of the 23 FIR-continuum-detected targets, 20 have been considered in this work since they are isolated systems. Of these 20, 7 are spatially resolved; for each of the remaining 13, we provide an upper limit to the dust size.

We find that the gas emission is more extended than the dust spatial scale, by a factor of 1.40 ± 0.29, while the latter appears to be larger than the stellar emission size. Moreover, we do not find any significant trend for dust size as a function of the stellar mass and the redshift. In addition, we provide a minimum dust temperature estimate for the 7 resolved sources, for which we find $T_{min,dust} \sim 16 - 19K$. We also derive dust masses for the resolved sources, $M_{dust} \sim 10^7 - 10^8 M_\odot$.

This thesis is structured as follows:

- In Chapter 1, we briefly provide a general view on some current open issues concerning galaxy evolution at high-z, emphasizing the importance of the determination of the physical parameters of dust;
- In Chapter 2, we present the various components of the interstellar medium, mainly focusing on the main features of dust;
- In Chapter 3, we present the basics of interferometry and the main features of the ALMA telescope. We also describe the imaging and fitting process, which are necessary to obtain size measurements;

- In Chapter 4, we introduce the ALPINE survey and describe in detail the source catalog used in this work. We also show the results of the fitting procedure;
- In Chapter 5, we present our results and we include them in an evolutionary context, by comparing them with other results from literature;
- In Chapter 6, we present the conclusions and consider future perspectives.

Contents

1 Introduction

1.1 Importance of the ISM in high redshift galaxies

Understanding galaxy formation and evolution is one of the most important goals in astrophysics nowadays. In the last two decades, thanks to new instrumentation and telescopes, it has been possible to investigate the emission and physical properties of galaxies from the epoch of re-ionization ($z > 6$, e.g. Zaroubi (2013)) to present times ($z = 0$). Among others, one major result is the measure of the star formation in galaxies across cosmic time, through the cosmic star formation rate density (SFRD, Madau et al. (2014)). Studying SFRD, where the star formation rate (SFR) defines the amount of stars produced in a unit of time and the SFRD is the SFR expressed in units of comoving volume, is crucial to understand the evolutionary history of galaxies, since it allows us to put constraints on models of galaxy evolution.

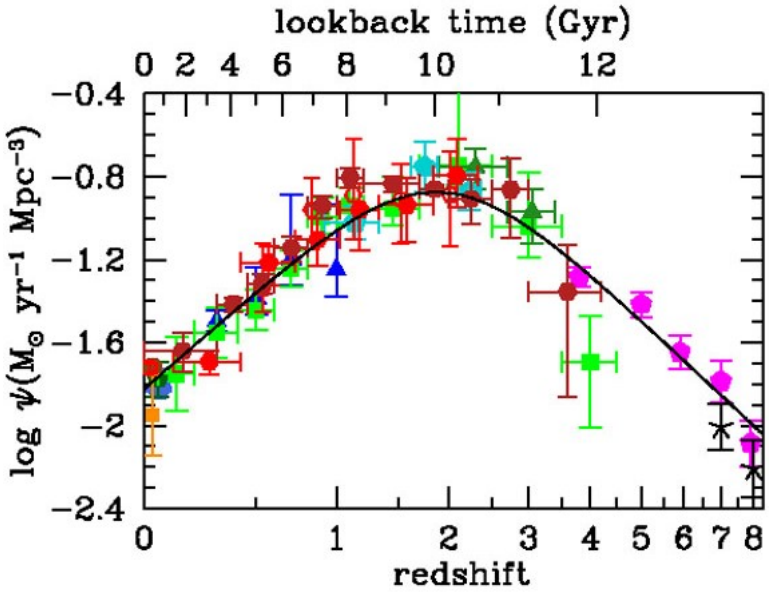

Figure 1: The rate of cosmic star formation measured in IR (in red) and UV (other colors) bands. The black curve is the best-fit of the SFRD (Madau et al. 2014).

As we show in Figure 1, Madau et al. (2014) found that the cosmic SFRD evolve through cosmic time, increasing from the epoch of re-ionization, scaling as $(1+z)^{-2.9}$, to peak at redshifts $z \sim 2-3$, when the Universe was just $2-3$ Gyr old, to eventually decline towards $z = 0$ as $(1 + z)^{2.7}$. The physical explanation of this trend for high redshift galaxies is not currently understood. The decline at $z < 2$ seems to be due to the exhaustion of star-forming gas in late-type galaxies (e. g. Francesco Calura et al. (2003), Bell et al. (2005)). In the local universe ($z \sim 0$), studies show that the SFR is mostly driven by a steady accretion of gas (Saintonge et al. 2022). The dominant processes that regulate the star formation are likely to strongly depend on redshift, as the relative roles of fundamental drivers, such as merging and cold gas accretion, are known to evolve with cosmic time (e.g, Fakhouri et al. (2010), Bouché et al. (2010)). To shed more light on these processes, it is crucial to constrain the evolution of fundamental galactic properties, such as their gas content and their

morphological properties.
Besides cold gas, interstellar dust is another component of the interstellar medium (ISM) that plays a fundamental role in driving galaxy properties. In star-forming regions, newly born stars are typically enshrouded in dust, which absorbs the incident optical/UV radiation emitted by massive stars, to then re-emit it in the far infrared band (see section 2.2.4). Therefore, star formation can be traced both via the UV and far-IR emission: this result is confirmed in both the local and distant Universe, where up to 90% of star formation activity may be obscured by dust (Hodge et al. 2020).

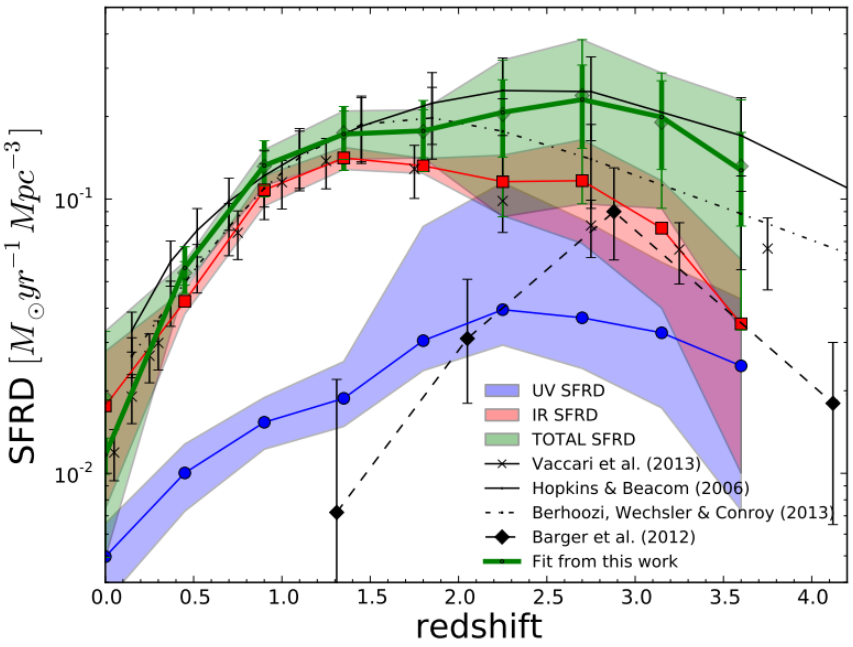

Figure 2: SFRD as a function of redshift; in the FUV, FIR and total (FUV+FIR), respectively shown in blue, red and green. Solid lines represent the mean values, while the colored areas are the associated uncertainties. The UV measurements are not corrected for dust-extinction. Figure taken from Burgarella et al. (2013).

As we show in Figure 2, recent studies revealed that a significant amount of dust was already present in galaxies at high redshift and that dust-obscured star formation was already the dominant contribution to the total SFRD at least up to $z \sim 3.5$ (Burgarella et al. 2013).
In addition, dust may also affect the star formation activity. Dust permits the formation of molecules, such as H_2 (i.e., the main fuel of star formation), on its surface, shielding them from dissociating UV radiation, hence, allowing for an increased star formation activity (Yamasawa et al. 2011, Asano et al. 2013).

1.2 Dust temperatures

As we explore in section 2.2.4, dust emits thermally, following the Planck's law, strictly related to its temperature. Therefore, the dust temperature (T_d) is a crucial parameter to determine the properties of the dust from its emission. Moreover, studying T_d may provide us with insights into the nature of dust-enshrouded energetic sources, such as massive stars or active galactic nuclei (AGN), and the processes determining dust formation and evolution.
Currently, many observations and models, carried out in redshift ranges between $0 < z < 8$, show an increase of T_d with redshift, as we show in Figure 3. How-

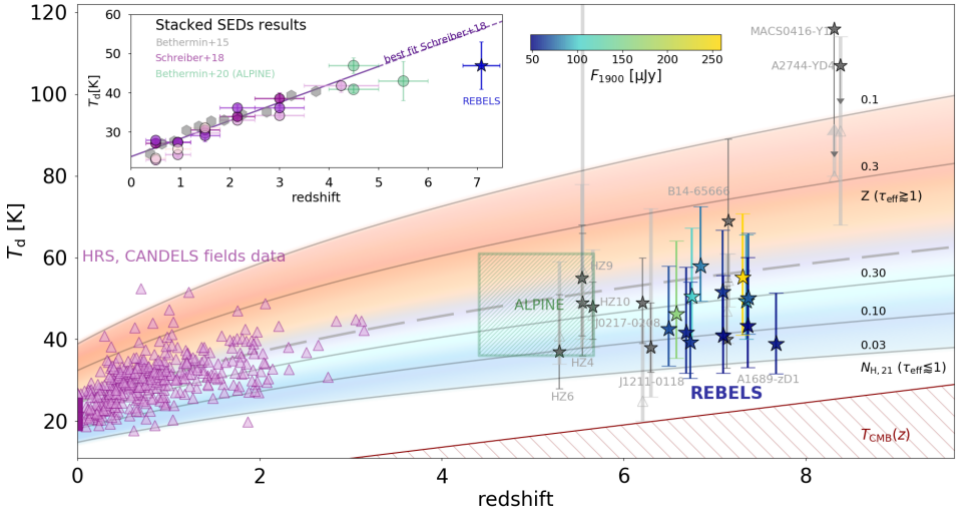

Figure 3: **Main panel**: Dust temperature over redshift. Low-z stacked SEDs are unpacked into single detections, shown in purple triangles, which are the UV-to-IR normal star forming galaxies detected in two fields: HRS and CANDELS Schreiber et al. 2018. Moreover, individual UV-selected galaxies at $z \lesssim 5$ for which T_d are estimated are shown in grey triangles and star (see table B1 of Sommovigo et al. (2022) for details). T_d estimate for continuum-detected galaxies from REBELS (Saintonge et al. 2022), which are color coded for their F_{1900}, and ALPINE (M. Béthermin et al. 2020) are shown in stars and green hatched rectangle, respectively. The coloured regions show the evolution of $T_d - z$ derive analytically via the equation 10-18 in Sommovigo et al. (2022). The increasing effective optical depth τ_{eff} is shown from blue to red regions. The grey dashed line represent the relation in equation 10 found in Sommovigo et al. (2022). The solid lines express the different values of column density $N_{H,21} = N_H/10^{21}$ or metallicity Z in the case of $\tau_{eff} \lesssim 1$ or $\tau_{eff}1$, respectively. **Main panel**: Dust temperature over redshift. T_d obtained by stacked SEDs fitting for $0 \leq z \leq 6$ from Matthieu Béthermin et al. (2015), Schreiber et al. (2018) and M. Béthermin et al. (2020) in grey, purple and green points, respectively. The purple line is the linear best fit gathered from Schreiber et al. (2018), for $z \lesssim 4$. The blue star is the average dust temperature $T_d = (47 \pm 6)K$ derived for REBELS galaxies. Figure taken from Sommovigo et al. (2022).

ever, the correlation is quite broad (see Figure 3) and, moreover, at high redshifts

($z > 5-6$) the results from different authors are different: in Bouwens et al. (2020), T_d seems to grow linearly with z, whereas in Andreas L. Faisst et al. (2020), the T_d tends to flatten for $z > 4$. Also the interpretation of the increase of the dust temperature with the redshift has in literature different explanations: in Hodge et al. (2016), the authors link the dust correlation with the redshift to the same trend shown by the specific star formation ($sSFR = SFR/M_\star$); cosmological simulations (see Pallottini et al. (2022)) explain the high dust temperature as due to the low dust-to-metals ratio at high-z ($z > 5$), since, for a given L_{IR}, a lower dust content results in warmer dust. Finally, others show that dust temperature is instead related to the dust spatial distribution (Sommovigo et al. 2020), where the temperature increase originates from the most compact star forming regions, where dust heating is much more efficient.
Moreover, the dust temperature measurements are not always accurate at high-z since, at $z > 5$, are often obtained by a single photometric-point in the FIR continuum, where dust emission occur (Saintonge et al. 2022). Hence, in certain works, dedicated to the measurement of the dust content, the dust temperature is assumed as prior (Pozzi et al. 2021, Magnelli et al. 2020), or estimated from the stacked far-IR SED of galaxies at high-z (see M. Béthermin et al. (2020)). Both these possibilities introduce a certain level of uncertainty in measuring T_d, with strong consequences on dust mass estimates, since they are strictly related to T_d.

A recent study (Sommovigo et al. 2022) introduced a new technique, combining continuum and [CII] line emission measurements in the FIR, to estimate more accurately T_d of galaxies at $z \sim 7$.
Nevertheless, high-resolution studies of the spatial distribution of dust and the ALMA sub-mm/mm observation of high-z galaxies in different bands, in order to better sample the galaxy far-IR rest-frame SED, will be key to constrain dust temperatures.

1.3 Dust masses

Dust mass represents a key physical quantity for the characterization of the early universe, particularly for constraining the amount of dust-obscured stellar emission. Many recent works have found that galaxies at high redshift ($z \sim 6$) already show significant amount of dust (e.g., Laporte et al. (2017), Tamura et al. (2019), Rodighiero et al. (2023)), up to $10^8 M_\odot$ (Leśniewska et al. (2019), see also Figure 4).

These results may imply that typical dust formation channels (AGB and evolved stars) cannot account for the observed amount of dust at high redshift, since it would take more time than the age of the universe at that epoch ($\sim 1Gyr$) to form it (e.g., Valiante et al. (2011), Ferrara et al. (2016)). One currently accepted model predicts that dust at high-z is mainly formed by supernova ejecta, caused by the rapid life cycle of massive stars and by non-stellar mechanisms, as the dust growth in the diffuse ISM (see F. Calura et al. (2017)). However, few studies of high redshift galaxies have been conducted to study the cosmic evolution of dust mass (Pozzi et al. 2020, Magnelli et al. 2020, Pozzi et al. 2021), therefore, to achieve a clearer view on this open issue, more observations at early epochs are required. More and more heavily obscured sources at very high redshift ($z > 10$) are being discovered

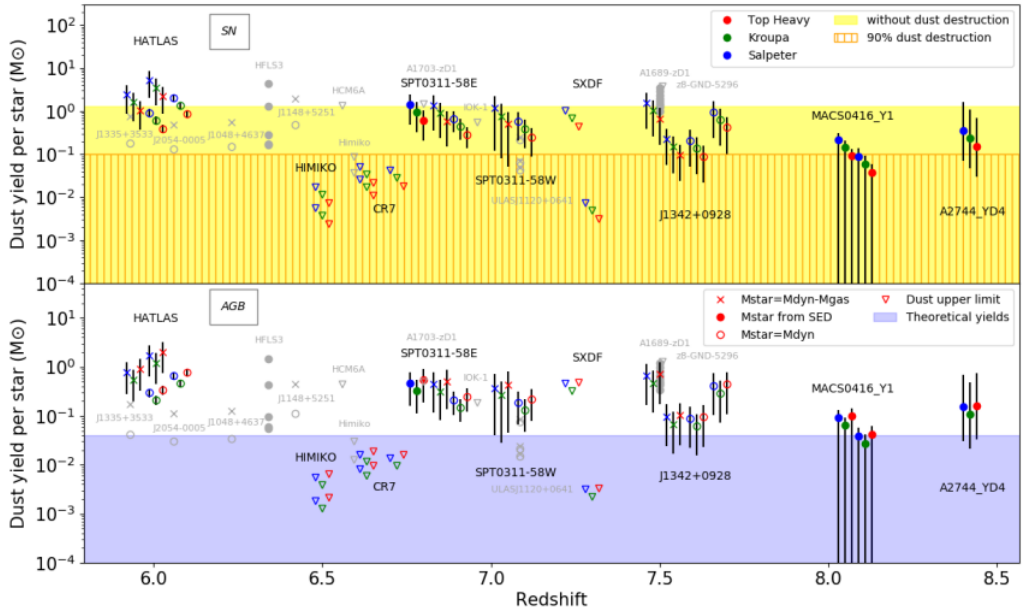

Figure 4: Dust yield for SN and asyntotic giant branch (AGB) star, respectively shown in the top a bottom panel, required to motivate the dust masses measured in Leśniewska et al. (2019). Three different initial mass function (IMF) are assumed: top-heavy, Kroupa and Salpeter in red, green and blue, respectively. Moreover, stellar mass were derived in three different ways: $M_{dyn} - M_{gas}$ (cross), M_{dyn} (open circle) and SED modelling (filled circle). Upper limits on dust masses are indicated by a downward triangle. Points with identical shape and color for a galaxy, correspond to distinct estimates of dust or stellar mass. Grey symbols show galaxies from Michałowski et al. (2010) and Madau et al. (2014). For the top panel, two regions have been defined: beneath the yellow region, the maximum theoretical dust yield without dust destruction of $1.3M_{\odot}$ is indicated, while under the vertical orange stripes is denoted the limit of $0.1M_{\odot}$ including $\sim$ 90% dust destruction. For the bottom panel, the theoretically permitted dust yields are shown in light blue .Figure taken from Leśniewska et al. (2019)

with the JWST (e.g., Rodighiero et al. (2023)), that will need to be confirmed in the FIR with ALMA.

1.4 Dust spatial extent

The study of dust sizes (i.e., generally intended as the effective radius $r_{e,FIR}$, which represents the radius containing half of the galaxy emission in the FIR continuum band) in high-z galaxies represents a crucial step in determining physical parameters such as the dust temperature and, consequently, dust masses. The study of the FIR continuum spatial extent of main-sequence (MS) galaxies at high-z was only made possible in recent times, thanks to the advent of new telescopes with high angular resolution and sensitivity, such as ALMA. Dust absorbs the radiation of young stars and re-emits it in the FIR continuum. Thus, studying the spatial extent of the dust emission in the FIR range provides important information about dust-obscured star

formation within galaxies.
Since the firsts results of high-resolution measurements with ALMA, the presence of compact dusty cores for galaxies at high redshifts was revealed (Fujimoto et al. 2017), confirming the suggestions of lower resolutions observations (Younger et al. 2008). However, a few discrepancies in these findings lie in their current physical interpretation. While these results have been suggested to be evidence for bulge growth and morphological transformation (Hodge et al. 2020), they may be dependent on the merger state. Moreover, in the few objects where individual merging components have been resolved, emission in the FIR was still associated with spatially small regions (Riechers et al. 2017). These findings are consistent with works that measured sizes from other SFR tracers, such via radio synchrotron (Ivison et al. 2002) and $[CII]/FIR$ ratio (Gullberg et al. 2018), confirming that dust sizes are relatively compact. Moreover, the spatial extent of the FIR emission, defined as the effective radius in the far-infrared $r_{e,FIR}$, may increase with luminosity in the infrared range, scaling as $r_{e,FIR} \propto L_{FIR}^{\alpha}$, with $\alpha = 0.28 \pm 0.07$ (Fujimoto et al. 2017).

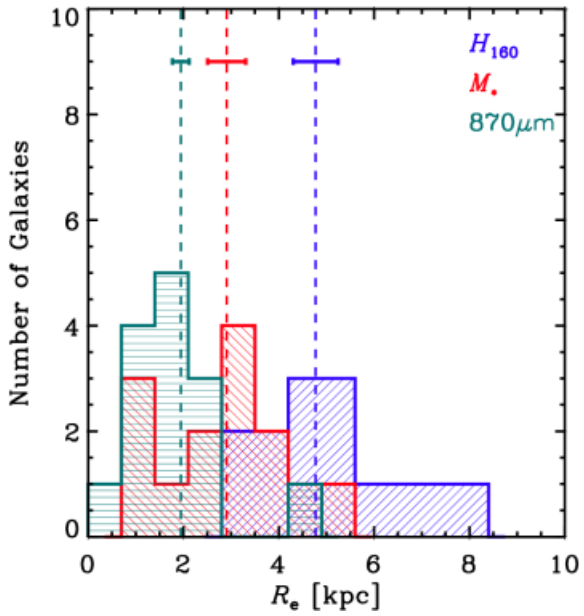

Figure 5: Histograms of effective radius measured in UV (H160-band), considering the stellar mass distribution and at 870μm, tracing the rest-frame FIR emission, in blue, red and green, respectively. Median sizes are indicated as vertical dashed lines; while horizontal error bars show the respective uncertainty on the median values. Figure from Lang et al. (2019).

Furthermore, since it is believed that the spatial distribution of the FIR emission traces the extent of the dust-obscured star formation, it is important to compare dust sizes with the spatial extent in the rest-frame optical/UV and with stellar mass tracers. A result on which numerous recent works seem to concur is that dust sizes are in general more compact than the rest-frame optical/UV ones (Hodge et al. 2016,Fujimoto et al. 2017). This is shown in Figure 5, where the authors studied the dust and stellar spatial extent of sub-millimeters galaxies (SMGs) at $z \sim 2$. This finding may be regarded as evidence of ongoing bulge formation, which may support

rapid morphological transformation (Hodge et al. 2020). However, some works do not confirm these results for FIR-fainter galaxies, which may find themselves at an evolutionary stage preceding bulge formation (Rujopakarn et al. 2016).
Also interesting it is the comparison of the dust sizes with the gas ones. Recent studies agree that the cool molecular gas, typically traced by the CO emission, for high-z galaxies, is more extended than the FIR continuum (Chen et al. 2017). While this result might suggest a varying dust-to-gas ratio across the galaxies, as found in local ones (Casasola et al. 2017), it may be also explained by a radiative transfer model, that links the dust continuum and the cool molecular gas. In this scenario, explored in Calistro Rivera et al. (2018), the small spatial extent of the dust emission might originate from a radial variation in the dust temperature and gas optical depth. The compactness of the FIR continuum emission is also observed with respect to the spatial extent of atomic gas emission, which, at high redshift, is generally traced by the fine-structure [CII] 158μm line. This result has found a consensus over a large number of studies (Gullberg et al. 2018, Fujimoto et al. 2019).

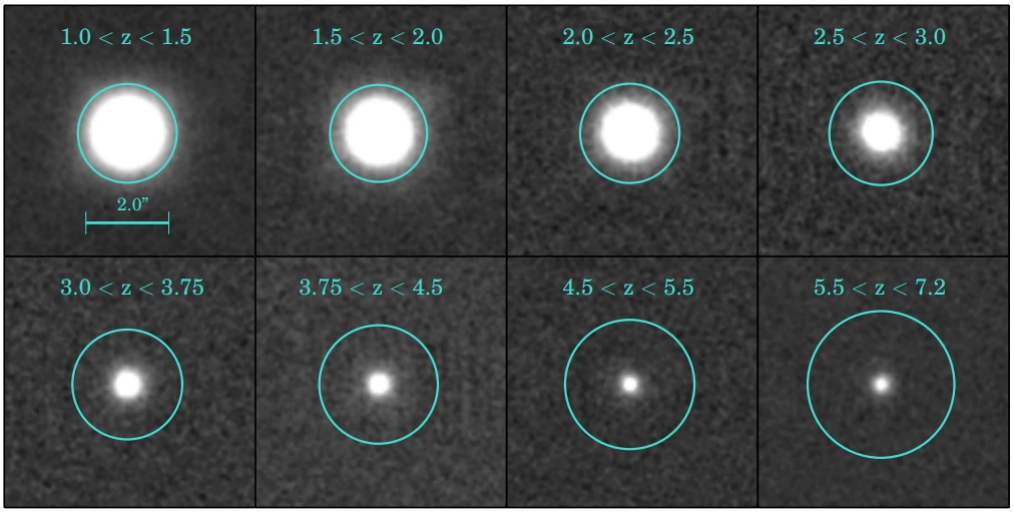

Figure 6: Stacks of galaxy images from HST/F160W CANDELS imaging, as a function of redshift, reported at the top of each panel. The cyan circles represent a circular region of diameter of 10kpc. Figure from Allen et al. (2017).

As discussed earlier, the study of the dust emission (its size, temperature and mass), is crucial to understand the physical properties of dust-obscured galaxies. However, the size of the dust emission of normal star-forming galaxies were made possible only in recent times at high-z, so few dust size studies exist for large redshift ranges ($0 < z < 6$). Moreover, techniques to derive dust sizes are different from each work thus a comparison might be challenging (Fujimoto et al. 2017).
Recent studies clearly show an evolution of optical/UV size over cosmic time (Allen et al. (2017), see also Figure 6), while there are some discrepancies in the literature regarding the dust sizes. While Wang et al. (2022) find no significant evolution over redshift for FIR continuum sizes of MS galaxies, Gómez-Guijarro et al. (2022) suggest that dust continuum sizes evolve with redshift. Therefore, the picture of dust sizes evolution is still unclear and further studies are necessary to investigate

this issue.

1.5 Motivation of the present work

The ISM plays a crucial in the study of galaxy evolution since it is strictly related to the cosmic SFRD, being the gas the fuel of the SFR. In particular, the interstellar dust strongly absorbs the UV/optical emission from stars, re-emitting the energy in the FIR regime. Hence, studying the dust properties is fundamental to achieve an unbiased view of the SFR. In this context, two quantities are crucial to be measured: the dust emission size and the dust temperature.

Concerning the measurements of the spatial emission of the dust, called dust size, in literature few and discordant results have been obtained. On one hand, since the firsts results of high-resolution measurements with the ALMA telescope, the dust continuum emission detected in galaxies in the submm/mm appears to be more compact than the stellar size (Hodge et al. 2016 ,Fujimoto et al. 2017, Rujopakarn et al. 2019), also confirmed by size measurements from other tracers such as CO lines (Puglisi et al. 2019) and radio emission (Jiménez-Andrade et al. 2019), both found to be more compact compared the stellar spatial extent. On the other hand, some works support a more extended dust continuum emission (Rujopakarn et al. 2016, Cochrane et al. 2021), confirmed also by simulations (see Popping et al. 2022). Therefore, the level of compactness of the dust-emitting regions of high-z galaxies is still uncertain.

Concerning the dust temperature, its measure is fundamental to provide insights into the nature of dust-enshrouded energetic sources, such as massive stars or active galactic nuclei (AGN), and the processes determining dust formation and evolution. While there is a general consensus regarding the evolution of dust temperature as a function of redshift (Matthieu Béthermin et al. 2015, Schreiber et al. 2018, Sommovigo et al. 2022) an accepted physical interpretation of this trend is still lacking: while some works suggest that warm dust might result from a more compact dust geometry in high-z galaxies (Sommovigo et al. 2020), cosmological simulations ascribe the increase in dust temperature to a low dust-to-metal ratio at high redshift (Pallottini et al. 2022). However, dust temperature measurements at high redshift are quite limited and derived from single point far-IR point measurements or by stacked spectral energy distributions (SEDs) (Tamura et al. 2019, M. Béthermin et al. 2020).

This thesis work aims to determine different physical parameters in high-z galaxies related to dust: size, temperature and mass. The studied galaxy sample belongs to the ALPINE survey (Le Fèvre et al. 2020, M. Béthermin et al. 2020, A. L. Faisst et al. 2020), an ALMA survey in Band 7 aimed to detect the [CII] and the FIR-continuum emission of UV-selected galaxies at $4 < z < 6$. The ALPINE survey is one of the few high-resolution studies of high-z MS galaxies, crucial for the study of galaxy evolution after cosmic reionization.

Therefore, the main goals of this work are:

- To derive the emission sizes of ALPINE galaxies in the FIR continuum, and then compare these results with the extension of the stellar and gas emission, the latter traced by the [CII] transition;
- To investigate the evolution of the dust spatial extent over cosmic time and stellar mass;
- To measure the minimum dust temperature of the ALPINE galaxies, to constrain galaxy models;
- To derive dust masses for ALPINE galaxies, from size and dust temperature measurements.

2 The interstellar medium

The ISM is all the matter found between stars and represents one of the most important components of a galaxy. Despite being only $\sim 5-10\%$ of the total mass of a galaxy, it plays a crucial role for the star formation and the recycling of matter and energy within the galaxy, hence, its study is fundamental to fully comprehend galaxy evolution. Moreover, studying its properties allows us to understand where and when star formation occurs within a galaxy.

Figure 7: Multiwavelength image of the andromeda galaxy. The top right panel probe the dust component of the ISM in the infrared regime, which traces the star formation regions. In the top left panel we can observe the optical emission of stars within the galaxy. The bottom right panel shows the X-rays sources of the galaxy: supernova remnants and binary systems. While the central panel combined the infrared and the X-ray emission, the bottom left panel combine the emission from stars, dust and X-ray sources. Credit: https://sci.esa.int/web/herschel/-/48182-multiwavelength-images-of-the-andromeda-galaxy-m31.

The ISM is found both in early-type (elliptical) and late-type (spiral) galaxies. While in early-type galaxies the ISM is typically diffuse all over the galaxy, in spiral ones the ISM is generally concentrated within a relatively thin gaseous disk, along the spiral arms, where the star formation occurs, as we show in Figure 7. The interstellar material is typically divided in two major components: gas, which represent 99% of the ISM mass, and dust, which is the solid state of the ISM and accounts for 1% of its total mass. In this section we will describe the main components of the ISM, focusing on the dusty component.

2.1 Gas

The gas in the ISM is composed almost entirely of hydrogen and helium, with hydrogen accounting for around 70% of the total mass, helium for 28%, and heavier

elements for the remaining 2%. Since helium is chemically inert, thus unable to form stable bonds, the interstellar gas is typically described only in terms of hydrogen. As discussed before, the ISM is typically found in every part of a galaxy, where physical conditions can change considerably: hence, the gas component of the ISM is usually described in terms of four distinct phases that depends on temperature and density, which we describe below (see Bruce T. Draine (2011)).

- **Hot ionized medium (HIM)**;
  This phase of the gas is the hottest in the ISM, reaching temperatures of $T \sim 10^6 - 10^7 K$, although having low densities, in the range of $n_e \sim 10^{-4} - 10^{-2} cm^{-3}$. It is mainly found in the bulges of spiral galaxies and more largely distributed in elliptical galaxies. These high temperatures are due to shocks fronts of supernovae explosions and strong stellar winds of young and massive stars, where the gas is collisionally ionized. It is typically referred as the hot corona of the galaxy since it can reach a vertical scale height up to $\sim 3kpc$. The hot gas present in the corona then cool down and eventually return to the disk, forming the so called 'galactic fountains' (see Fraternali (2017)). The main cooling mechanism of this very hot phase of the ISM occur via bremsstrahlung, mainly emitting in the X-ray/γ-rays due to these very high temperatures. The cooling timescale for bremsstrahlung emission is given by $t_{cool} \propto n_e^{-1} \cdot T^{1/2} yr$, hence for temperature and densities of the HIM, they may be as long as the Hubble time ($\sim 10^{11} yr$). However, when the HIM cools down to $T \sim 10^4 K$, recombination processes set up, with line emission from free-bound transition in the soft X-rays (C_{IV}, O_{VI}) and bound-bound transitions in the optical (H, He, C, O). In addition, the HIM is also traced by synchrotron radio emission of accelerated electrons from supernova remnants.

- **Warm ionized medium (WIM)**;
  This colder but still ionized phase of the ISM is typically associated with temperatures around $\sim 10^4 K$ and densities of $\sim 1 - 10^3 cm^{-3}$; indeed, $\sim 90\%$ of the total ionized gas of the ISM is located in the WIM. The WIM is related to process of photoionization: this ISM phase is mainly found in regions surrounding massive stars populations, typically of class O and B, which, due to their strong UV emission, are able to ionize the gas in their proximity, giving birth to the HII regions. The WIM also exits in regions of thermal equilibrium between photoionization and recombination processes, such as planetary nebulae. Additionally, the WIM is also found close to the galactic centers, where the UV radiation field is strong enough to photoionize the ISM. The WIM emits via bremsstrahlung, but at much lower energies than the HIM, mainly in the radio/infrared frequencies. However, the WIM can also cool via line emission from bound-bound transitions in the optical/UV of atoms/ions of high excitation ($[OIII], [SIII]$) and $H\alpha$ recombination.

- **Neutral medium**;
  The neutral medium is generally divided in two phases: the warm neutral medium (WNM) ($T \sim 10^2 - 10^4 K$, $n_e \sim 0.1 - 1 cm^{-3}$) and the cold neutral

medium (CNM) ($T \sim 10 - 10^2 K$, $n_e \sim 1 - 10^3 cm^{-3}$). However, there is evidence that the neutral medium is in a thermally unstable regime in the range of temperatures of the WNM and CNM, thus it is not possible to define two distinct phases. The neutral medium is composed by neutral hydrogen HI, organized in diffuse clouds, detected via a forbidden emission line at $\lambda = 21cm$. The $21cm$ line originates from the hyperfine structure of the hydrogen atom, where the spin flip of the electron relative to the proton in the atom's nucleus changes from the parallel state to the anti-parallel state. This transition is highly forbidden, with a typical timescale of $\sim 10^7 yr$, although, due to the high column density of the HI ($N(HI) > 10^{21} cm^{-2}$) it is possible to observe this emission. The HI is fundamental to detect emission from the whole galaxy disk, since it is present on the whole galaxy, filling 40% of the disk's volume. Moreover, it has been historically crucial to measure the rotation velocity of spiral galaxies, which provides an indirect evidence of the existence of the dark matter. In addition, the neutral medium is also traced by the emission line associated to the fine structure transition of the single ionized carbon ([CII]) at $158\mu m$. Due to its relatively low ionization potential ($\sim 11eV$), lower than the HI ($13.6eV$), the [CII] can be produced both in neutral and ionized regions. Moreover, its critical density ($\sim 10^3 cm^{-3}$) makes the [CII] emission line an important tracer of the ISM, in particular in high-z galaxies.

- **Molecular medium**;
  This represents the molecular phase of the ISM, thus molecular hydrogen H_2, with very low temperature $T = 10 - 20K$, but at the same time very high densities $n_e = 10^2 - 10^5 cm^{-3}$. The molecular hydrogen is organized in giant molecular clouds (GMC), that are gravitationally bound together, which are the site of star formation. The molecular medium is observed via the emission of rotational lines, due to rotational transitions of molecules, typically observed at radio/sub-mm wavelengths. While the H_2 is the most abundant molecule of this ISM phase, due its omonuclear nature, which does not permit dipole transition, it is rarely observable in the universe. Therefore, the molecular medium is typically studied using as tracer of the H_2 molecule the carbon-monoxide molecule, (CO) via its dipole rotational. At higher densities, so in inner regions of the GMC, other molecules are used, as the HCN and HCO+, since they have an high critical densities ($10^3 - 10^6 cm - 3$), and so the radiative de-exitation dominate over the collisional de-exitation also at high densities.

2.2 Dust

The dust is the solid state component of the ISM, mainly formed of grains, which are microscopic particles made of dieletric and reflective material. While dust represent only 0.1% of the total galaxy mass, it is able to absorb a large quantity of stellar emission ($\sim 30\%$), which will be re-emitted at longer wavelengths. Moreover, dust represent the main site for molecules formation i.e. H_2, the most abundant molecule in the universe, is though to be formed on the surface of dust grains. Additionally, its role may contribute to the formation of planetary systems and gas dynamics, being able to transmit radiation pressure produce by stars to the gas. Thus, the role of dust in astrophysics is fundamental for a coherent comprehension of galaxy emission and evolution.

2.2.1 Dust extinction

The extinction phenomenon occurs whenever radiation propagate through a medium containing small particles, such as dust grains. The transmitted emission is reduced in intensity by two physical processes: absorption and scattering.

We can then describe the process of extinction, considering the emission of a star intercepted by a dust cloud posed in front of the observer, as we show in figure 8.

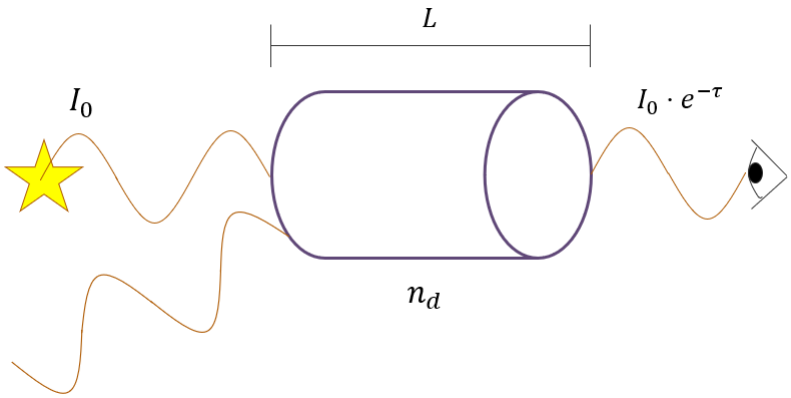

Figure 8: Simple schematization of dust absorption and scattering of incident radiation coming from a stellar source. The stellar radiation I_0 propagates through a cylindrical dust cloud of length L, with a grain number density of n_d. The stellar radiation that reaches the observer is then modified by an optical depth τ.

For simplicity, we assume that the dust grains can be interpreted as small spheres of radius a, of grain number density n_d, arranged in a cylindrical column of length L. The stellar emission I suffers a reduction in intensity dI due to extinction equal to:

$$\frac{dI}{I} = -n_d C_{ext} dL \tag{1}$$

where dL is an element of the cylindrical column and C_{ext} is defined as extinction cross section. The latter is an area which describes the amount of the incident beam that is effectively absorbed or scattered and is provided by the ratio of the total

energy absorbed per second and the energy incident per square meter per second. C_{ext} depends on the geometric cross-section, given by πa^2 and the optical properties of the dust grains.

Integrating the intensity I over the entire length of the dust cloud L, we find:

$$I = I_0 e^{-N_d C_{ext}} = I_0 e^{-\tau} \tag{2}$$

where I_0 is the intensity impacting the dust cloud at $L = 0$, $N_d = \int (n_d C_{ext})$ is the column density of the dust, so the total number of grains in the unit column, and τ is the dust optical depth.

It is possible to express the intensity reduction in function of magnitudes, thus the total extinction at a certain wavelength λ is:

$$A_\lambda = -2.5 \log \left(\frac{I}{I_0} \right) = -1.086 N_d C_{ext} \tag{3}$$

A_λ can be rewritten in as a function of the extinction efficiency factor Q_{ext}, obtained by the ratio of the extinction cross section C_{ext} and the geometric cross-section define above (πa^2):

$$Q_{ext} = \frac{C_{ext}}{\pi a^2} \tag{4}$$

Therefore, A_λ is given by:

$$A_\lambda = -1.086 N_d \pi a^2 Q_{ext} \tag{5}$$

However, in a more realistic case, if instead of spherical grains of radius a, we consider a size distribution such that $n(a)da$ (John S. Mathis 1997) is the number of grains per unit volume in the line of sight (l.o.s.), with radii from a to $a + da$, then A_λ is expressed as:

$$A_\lambda = 1.086 \pi L \int_a^{a+da} a^2 Q_{ext}(a) n(a) da \tag{6}$$

This way, we express the expected spectral dependence of extinction A_λ for a given grain model (with an assumed composition and size distribution), which only depends on Q_{ext}. Although, determine the latter is not trivial: the extinction efficiency is the sum of the single efficiency factor for absorption and scattering, defined as:

$$Q_{ext} = Q_{abs} + Q_{sca} \tag{7}$$

These efficiency factors both depends on two parameters:

- A dimensionless size parameter $X = 2\pi a/\lambda$, which compares the size of the grain with the wavelength of the incident radiation;
- A composition parameter $m = n - ik$, which is the complex refractive index of the dust grain material. If $n > k$, then the grain is an effective scatterer, while for $k > n$, the grain is an effective absorber, such as metallic grains

Thus, for any grain model (B. T. Draine et al. 2007), one may calculate the efficiency factors and compare these results with the total extinction observed. However, to obtain Q_{abs} and Q_{sca} one shall resolve the Maxwell's equations for an incident wave, for an object of specified size and shape, composed of material with a refractive index m. Mie and Debye, in 1908 and 1909 respectively, proposed a solution to this problem, in the special case of a homogeneous spherical particle, giving birth to the Mie theory. The latter suggest that the electromagnetic field inside and outside the sphere can be decomposed into spherical harmonics with an appropriate radial functions, with coefficients that must satisfy the continuity conditions at the surface of the sphere. There are two limit cases that can be treated:

- **Rayleigh scattering**:
  This is the case for an incident emission of wavelength much larger than the size of the dust grain (i.e. $X << 1$). Considering the simplified case of null absorption, the extinction factor is defined as:

$$Q_{ext} \approx Q_{sca} = \frac{8}{3} \cdot \left| \frac{(m^2 - 1)}{(m^2 + 2)} \right|^2 \cdot X^4 \tag{8}$$

  where, using the definition of X, the scattering factor depends weakly on the incident wavelength:

$$Q_{sca} \propto \lambda^{-4} \tag{9}$$

  Now, if we take into consideration an absorption term ($Q_{abs} > Q_{sca}$), the absorption factor is described by:

$$Q_{abs} \approx 4 \cdot Im \left[\frac{(m^2 - 1)}{(m^2 + 2)} \right] \cdot X \tag{10}$$

  where, again using the definition of X:

$$Q_{abs} \propto \lambda^{-1} \tag{11}$$

  Thus, in this regime, absorption is the dominant factor.

- **Mie scattering**:
  In this case, the grain size is much larger than the incident radiation (i.e. $X >> 1$). Again considering no absorption, the extinction factor may be written as:

$$Q_{ext} \approx Q_{sca} = 2 - \frac{4}{\rho} \sin \rho + \frac{4}{\rho^2} (1 - \cos \rho) \tag{12}$$

  where $\rho = 2x(m - 1)$. Thus, Q_{ext} is dependent on an oscillatory term, related to X, as we show in Figure 9. The maximum of this oscillation occurs when the twice-refracted light passing through the grain, interferes with the light

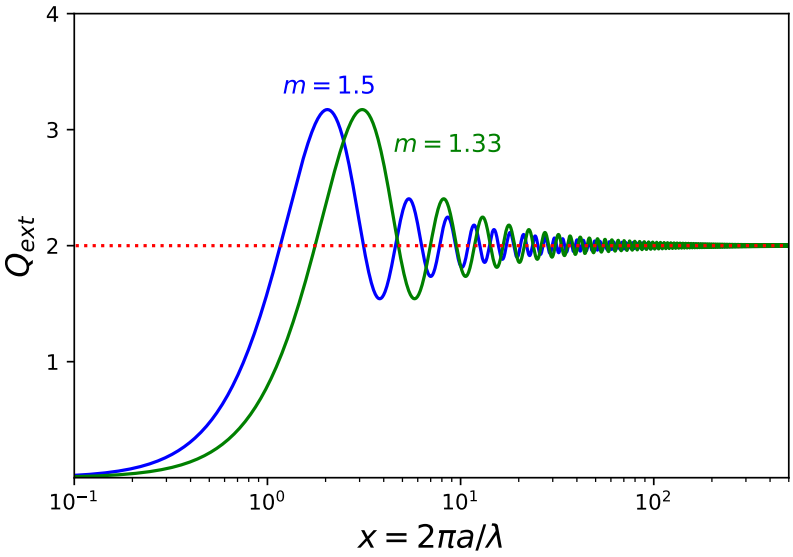

Figure 9: Plot of the extinction efficiency in function of X for materials with different refraction index m.

diffracted around the particle. The position of the peak depends also on the refraction index as $1/(m-1)$, representing the resonance between the incident radiation and the dipole moment of the particle. Moreover, as X tends to larger value, $Q_{ext} \sim 2$. This is the Babinett's principle, which affirms that the diffraction pattern from an object is equal to the one from an aperture of identical cross-section.

However, these results do not take in consideration the angular dependency of various parameters such as the location of the source, the position of the observer and the scattering grains, that greatly influence the intensity of the scattered radiation. To simplify this complex geometrical problem, it is possible to describe the angular dependence of scattering intensity in two parameters:

- The albedo $\omega = Q_{scat}/Q_{ext}$, where, for an ideal pure-scattering grain, $\omega = 1$, while, for a completely absorbing grain, $\omega = 0$;
- The mean value of the cosine of the angle of scattering $g(\theta) = \langle \cos\theta \rangle$, where, for an isotropic scattering ($X << 1$), $g = 0$, while, for a forward only scattering, $g = 1$.

In a realistic case, one must consider different angle of the incident emission, which corresponds to a multitude of distinct extinction that depends on wavelength. This is called extinction law, typically expressed as the ratio of two different colors or in units of magnitudes: $E(\lambda - V)/E(B - V) = (A_\lambda - A_V)/(A_B - A_V)$, where A_B and A_V are the absorption in the photometric band B (4300 Å) and V (5500 Å), respectively.

An additional parameter that is commonly used to describe the extinction is $R_V = A_V/E(B - V)$. R_V represent the relative slope of the extinction curve, which

can provide information on the grain properties. Typical values of R_V ranges from 2 to 6, far from the ideal case (see Figure 9).

To infer extinction curves, typically spectra of two stars that belongs to the same spectral class are compared, where only one is affected by extinction along the line of sight. Moreover, for extragalactic sources, it is possible to estimate the dust extinction law when a foreground galaxy overlaps a background galaxy or through gravitationally-lensed QSOs, assuming a time-independent intrinsic spectrum (B. T. Draine 2003).

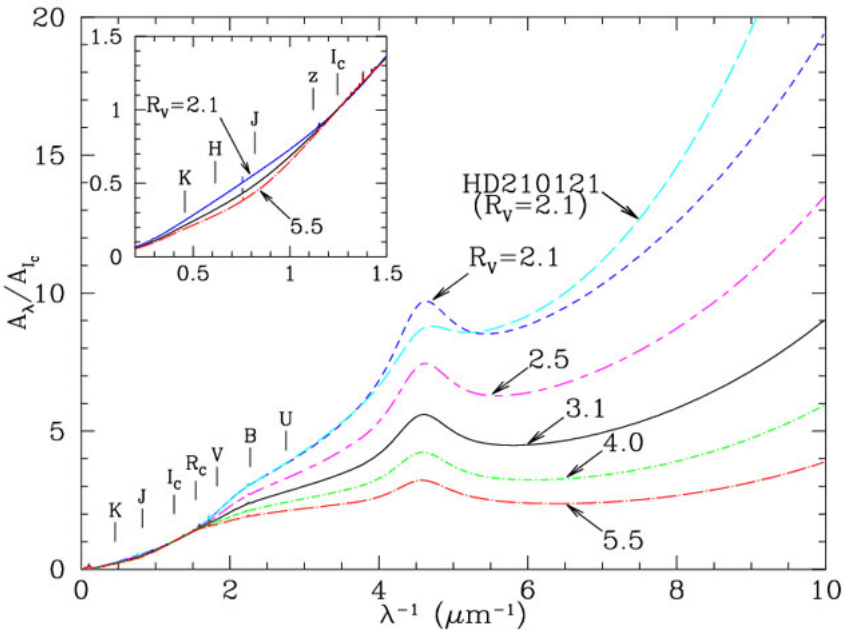

Figure 10: Plot of different extinction curves over λ^{-1} for different values of R_V, ranging from 2 to 5.5. In cyan, it is shown a fit for the extinction curve toward HD210121 (a B3V background star), which demonstrate the influence of a different l.o.s. on the typical extinction curve, for the same value of R_V. In the upper left, is shown a zoom of the curves for IR wavelengths. Figure taken from B. T. Draine (2003).

There are several parameters that influence the trend of the extinction curve, fundamental to understand the composition and structure of dust grains:

- **Total hydrogen column density**;
  The general continuous structure of the extinction curve along the l.o.s. is strictly related to total column density of hydrogen N_H. This results was already found in 1978, where, using both the HI $Ly\alpha$ and H_2 Lyman-Werner bands in the UV, it was derived a conversion factor between the total visual extinction A_V and N_H:

$$\frac{A_V}{N_H} \approx 5.35 \cdot 10^{-22} mag \cdot cm^2 \tag{13}$$

  although, more recent results (Güver et al. 2009) find a smaller value:

$$\frac{A_V}{N_H} = 4.52 \pm 0.18 \cdot 10^{-22} mag \cdot cm^2 \tag{14}$$

However, there are two factors to take into account: for first, this ratio is not universal and depends on the value of R_V, thus one can perform an empirical fit on the observed data and express it as a function of R_V. Secondly, accurate estimates of this value can only be made for rather close objects, usually inside our galaxy and in the local group, such as the large and small magellanic clouds.

- **The 2175 Å bump**;
  This is the strongest spectral feature in the extinction curve, observed as a broad bump at a $\lambda = 2175 \pm 50$. This feature is observed in almost all extinction curves, thus the absorber must be abundant and sufficiently robust to survive in different environments. At the present time, it is still unclear who produces this phenomenon, but several candidates have been proposed. While some studies have suggested that non-carbonaceous elements may produce this effect, such as OH^- on small silicate grains, it is currently believed to be abscribed to carbon-rich particles, either in the form of graphite, hydrogenated amorphous carbon grains, or various aromatic forms of carbon.

2.2.2 Dust components and sizes

Cosmic dust is composed of single dust grains or aggregates of them, irregularly shaped and typically compact or porous, as we show in Figure 11. They are though to be formed by refractional materials, arranged in a rocky core, made of silicates and carbonaceous, or a metallic core, such as an iron sphere, covered by a layer of ice composed of volatile compounds like water or CO_2 condensed on the core's surface. Moreover, on dust's grains surface are also present molecules, as we show in Figure 12. It is possible to determine dust's grain composition either by directly measuring its components, studying comet and meteoric dust, or by reproducing the observed extinction curve considering a mixtures of grain with each a specific refraction index.

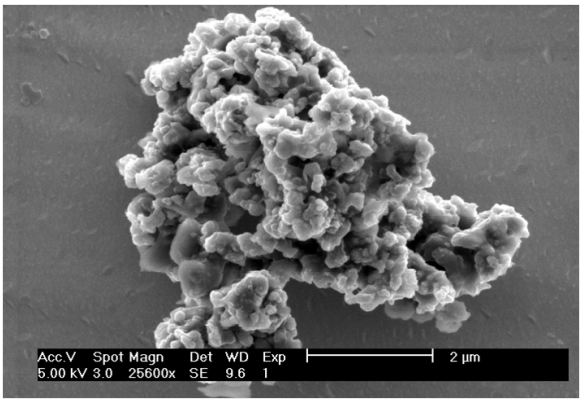

Figure 11: A typical chondritic porous interstellar dust particle of a few micrometers, composed of mineral grains and organic matter. Credit: https://earthandsolarsystem.wordpress.com/2011/06/14/interplanetary-dust-a-sneaky-way-to-study-comets/

From these observation, it was found that the majority of interstellar dust is made of a mixture of silicate grains, at 5% crystalline, formed from compounds with iron and magnesium, and 95% amorphous, and carbonaceous grains. These ones include pure carbon in crystalline form, such as diamonds and graphite, amorphous form and hydrocarbons in the form of hydrogenated amorphous carbons and PAHs. Moreover, a small percentage of interstellar dust is made by other carbonaceous material such as silicon carbide (SiC) and carbonates like calcite ($CaCO_3$). Dust grains are typically assumed to be spherical, however observations of polarized starlight passed through dust grains shows that grains cannot be spherical. This has serious implication in grain dynamics and molecular formation on grain surfaces, since a non-spherical shape allows for larger surface area thus increasing molecular formation. Grain sizes

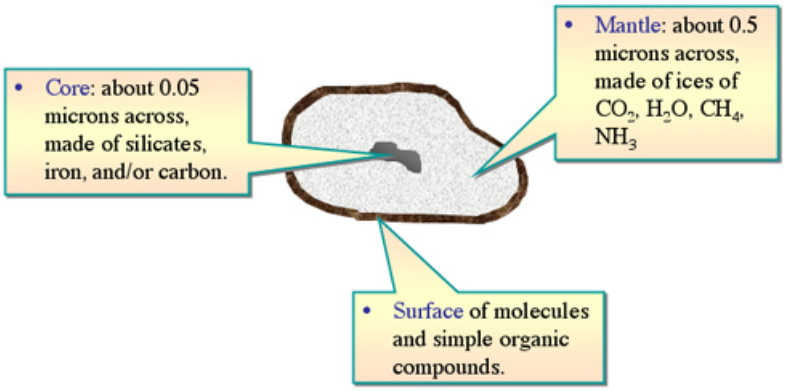

Figure 12: Simple representation of the structure of an interstellar dust grain. Credit: https://astronomy.swin.edu.au/cosmos/d/Dust+Grain/

are various and are typically defined assuming a power-law size distribution since dust is made of various dust grains and the detailed extinction curve cannot be made by only one size. Grain sizes are then described by the MRN mixture proposed by Mathis, Rumpl and Nordsieck, which follow the law (J. S. Mathis et al. 1977):

$$N(a) \propto a^{-\beta} \tag{15}$$

with grain sizes ranging from $a_{min} = 0.005\mu m$ to $a_{max} = 1\mu m$ and $\beta = 3.5$.

2.2.3 Dust formation and destruction

Dust grains are formed in two steps: first, the phenomenon of nucleation occurs, where solid materials can condense out of the gas phase, forming a stable nucleus. This process is crucial to quickly form dust grains, where the characteristic timescale of nucleation is around $10^6 - 10^9 sec$. Secondly, the grain's growth via the accretion onto the nucleus of the ambient gas, atoms or molecules is responsible of creating macroscopic dust grains (Demyk 2011).

Figure 13 shows a schematization of the life cycle of dust in the ISM. Dust can be mainly produced by a variety of sources in the universe. The main contributor to cosmic dust is thought to be evolved stars, in particular asymptotic giant branch (AGB) stars, thus stars with initial masses in the range of $0.8 < M/M_\odot < 8$.

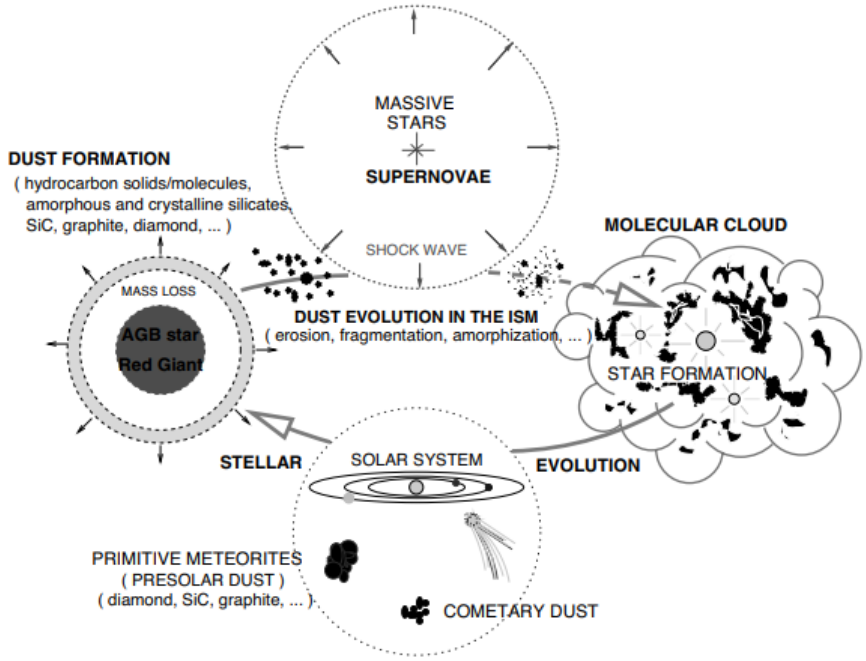

Figure 13: The life cycle of dust in the ISM. Figure taken from A. P. Jones (2004).

During their late stages of stellar evolution, AGB stars undergo a pulsating phase, ejecting dense cool shells of gas from their surface, allowing the formation of dust grains via the process of condensation. The composition of dust produced by this mechanism depends on the abundances of heavy materials in the outermost layers of stars, generally expressed as the ratio between oxygen and carbon (O/C) (Demyk 2011). In the oxygen rich scenario ($O/C > 1$), the majority of carbon atoms forms CO thus dust grains are mainly made of silicates, showed by a strong $10\mu m$ silicate feature in their spectra. In the carbon rich scenario ($O/C < 1$), dust grains are formed by carbonaceous solids such as graphite and amorphous carbon. However, also core collapse supernovae (SNII), where ejecta from SN explosion of high-mass stars ($M > 8M_{\odot}$) may form dust.

However, dust yields from this process are still unconstrained: while observations of the remnant of the SN1987A showed produced dust masses up to $0.2M_{\odot}$ (Indebetouw et al. 2014), other studies measure much lower dust masses, of the order of $10^{-5} - 10^{-3}M_{\odot}$ (Demyk 2011). There are also mechanism that destroy dust in the ISM, where the most significant one is called sputtering. In this process, atoms that make up the dust grains are ejected due to collisions with incident atoms or ions with energies $10eV/nucleon$, provided by SN-generated shock waves (A. P. Jones 2004). However, other processes can lead to dust destruction or alter dust composition such as the photolysis of ice mantles and surface coatings by UV starlight (B. T. Draine 2003).

2.2.4 Dust thermal emission

As discussed earlier, dust grains can scatter or absorb and be heated by incident radiation. In this case, the dust grains reach thermal equilibrium with the incident

radiation field and is heated at a certain temperature T_d, which depends on size and composition of dust grains, and therefore emitting black body radiation. While dust could be heated either by collisional processes with atoms or other dust grains or by energy absorption produced by molecular reactions of molecules that form on grain surface, in an intense radiation field, the most efficient process process is photon absorption through radiative heating.

When the photon is absorbed, the dust grain is left in an excited state, with a probability of $10^{-7}s^{-1}$ to re-emit the photon spontaneously. However, grains are made of complex molecules that have many excited states, which can redistribute the energy of the absorbed photon into internal vibrational states, heating the grain, in $10^{-12}s$. Since the product of the spontaneous emission probability and the vibrational redistribution results in a timescale of 10^{-5}, the majority of the absorbed photons will efficiently heat the dust grains. After being heated, grains can cool by collisions or by sublimation, however, the dominant cooling channel is the radiative one, which establishes thermal equilibrium, emitting thermal photons. Now, considering a spherical dust grain with radius a, at a distance d from a star with luminosity $L_\nu(*)$, we can express the thermal equilibrium condition through the balance between the energy absorbed by the grain and the thermal energy radiated by the dust ($W_{abs} = W_{em}$) with the thermal equilibrium equation:

$$\pi a^2 \int_0^\infty \frac{L_\nu}{4\pi d^2} Q_{abs}(\nu) d\nu = 4\pi a^2 \int_0^\infty F(\nu) d\nu \tag{16}$$

The left side represents the energy absorbed by the grain, given by the energy emitted by the star and the effective absorption $Q_{abs}(\nu)$. The right side is the thermal energy emitted by the dust, that depends on the size of the grain and the emitted spectrum. The latter can be expressed as function of the Planck's function ($B_\nu(T_d) = \frac{2h\nu^3}{c^2}(e^{\frac{h\nu}{\kappa_B T_d}} - 1)^{-1}$), due to Kirchoff's law, and the absorption coefficient Q_{abs}:

$$F(\nu) = \pi I(T_d) = \pi B_\nu(T_d) Q_{abs} \tag{17}$$

The absorption coefficient is related to the optical depth τ_ν, thus the dust emitted spectrum can be expressed as a grey body emission or modified black body (MBB):

$$F(\nu) \propto B_\nu(T_d)(1 - e^{-\tau}) \tag{18}$$

The absorption coefficient can also be expressed as a function of wavelength, $Q_{abs} \propto \lambda^{-\beta} \propto \nu^\beta$, where β is an index that depends on the grain composition: $\beta = 1$ for amorphous material and $\beta = 2$ for crystalline grains. Hence, since stars mainly emit in the UV/optical/near infrared range, grain absorption is preferred at those frequencies, however, most of the dust emission occur in the mid to far infrared range, due to dust temperature in the range of $T_d \sim 10 - 100K$. Now, recalling equation 16, it is possible to explicit the dust grain temperatures by assuming average values of $\langle Q_{UV} \rangle$ and $\langle Q_{IR} \rangle$, respectively, the absorption and emission coefficients in the UV and IR, therefore, considering the Stefan-Boltzmann equation $F = \sigma T^4$, where σ is the Stefan-Boltzmann costant:

$$T_{gr} \approx \left(\frac{\langle Q_{UV} \rangle}{\langle Q_{IR} \rangle} \right)^{1/4} \left(\frac{L_\star}{16\pi\sigma d^2} \right)^{1/4} \tag{19}$$

where the temperature of the grains is inversely proportional with the distance from the star. The average emission coefficient in the IR ($\langle Q_{IR} \rangle$) is typically function of the grain size a and their temperature T_{gr}: therefore, expressing the grain emissivity as $Q_{em} \propto \nu^{\beta}$:

$$\langle Q_{IR} \rangle \approx (2 \cdot 10^{-3} a T_{gr})^{\beta} \tag{20}$$

Hence, the total IR flux obtained by the dust is $F_{TOT,IR} \propto \pi B_{\nu}(T_{gr}) \propto T_{gr}^{\beta+4}$, which will be much steeper than the emission of a perfect blackbody. From equation 20, it is clear that the grain temperature depends on the emissivity index β: indeed, for higher β, the grains are less efficient at emitting at lower frequencies, thus shifting the emission peak at higher frequencies.

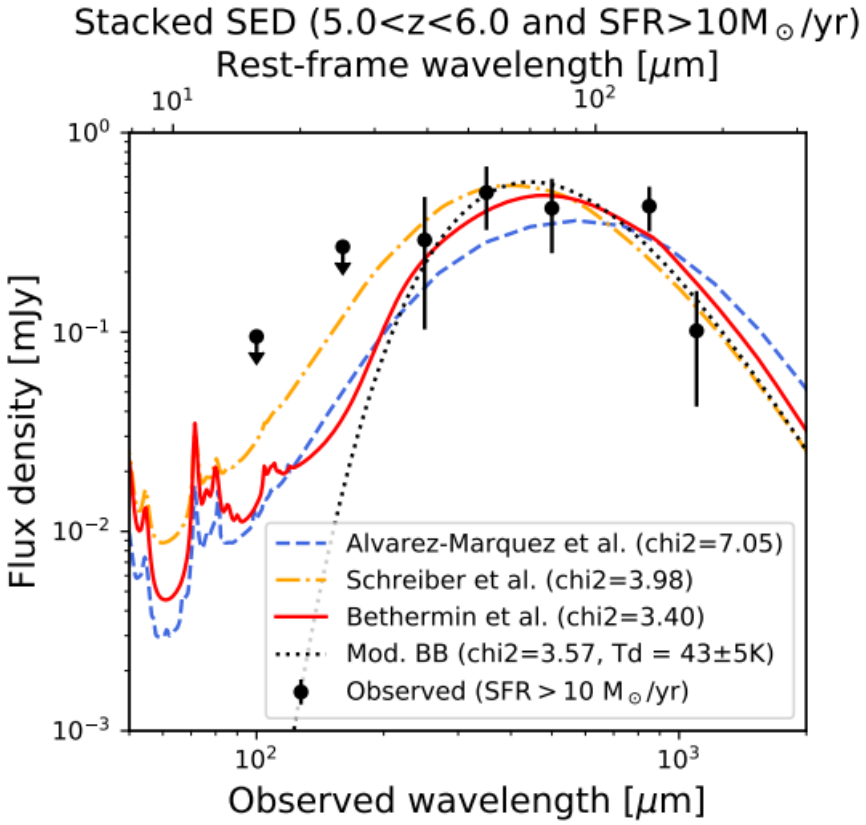

Figure 14: Stacked SEDs for high-z galaxies ($5 < z < 6$) with $SFR > 10 M_{\odot}$ obtained by IR SED templates and observed mean SEDs in blue, orange and red for Álvarez-Márquez et al. (2016), Schreiber et al. (2018) and Matthieu Béthermin et al. (2017) respectively. The black dotted line is the best fit of the $\lambda_{rest-frame} > 40 \mu m$ for a modified black body model. Figure taken from M. Béthermin et al. (2020)

To model the total dust emission in galaxies, one shall consider all the different parameters that characterize dust such as its composition, its size and additionally the intensity of the background field. While this is rarely done (see B. T. Draine et al. (2007)), the usual approach is to assume that the dust spectrum is produced, in the FIR, by a MBB at a single dust temperature for all the dust grains (Burgarella

et al. 2013). Using the full radiative transfer equation the observed flux density is expressed as (Weiß et al. 2007, Walter et al. 2022):

$$F_{\nu_{obs}} = \Omega[B_\nu(T_d) - B_\nu(T_{CMB})](1 - e^{-\tau_\nu})(1+z)^{-3} \tag{21}$$

where $F_{\nu_{obs}}$ is the flux at the frequency of the observation ν_{obs}, Ω is the solid angle covered by the source, $B_\nu(T) = \frac{2h\nu^3}{c^2}(e^{\frac{h\nu}{\kappa_B T}} - 1)^{-1}$ is the Planck function at a temperature T, $T_{CMB}(z) = 2.725(1+z)K$ is the cosmic microwave background (CMB) temperature at a redshift z, τ_ν is the dust optical depth and ν is the rest-frame frequency ($\nu = \nu_{obs}(1+z)$). As we show in Figure 14, a MBB at a single dust temperature does not always approximate well the SED in the FIR, in particular at high-z, due to the few photometric points that can be obtained via observations. However, a more accurate result would involve considering two (or more) different MBB at different dust temperatures, e.g., a cold component, heated by the diffuse field, and a warm one, provided by heated grain close to stellar emission.

3 Methods & data analysis

3.1 A brief look into interferometry

Interferometry is a technique used by in radio and sub-mm/mm telescopes to capture the light coming from the faintest and smallest objects in the universe. Their basic functioning can be described by considering the simplest interferometer possible: the two-element multiplying interferometer, composed by only two antennas. This can be easily implemented in the case of an array of N antennas taking into consideration $N(N-1)/2$ unique baselines. Additionally, in this exemplification, a multiplying correlator is considered, which multiplies and creates a time average of the signal detected by the two antennas. Figure 15 shows this model, where the two antennas, separated by a baseline $\vec{b}$, observe the same source in the sky, where its direction is given by the vector $\hat{s}$, with a certain angle θ with respect to the baseline (Condon et al. 2016).

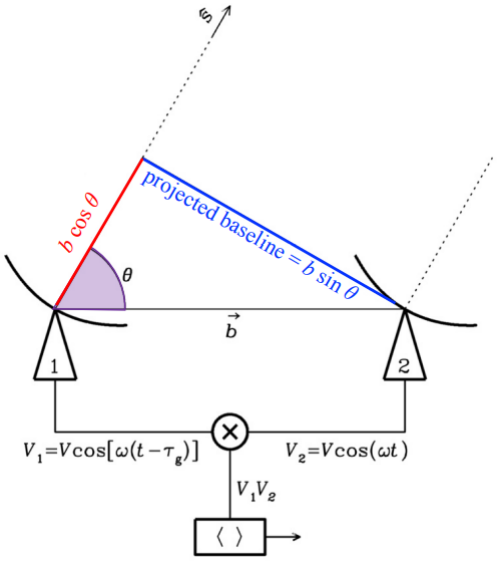

Figure 15: Two element interferometer model that points towards a target in the direction given by the vector $\hat{s}$. The voltages produced by the two antennas are then multiplied ($\times$) and time averaged ($\langle\ \rangle$) by the correlator. Figure taken from https://science.nrao.edu/facilities/alma/naasc-workshops/nrao-cd-ru17/InterfBasics$_R$*ice.pdf*.

The two antennas receive from the target a signal, that originates two oscillating voltages defined as V_1 for the first antenna and V_2 for the second one. These two voltages differs from one another for a geometric delay, given by the additional path that the signal must cross to reach the antenna 1, defined as $\tau_g = b \cdot cos\theta/c$. This geometric delay must be taken into consideration to keep the signal coherent. Considering a quasi-monochromatic interferometer, that responds to radiation in a very narrow band $\Delta\nu << 2\pi/\tau_g$, centered on frequency $\nu = \omega/(2\pi)$, the output voltages of the two antennas at a certain time t are (Condon et al. 2016):

$$V_1 = V cos[\omega(t-\tau_g)] \quad \text{and} \quad V_2 = V cos[\omega(t)] \tag{22}$$

that are sent to the correlator, which multiplies voltages V_1 and V_2:

$$V_1V_2 = V^2 cos[\omega(t-\tau_g)]cos(\omega t) = \frac{V^2}{2}[cos(2\omega t - \omega\tau_g) + cos(\omega\tau_g)]^1 \quad (23)$$

The correlator also makes a time average Δt such as $\Delta t >> (2\omega)^{-1}$, to remove the rapidly varying term $[cos(2\omega t - \omega\tau_g)]$, therefore obtaining the output voltage, or correlator response R:

$$R =< V_1V_2 >= \frac{V^2}{2} cos(\omega\tau_g) \quad (24)$$

These voltages are proportional to the electric field produced by the source, multiplied by the voltage gains of the antennas: thus the correlator output amplitude is proportional to the flux density of the source S (Condon et al. 2016):

$$R \propto V^2 \propto S \times (A_1A_2)^{1/2} \quad (25)$$

where A_1 and A_2 are the effective collecting areas of the two antennas.

The motion of the target onto the sky plane brings a variation of θ, so the signal's delay that appears on the antenna 1 constantly changes, thus the correlator response R varies sinusoidally with time. These sinusoidal variations are called fringes.

The phase of the fringes ϕ, which is the relative phase between the signals received at the antenna 1 and the antenna 2, depends on the geometric delay τ_g and λ:

$$\phi = \omega\tau_g = 2\pi\nu\tau_g = 2\pi\nu\frac{bcos\theta}{c} = 2\pi\frac{b}{\lambda}cos\theta \quad (26)$$

The correlator response R to a point source can be then expressed as:

$$R = \frac{V^2}{2}cos(\phi) = \frac{V^2}{2}cos\left(2\pi\frac{b}{\lambda}cos\theta\right) \quad (27)$$

Though, the voltage pattern of individual antennas must be taken into consideration, which, for identical antennas, is given by their own power pattern. This is called primary beam of the interferometer, which is equal to the square of the *sinc* function[2]. The response of the interferometer $P(\theta)$, also called dirty beam, is then given by:

$$P(\theta) \propto sinc^2\left(\frac{D}{\lambda}cos\theta\right) cos\left(2\pi\frac{b}{\lambda}cos\theta\right) \quad (28)$$

thus it is the multiplication of the power pattern of the individual antenna with the correlator response to a point source. In other terms, the cosine function obtained by the correlator response is modulated by the *sinc* function squared. The outcome of the correlator will then be the true sky brightness distribution convoluted by the antenna pattern. A visualization of the interferometer response to a point source, in polar coordinates, is shown in figure 16.

Due to the effect of the *sinc* function, the brightness of the point source is seen by the interferometer as one main lobe followed by secondary lobes of lower intensity.

[1] This is true for to the trigonometric identity $cos(x)cos(y) = [cos(x+y) + cos(x-y)]/2$

[2] $sinc(x) = \frac{sin(x)}{x}$

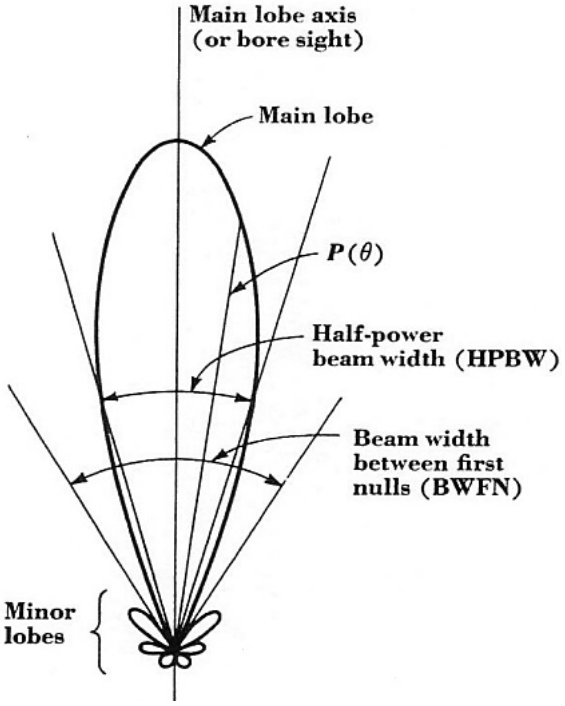

Figure 16: Interferometer response to a point source in polar coordinates. Credit - https://science.nrao.edu/science/meetings/presentation/jdf.webinar.1.pdf

The half-power beam width (HPBW) or full width to half-maximum (FWHM), as seen in figure 16, defines the resolving power, so the capability of an antenna to spatially resolve a source. In an interferometer, this quantity is given by:

$$\theta_{FWHM} = \frac{\lambda}{b_{max}} \tag{29}$$

where λ is the wavelength of the observation, which, for radio observation, stands in the range of the sub-mm/mm, and b_{max} is the maximum distance between the two antennas. Compared to a singular antenna, the resolution power is given by $\theta = \frac{\lambda}{D}$, where D is the diameter of the single dish. Due to engineeristic problems, such as gravitational sagging or telescope deformations caused by differential solar heating throughout the whole dish of the antenna, the maximum diameter reachable is around $D \simeq 500m$, so the angular resolution of a singular antenna that operates in the radio frequencies stands around $\theta \simeq 2''$ (Condon et al. 2016). Instead, interferometers can achieve incredible resolving power: since the baselines of modern radio interferometers can reach distances up to several kilometers, the resolution obtained by this technique can be around milliarcseconds. It is also crucial to consider the beam width between first nulls (BWFN), also called primary beam, that represents the Field Of View (FOV) i.e. the portion of the sky observable by an antenna. The FOV is given by:

$$\theta_{BWFN} = \frac{\lambda}{D} \tag{30}$$

so it only depends on the diameter of the singular antenna, even for interferometers. There is an important difference between the two: in a single antenna configuration,

the size of the FOV is the same as the resolving power itself, so it can't provide enough resolution elements to make sufficient imaging. On the other hand, the FOV in an interferometer is several times the size of the beam, so it allows imaging. Additionally, while the collecting area of a single dish of diameter D is $\pi \cdot D^2/4$, an interferometer has N times this value, where N is the number of antennas in the array.

These concepts can be easily implemented in a multi-element interferometer with N antennas, that produce $N(N-1)/2$ unique baselines, where each interferometer pair presents a different sinusoidal response to the source. Though, interferometric observations suffer from the short spacing problem. The maximum recoverable scale is defined as:

$$\theta_{MRS} \propto \frac{\lambda}{b_{min}} \tag{31}$$

where b_{min} is the minimum baseline of the array. Since in an interferometer the shortest baseline achievable can't be less than two times the diameter of the antennas, otherwise they would overlap, it is then impossible to recover information from very large angular scale. This issue can be solved by providing a single dish antenna of diameter D bigger than the shorter baseline achievable by the array: an example is the Atacama Compact Array (ACA), discussed later (C. et al. 2022).

If the source is extended, to be properly treated with interferometric observation, it has to be composed by the sum of independent point sources. The correlator response expresses only the cosine component of the signal, the even part of the brightness distribution. Since every function can be thought as a sum of even and odd parts, the brightness distribution can be obtained by considering a cosine and a sine correlator, where the latter follows a $\pi/2$ phase delay. The combination of cosine and sine correlators is called a complex correlator, since it is possible to express trigonometrical functions as complex exponentials. The response to an extended source with a certain brightness distribution from an interferometer with a complex correlator is then called a complex visibility, expressed as:

$$V(u,v) = \int\int I(x,y) \exp^{-2\pi i(ux+vy)} \, dxdy \tag{32}$$

which, thanks to the van Cittert-Zernike theorem, measures the 2-D Fourier transform (FT) of the source brightness distribution.

To express the correlator response of an interferometer, a special cartesian coordinate system is used, called uv plane, which represents the spatial distribution of the baselines, in units of λ. A single baseline would then sample a single scale of the sky brightness distribution, measuring two points in the uv plane. Since visibilities represent a function with Hermitian symmetry, a single sampling will always return a point with coordinate (u,v) and its complex conjugate (-u, -v). A more complete sampling of the uv plane is then necessary to obtain the true sky brightness distribution. This can be achieved in different ways: first, with a greater number of antennas, the number of projected baselines increases as well, which then will return more visibilities and consequently an improved sampling of the uv plane. Secondly, it is possible to use the Earth's rotation aperture synthesis. Since the points in the

uv plane are just the projected baseline seen by the source, earth's rotation changes the positions of the baselines in the uv plane, increasing the sampling. For example, a 12 hour pointing of the source by a single baseline would trace a complete ellipse in the uv plane (Condon et al. 2016).

3.2 The Atacama Large Millimiter Array

The Atacama Large Millimeter/Submillimeter Array (ALMA) is an aperture synthesis telescope, located on the Chajantor plain of the Chilean Andes on an altitude of 5000m, made up of 66 antennas. These are divided into:

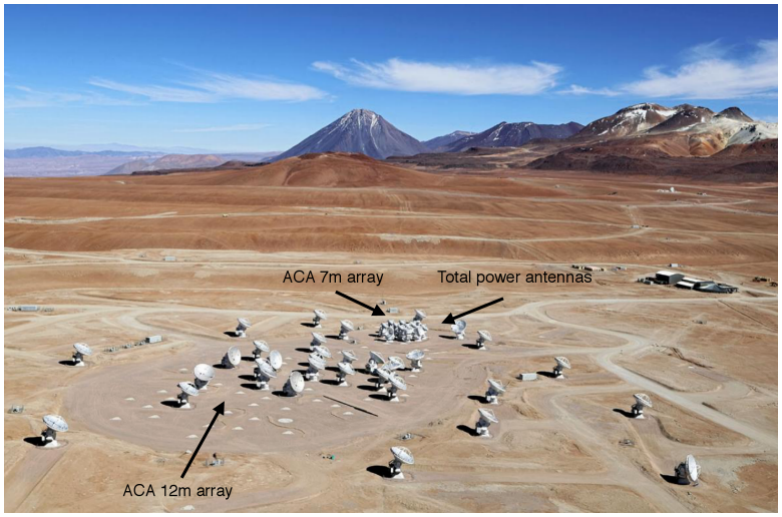

Figure 17: A picture of the Chajantor plain that shows the 12m and 7m ACA and the total power antennas. Credit - http://www.alma.inaf.it/images/Intro-ALMA-250219-jb.pdf

- the **12m array**; which is composed by fifty 12m dish receivers, capable of reaching baselines up to 16km.
- the **ACA**; composed of twelve 7m dish receivers, closely spaced one to each other, capable of creating baselines between 9m and 30m. This configuration is necessary to deal with the already mentioned short spacing problem that involves interferometric observations. The ACA have been then implemented to the ALMA facility to be more sensitive to emission on a larger angular scale.
- the **Total Power array (TP array)**; made of four 12m antennas, to perform single dish observations to cover even wider angular scale, providing baselines between 0m and 12m.

ALMA observations largely cover the sub-mm/mm emission band, measuring frequencies between 84 GHz and 950 GHz (2.6mm and 0.4mm). Then it will be fully operative, ALMA will be able to cover even lower emission, up to $35GHz$ ($6mm$).

Band	**Wavelength** $[mm]$	**Frequency** $[GHz]$	**First light**
1	8.57-6.00	35-50	Not yet implemented
2	4.48-3.33	67-90	Not yet implemented
3	3.57-2.59	84-116	2009
4	2.40-1.84	125-163	2013
5	1.84-1.42	163-211	2016
6	1.42-1.09	211-275	2009
7	1.09-0.80	275-373	2009
8	0.78-0.60	385-500	2013
9	0.50-0.42	602-720	2011
10	0.38-0.32	787-950	2012

Table 1: Table of the ten ALMA receivers with their observations wavelength/frequency band and in which year they became operative. In orange is underlined receiver 1, which is still in production, while in yellow is underlined the receiver 2, currently in development.

In table ?? we show the different receivers of ALMA and at which frequencies they operate.

Although the whole ALMA observation band is uneffected by the ionosphere, absorption and signal delays effect occur due to the presence of the troposphere. Since these effects are altitude and weather-dependent, the ALMA observatory was built on this peculiar site due to the considerably dry weather, clear sky conditions and high altitude. Even with these amazing requirements, the trophospheric absorption still effects data: in figure 18 is shown how the percentage of the transmitted emission varies based to different frequencies.

It can be also noted that these transmission curves depends on the precipitable water vapour (PWV). The PWV is an index that accounts for how much water is present in a column of atmosphere between the source and the instrument. It is defined as the water depth contained in the column, as if all the water had precipitated as rain, thus its unit of measurement is length. As we show in figure 18, for high quantity of the PWV, the transmission probability decreases. In the best weather conditions, the PWV can reach 0.6mm, but typically it stands around 1mm, making it difficult to perform observations at high frequencies if not in optimal conditions. Moreover, variations in the PWV due to atmospheric turbulence cause phase fluctuations of the incoming signal, called phase noise, that can be expressed as:

$$\phi_e \simeq \frac{12.6\pi}{\lambda} \cdot PWV = \frac{12.6\pi\nu}{c} \cdot PWV \tag{33}$$

where ϕ_e represent the phase fluctuations, ν is the frequency of the observation and PWV is the value of the precipitable water vapour. Additionally, this effect is stronger for longer baseline since antennas can be placed at distances of several kilometers from one another to detect different atmospheric variations in the patch of sky interpose between the target and different antennas. This phase delay then

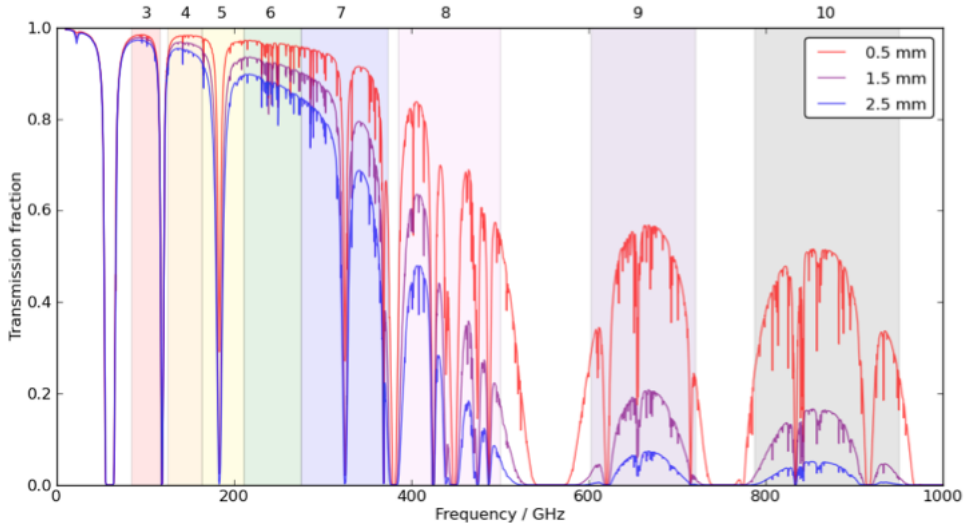

Figure 18: Atmospheric transmission fraction in respect to the frequency, in GHz. The different color bands show at which range of frequency the ALMA receivers operate. The color curves represent three different PWV densities during an year. (https://almaost.jb.man.ac.uk/help/)

creates decorrelation in the signal detected by the array, causing a lower integrated flux detection, up to 60% of the original brightness, due to visibility vectors partly cancelling out. To solve this issue, each 12m antenna contains a Water Vapor Radiometer (WVR), able to correct for these phase fluctuations. The WVR detect the PWV in the layers of atmosphere between the target and the antenna, measuring the 183 GHz water emission line of the atmosphere in four different wavelength intervals. Since each antenna is provided with its own WVR, this instrument constantly measures the PWV, in intervals of 1s each, due to very fast variation of the atmospheric turbulence. Other than the WVR, each antenna is provided of a cryostat, that can contain up to ten cartridges, each covering one frequency band, back-end electronics and an Amplitude Calibration Device (ACD). The latter is able to measure the system noise temperature T_{sys}, which is the output of the radio telescope, including the observed source, and the receiver temperature T_{rx} caused by the overheating of the receivers.

The data obtained by each observation are transformed into the ALMA Science Data Model (ASDM): this format is then converted into a measurement set (MS), which keep visibility data in a table system, to be utilized in the Common Astronomy Software Application (CASA) (McMullin et al. 2007), developed to perform calibration and imaging of interferometric data. The main table contains the radio data obtained in the observation in a column called *data*. When a calibration is applied to the *data* column, a *corrected* column is created to contain the calibrated data leaving the original data untouched. Furthermore, a *model* column can be required to store expectation values for the emission of calibration sources.

3.3 How to determine sizes

The first step to perform the data analysis was to download the data, directly from the webpage of the ALPINE collaboration. Two different types of data were obtained:

- **Measurement sets**; since these are interferometric data and, as previously explained, are organized in .ms file. These data were previously analysed by the ALPINE team, performed a 30s time averaging of visibilities. These interferometric data contained both the [CII] line and the dust continuum emission. Since in this thesis we are interested only on the dust continuum emission, it is necessary to remove the [CII] emission line. Moreover, the data release team noticed that some antennae were not perfectly calibrated so, to perform imaging or uv-fitting, is mandatory to flag these malfunctioning antennas beforehand. The list of the antennas to flag were obtained via private communication.

- **Raw cubes**; these are 3-dimensional images of the target, where two dimensions refer to the position of the source (RA and DEC) and the third is the frequency. These raw cubes are used to track emission in different position at different frequencies, in particular to identify the presence of line emission in the target: specifically, in the ALPINE survey, they have been used to track the [CII] $158\mu m$ emission line. In this thesis, we also target this emission line, however, we subtract it from the .ms file, to isolate the continuum emission.

All the data analysis has been executed with the Common Astronomy Software Application (CASA). Since CASA allows to run its tasks via Python (www.python.org) scripts, we implemented different scripts to use on each source, to accelerate the process of data analysis. In the following, we will describe in detail each step of the data analysis performed on one target of the survey, $Deimos - Cosmos - 873756$. The same procedure is applied to all the targets.

The data analysis started with the measurements set (ms) of the corrected data. The first task we use on the interferometric data is the CASA task $flagdata$, being able to remove the malfunctioning antennae previously identified. For $Deimos - Cosmos - 873756$ no antennas was flagged as problematic, thus the use of $flagdata$ was not necessary. Later, we implement an useful CASA task: *listobs*, which allows the user to obtain a summary of the measurement set content. In particular, we use this task to retrieve the position of each target in the sky, i.e. the RA and DEC coordinates. Subsequently, we analyze the raw data cube to point out at which frequencies is found the [CII] emission, as we show in figure 19.

After identifying the [CII] emission frequencies, with the use of *plotms*, a task for plotting and interacting with visibility data, we visualize the measurement set file, showing the amplitude of the visibilities at different frequencies. With this, we identify the emission of the [CII] line found in a certain spectral window of the data set, as we show in figure 20.

Now, with the use of the CASA task *split*, it is possible to create a new visibility subset from an existing visibility set, which, in this case, was used to create a new measurement set that do not contain the [CII] emission, therefore we remove the

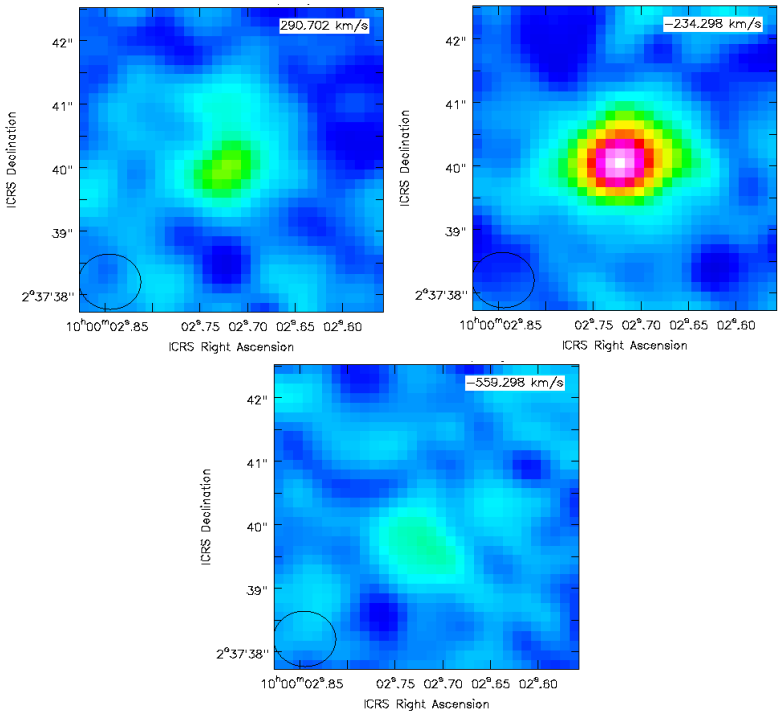

Figure 19: [CII] emission at different frequencies. The upper left panel shows the first detection of the [CII], at 342.22 GHz. The upper right panel shows the peak emission of the [CII] emission, which is found to be at 342.82 GHz. The centra panel shows the last detection of the 158 μm line, at 343.18 GHz

data obtained at a range of frequencies that include the emission peak line and its FWHM. Eventually, we obtain a new dataset, which solely contain the continuum emission. Therefore, we use this newly-created .ms file during the rest of the data analysis.

Now, using the CASA task *tclean*, we convert the visibilities contained in the new .ms file into an image, which shows the continuum emission. Therefore, in the following, we explain in detail the functioning of the *tclean* task.

The Fourier transform (FT) of the calibrated visibilities is able to produce a real image of the source. This is possible since the image is obtained by the convolution between the FT of the complex visibilities in the ideal case and the FT of the sampling function relative to the observation. To obtain an image that can be used for scientific purposes, it is required to perform the deconvolution of the anti-FT of the calibrated visibilities, called dirty image, with the anti-FT of the sampling function called dirty beam. So the *tclean* algorithm is able to obtain an image from the calibrated visibilities removing the secondary lobes introduced by the dirty beam, caused by the poor sampling of the visibilities in the *uv* plane, shown in figure 21, where, in the ideal case the *uv* plane would be completely covered by the observation.

The *tclean* removes the intensity peak from the dirty image, positioning the dirty beam above it and subtracting it: these clean visibilities are then added to a second map. This process continues until a threshold is reached (in rms, intensity or number of interactions). At the end of the cleaning process, two images are obtained: the

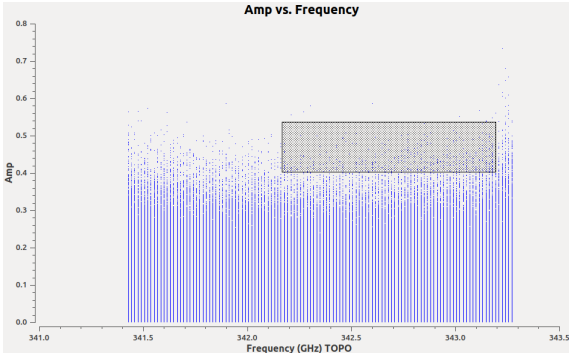

Figure 20: Plot of Amplitude vs Frequencies for the spectral window 0. The gridder region is a function of plotms, which is able to provide information on the selected points of the dataset.

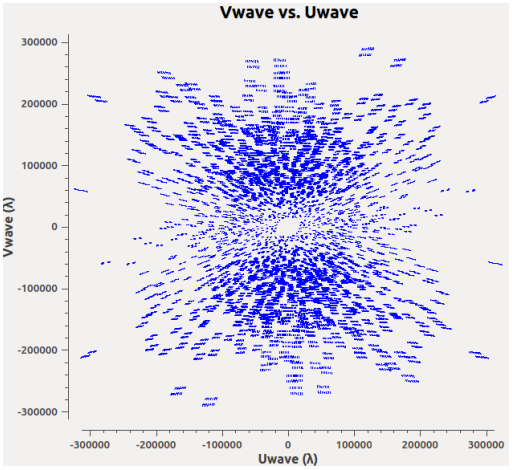

Figure 21: Coverage of the *uv* plane by the observation of $Deimos - Cosmos - 873756$.

residual image, containing all the data that have been excluded by the threshold established, and the model image with the cleaning. At the latter the process of *restore* is applied, where the clean beam, a Gaussian function that approximates the peak of the dirty beam, is convolved with each model component, which eventually will be added to the residual image.

To use the *tclean* task, it is necessary to define some parameters: the cell-size, which is the pixel size in the image, and the image size, which is the size of the image in pixels. The first one is given by the resolution element. Due to the Nyquist's sampling theorem, the pixel size is usually assumed 1/4 or 1/5 of the angular resolution, given by λ/B. This value can be obtained by considering the largest baseline of the observation in units of λ. For the considered target, this is equal to $B/\lambda = 366'500$. Considering its inverse, the value of the cell size, in arcsec, is then equal to:

$$\frac{\lambda}{B} \cdot \frac{206'265}{4} \simeq 0.14" \tag{34}$$

The image size (imsize) must be at least twice the primary beam size, defined

as the FOV, in order to avoid bright sources near the edge of the image that would cause aliasing. Given the values for λ ($8.6 \cdot 10^{-4}$m), and of the antenna diameter (12m), we obtain a FOV of $\simeq$ 15", which result in an image size of 30"x30" (216x216 in pixels).

Furthermore, it is necessary to keep in mind that the response of the antenna to the incoming signal is not uniform over the entire surface of the dish: this is called the primary beam effect. The signal that will reach the edges of the antenna will not be as intense as the one received at the center of it. Since for each antenna and observation, the primary beam model is known, it is possible to implement inside the *tclean* task the primary beam correction. However, this effect is better noticed for extended sources, with sizes around the value of the FOV, while the sizes of the targets in this thesis are comparable the angular resolution of the observation. Nevertheless, to perform imaging it is suggested to correct for this effect, as done in this work. Eventually, to create a continuum image, it is required to use the Multi-Frequency-Synthesis (MFS): this is a technique that allows different frequencies measurements to be combined during imaging, to create an image at a single frequency.

After implementing all the parameters explained above, we finally create the continuum image of the calibrated visibilities as shown in figure 22.

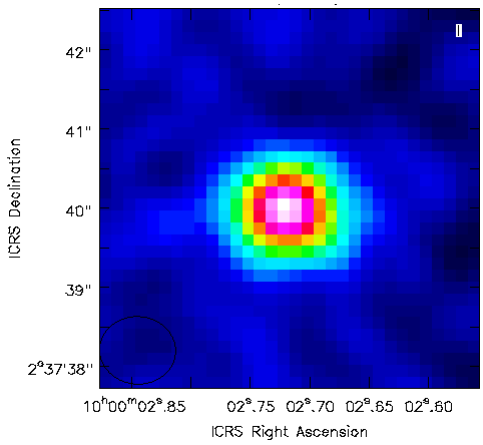

Figure 22: Continuum image of $Deimos - Cosmos - 873756$.

Now, to determine the size and the flux of the target, for first, we use the $imfit$ task. Its results will be the initial parameter of the task $uvmodelfit$, which will then return more accurate parameters. The CASA task $imfit$ fit an elliptical Gaussian component over a region of an image. The outcomes of this task are:

- Position in RA & DEC;
- Image component size, deconvolved from the beam;
- Integrated flux.

However, not all sources are resolved, so it will not always be possible to obtain a value of the image component size deconvolved from the beam: in this case, an upper limit of the size of the source will be given by the clean beam size.

To utilize the $imfit$ task, some parameters are required: the region of the image where the fit must be performed, the value of the rms, i.e. the root mean square of the measures, of the image and the range of pixels included in the fit.

First, a region must be taken around the source, located at the center of the image. The choice of the region is arbitrary, but it should be large enough to contain the source and, at the same time, it should avoid other non-target sources.

The rms is detected in the outer region of the image, resulting in a value of: $rms \simeq 4 \cdot 10^{-5} Jy/beam$. The $imfit$ task itself provide a default value of the rms, but computed inside the region used for the fit, hence, it does not represent a reliable value of the rms.

The pixels considered in the fitting procedure are the pixels with a significant peak flux (i.e. $F_{peak} > 3\sigma$), so, in this case: $3 \cdot \sigma = 1.2 \cdot 10^{-4} Jy/beam$.

Eventually, we use the $imfit$ task, also able to produce the images of the residual and model of the fit, to have some control over the success of the fit. In figure 23, the input image with the fitting region, the residual and the model of the fit are shown.

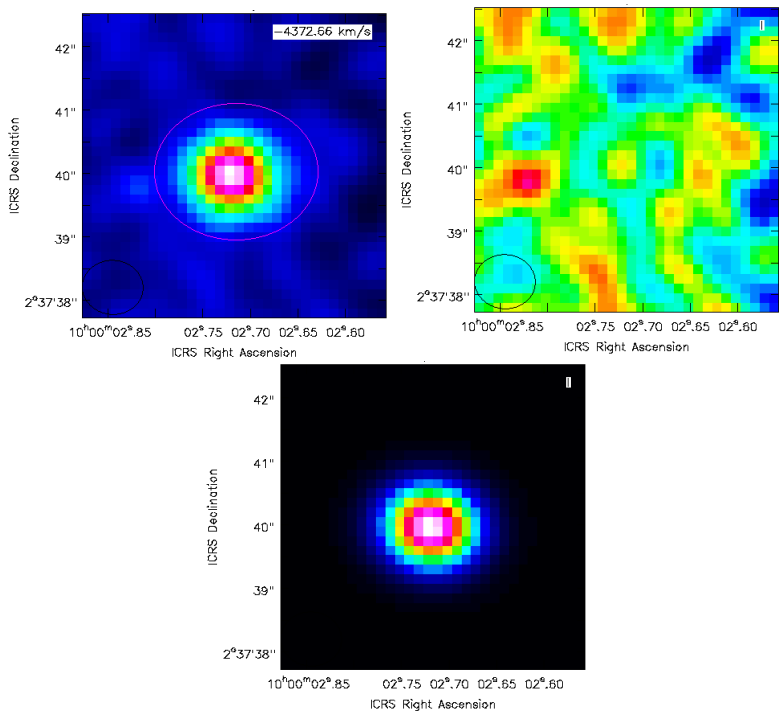

Figure 23: The top-left image shows the data image with, in pink, the fitting region required by the $imfit$ task. In the upper right and central panel, the residuals and the model of the fitting process are shown, respectively.

After obtaining these initial parameters, the task $uvmodelfit$ is used. Following the literature (see Fujimoto et al. (2020)), we apply this task only to sources with a total $S/N > 5$. This task does not produce an image-based fitting, instead, it makes a fit of a single component source model on the uv plane. Within this task, after imposing a Gaussian-type model, 6 initial parameters are requested:

- Integrated flux [Jy]

- $Xoff$ (offset east) [arcsec];
- $Yoff$ (offset north) [arcsec]
- Major axis of the FWHM a [arsec];
- Axis ratio q between minor axis b and major axis a of the FWHM [arcsec];
- Position angle [degree];

which can either vary in the fit or be kept fixed. In the first run of $uvmodelfit$, all the parameters are let free. While the $Xoff$ and the $Yoff$ need to be computed, the four remaining parameter are simply given by the result of $imfit$. The two offsets are calculated as the difference in the position of the source given by the observation, obtained by $listobs$, and the one given by $imfit$, in arcseconds units. Additionally, the number of iterations must be imposed, set at 5. The $uvmodelfit$ reports all the results in a component list. Now, as seen for the $imfit$ task, we produce the images of the residual and model of the $uvmodelfit$ task, as we show in Figure 24.

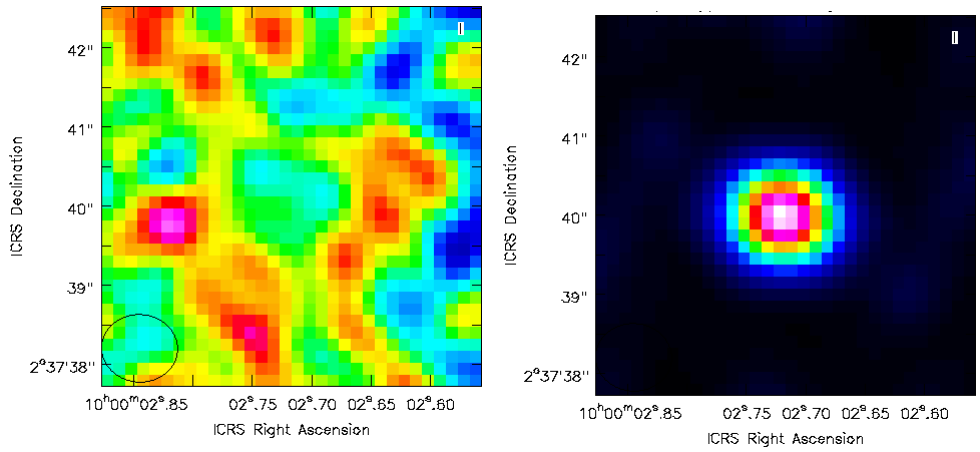

Figure 24: In the left and right image are shown, respectively, the residual and the model image of the fitting process with $uvmodelfit$.

If the outcome of the $uvmodelfit$ task is successful, it is then possible to perform another fitting process, fixing some parameters, such as $Xoff$, $Yoff$ and $flux$, to reduce the uncertainties on the source size parameters that are of interest for this work. Finally, the only step remaining is to convert the major axis and the minor axis of the FWHM into a size, defined as r_e, in kpc.

This is given by the following equation, in the case of a circular profile ($a = b = FWHM_{circ}$, where a and b are, generally, the deconvolved major and minor axis of the FWHM of the 2D-Gaussian respectively) (Voigt et al. 2010):

$$FWHM_{circ} = 2r_e \left(\frac{\ln 2}{k}\right)^n \tag{35}$$

where $k = 1.9992n - 0.3271$ and n is the Sérsic index. The latter is obtained by the Sérsic profile (Sérsic 1963):

$$I(r) = I_e \exp\left(-b_n \left[\left(\frac{r}{r_e}\right)^{\frac{1}{n}} - 1\right]\right) \tag{36}$$

where I_e is the intensity at the effective radius r_e, that encloses half of the total light from the model, and the constant b_n, which depends only on n. The Sérsic index thus defines the profile type, with $n = 0.5$ and 1 for Gaussian and exponential profiles respectively.

However, typically, fitting profiles are not circular but elliptical ($a > b$): in this case, we define the $FWHM_{circ}$ as the geometric mean of the major and minor axes:

$$FWHM_{circ} = \sqrt{a \cdot b} \tag{37}$$

Now, since in this work we solely performed fitting processes using Gaussian elliptical profiles, with the tasks $imfit$ and $uvmodelfit$ recalling equation 35 with $n = 0.5$, the effective radius is finally given by:

$$r_e = k \cdot \frac{FWHM_{circ}}{2} = k \cdot \frac{\sqrt{a \cdot b}}{2} \tag{38}$$

where k is the conversion factor from arcseconds to kpc, which depends on the cosmological parameters and the redshift of the target. In this work, we assume a ΛCDM cosmology with $\Omega_m = 0.3$, $\Omega_\lambda = 0.7$ and $H_0 = 70 s^{-1} Mpc^{-3} km$.

4 Sample

In this chapter we describe the sources used in the data analysis, selected from the ALMA Large Program to INvestigate [CII] at Early times (ALPINE) survey, which primary goal is to study the ISM properties and the SFRD at high redshifts, shortly after the epoch of re-ionization (figure 25).

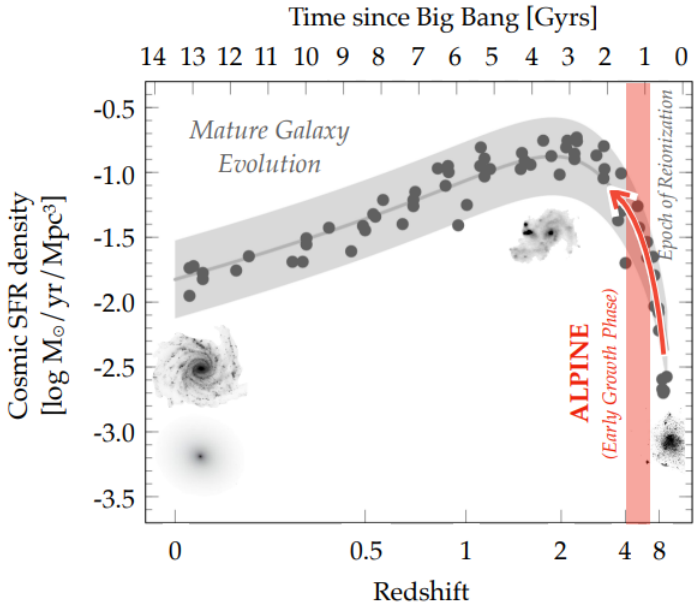

Figure 25: Cosmic SFRD as a function of redshift (and time since the Big Bang). The red bin shows the redshifts range ($4 < z < 6$) covered by the ALPINE survey, shortly after the epoch of re-ionization. The arrow in red indicates the growth of the total SFRD until its peak at $2 < z < 3$, to later decrease due to galaxy evolution processes (Andreas L. Faisst et al. 2022). Additionally, the images in grey show the evolution of galaxies' structure throughout cosmic time. This picture is taken from Andreas L. Faisst et al. 2022.

In the first paragraph, we summarizes the ALPINE survey, along with its main goals and most important results.
Secondly, we describe the selection criteria to determine the continuum catalog used in this work, out of the ALPINE sources.
Next, we present the results of the fitting processes and the diverse characterization of the continuum catalog.
Finally, we show the angular size, flux and luminosity measurement for each source of the continuum catalog.

4.1 Survey ALPINE

ALPINE (M. Béthermin et al. 2020, Le Fèvre et al. 2020, A. L. Faisst et al. 2020) is a survey, performed with the ALMA Telescope, focused on the detection of the emission line of the fine structure transition ($^2P_{3/2} \longrightarrow {}^2P_{1/2}$) of the single ionized carbon (C+ or [CII]) at 158 μm.

Due to its low ionization potential ($\simeq$ 11 eV), lower than the hydrogen's H (13.6 eV), the [CII] emission line is produced in different phases of the ISM (Lagache et al. 2018). Since the C+ is typically not affected by extinction, it represents the main coolant of photo-dissociation region (PDRs), cold neutral medium (CNM) and molecular clouds in high redshifted galaxies (Stacey et al. 2010). In addition, ALMA makes possible to simultaneously measure the nearby 160 µm continuum emission to track the dust emission.

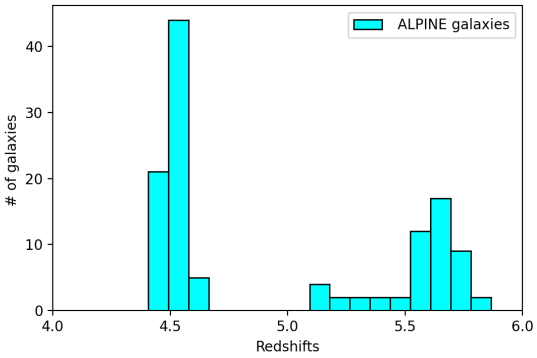

Figure 26: Histogram of the redshifts of the ALPINE targets. A redshift gap is noticeable between $z = 4.65$ and $z = 5.05$. In these redshift range, the [CII] 158 μm emission line is detected at frequencies between 313.6 GHz and 335.8 GHz, which correspond to a low transmission atmospheric window.

The ALPINE targets are selected from two cosmological fields: the Cosmic Evolution Survey (COSMOS) (RA=10:00:28.6, DEC=+02:12:21.0 (J2000)) (Scoville et al. 2007) and the Extended Chandra Deep Field South (E-CDFS) (RA=03:32:28.0, DEC=-27:48:30.0 (J2000)) (Giacconi et al. 2002).
All the ALPINE targets are UV-selected galaxies. Accurate redshifts of the targets come from two deep spectroscopic surveys: VUDS (Le Fèvre et al. 2015), using the VIMOS multi-object spectrograph mounted on the Very Large Telescope (VLT) on the southern emisphere, and DEIMOS (Hasinger et al. 2018), with the multi-object spectrograph located on the Keck Telescope, in the northern emisphere. In these two surveys, galaxies were firstly selected based on their photometric redshifts, derived in a variety of ways such as the detection of the $Ly\alpha$ emission line, lyman break color selection (LBGs) and UV absorption lines, to then confirmed as high redshift galaxies through UV spectroscopy (A. L. Faisst et al. 2020).
The spectroscopic redshifts of the ALPINE targets range between 4.4 and 5.9, but, to avoid atmospheric absorption features, the galaxies sample is split between redshifts of $4.40 < z < 4.65$ and $5.05 < z < 5.90$ (M. Béthermin et al. 2020), as in figure 26.

In figure 27 is represented the typical SED of a star-forming galaxies at z$\simeq$5 together with the data available from the ALPINE survey and the physical quantities that can be derived.
The various goals of the ALPINE survey can be summarized as (Le Fèvre et al. 2020, A. L. Faisst et al. 2020):

- **Detect the most dust obscured galaxies, thanks to the [CII] line emission and the dust continuum emission at 158 μm:**
  The dust, in fact, absorbs the optical/UV photons produced by the stars and re-irradiates the energy at longer wavelength. As a consequence, the dust emission can be used as a tracer of the SFR of a galaxy (see Kennicutt 1998);

- **Characterize the MS star forming galaxies at z$\simeq$5 and their merger**

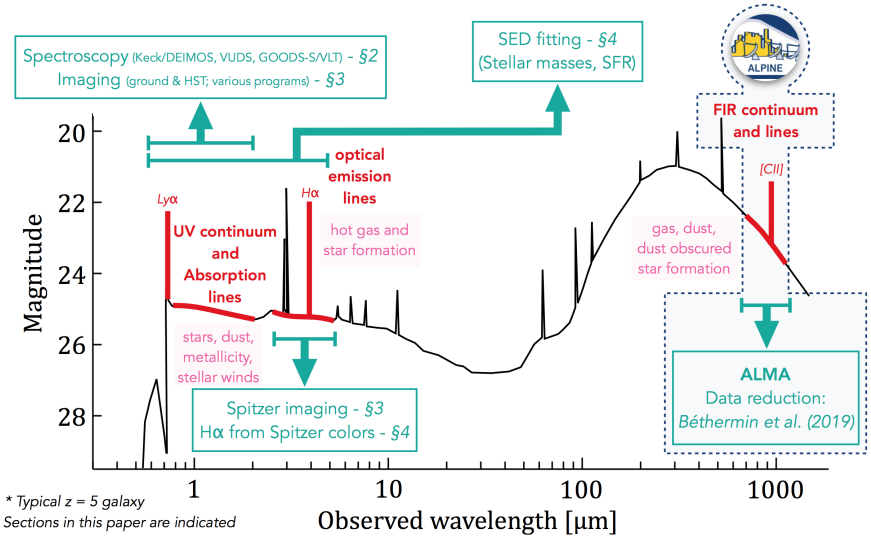

Figure 27: Multi-wavelength emission of a typical star forming galaxy at z≃5. In red we show the emission bands covered by different surveys. In the 1-10 μm range, the emission is observed by spectroscopy and imaging of the optical and UV band. These represent the UV-selected galaxies of the ALPINE survey, which completes the panchromatic study of high redshift galaxies through the detection of the [CII] line and its nearby continuum. The figure is taken from A. Faisst et al. 2020.

rates;

- **Study the total SFRD at this epoch**, which includes both the SFR derived from the UV continuum and the one in the far-IR from the dust emission;
- **Examine in detail the ISM properties**, through the luminosity relation L_{FIR}/L_{UV} and $[CII]/FIR$ diagnostic;

The observations were performed in the Band-7 of ALMA, since in the redshift range described above, the [CII] line emits in the 275-373 GHz frequency range. Observations started in May 2018 during Cycle 5 and they were completed in February 2019 in Cycle 6
Each target was observed for about 30 minutes and up to one hour of integration time, with the phase centers pointed to the UV rest-frame positions of the sources. Two spectral windows were used to detect the [CII] line and two more were added to account for the FIR continuum measurements. Detection was prioritised over spatial resolution: to maximise the integrated flux sensitivity, a compact array configuration was requested. Therefore, this resulted in a spatial resolution $0.7'' < \theta < 1''$, allowing to both avoid dilution of the flux density of the targets over several beams and achieve a relatively strong resolving power (M. Béthermin et al. 2020).

Eventually, 118 galaxies were observed, with 64% (75) of the targets detected in the [CII] range with an SNR>3.5 and 21% (23) in the continuum. In addition, 57 serendipitious non-target sources have been detected. The ALPINE collaboration found that the morphology of these galaxies in their study is quite varied: 40 % are mergers, 20% dispersion dominated, 13.3% rotating discs, 10.7% compact and the

remaining ones are too faint to be detected (Le Fèvre et al. 2020). This confirmed previous observations which showed that, at these high redshifts, galaxies show signs of merging but, at the same time, a significant number of galaxies have already settled onto a rotating disk (Young 2020).
Moreover, a large number of serendipitously HST-dark galaxies have been detected (Gruppioni et al. 2020, Le Fèvre et al. 2020), both in line and continuum, not found in previous optical surveys. This implies that the UV-selected sample does not include a significant number of obscured galaxies (Andreas L. Faisst et al. 2022). In Gruppioni et al. 2020, the SFRD from HST-dark galaxies found in ALPINE has been measured, finding that the obscured SFRD is $\simeq$ 17 % of the total SFRD at z>3.

This result is in agreement with findings from other selection techinque as in the radio band of HST-dark galaxies (see Talia et al. 2021, Enia et al. 2022). Additionally, from the dust continuum emission of the ALPINE galaxies, in Pozzi et al. 2021, the first estimate at high-z of the dust mass density (DMD) has been found.

4.2 Description of the continuum catalog analysed in the thesis

The sources used in this thesis are the continuum detected ALPINE targets (M. Béthermin et al. 2020).

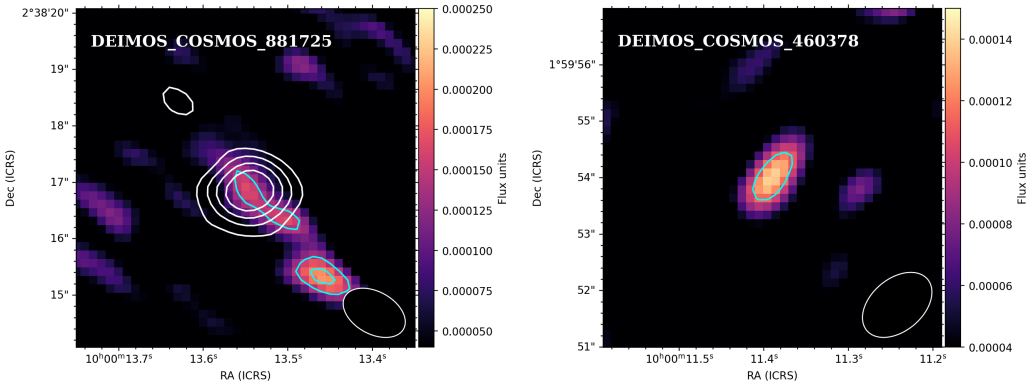

Figure 28: Continuum maps of two ALPINE targets. Cyan contours indicate the 3 and 4 σ levels. White contours on the left panel mark the [CII] line emission, obtained from the moment-0 maps, at 3, 5, 7, 9 σ. In the bottom right corner of both pictures we show the beam size of the observation. In the left image, $Deimos - Cosmos - 881725$ is shown, for which we did not determine its size due to its complex structure. In the right figure $Deimos - Cosmos - 460378$ is shown, a continuum target with no [CII] detection.

In M. Béthermin et al. 2020, the analysis of the ALPINE continuum detected sources is reported. To consider a source as a reliable continuum detection a certain SNR threshold must be established. This can be determined by introducing the concept of purity, or reliability of a source, as a function of the SNR. The purity of a source was computed as:

$$purity = \frac{N_{pos} - N_{neg}}{N_{pos}} \tag{39}$$

where N_{pos} and N_{neg} are the number of detections in the positive and negative maps, respectively. The purity was evaluated in a region of a 1″ radius. For the ALPINE targets, for a SNR of 3.5, a purity threshold of 95% was reached. Out of the 118 UV-selected ALPINE galaxies, 23 sources satisfied the cited criteria.
Moreover, 3 ALPINE targets are identified in the continuum range as multi-component objects (M. Béthermin et al. 2020). In this case, the methods explained in the previous chapter are not suitable to provide a size estimate. These 3 targets, i.e. $Deimos - Cosmos - 881725$, shown in figure 28, $Vuds - Cosmos - 5101209780$ and $Vuds - Efdcs - 530029038$ are excluded from this work [3].

Eventually, with the removal of these 3 problematic sources, the continuum catalog is made of 20 ALPINE targets. Out of these 20 galaxies, only 2 do not have a detection of the [CII] line emission, $Candels - Goodss - 19$ and $Deimos - Cosmos - 460378$, with the latter shown in figure 28. The remaining 18 sources, other than in the continuum, have all been detected by their [CII] emission, thus, to further characterize them, it is useful to consider their morpho-kinematic classification. Two different morpho-kinematic classifications have been produced. The first one is empirically visually-based on the 3D data-cubes, divided in the following classes (Le Fèvre et al. 2020):

- (1) Rotator (ROT);
- (2) Pair-Merger (MER);
- (3) Extended Dispersion dominated;
- (4) Compact Dispersion dominated;
- (5) Too weak to be classified.

The second morpho-kinematic classification is obtained using a tilted ring model fitting code (G. C. Jones et al. 2021). This classification is similar to the one defined above, but the (3) and (4) classes are combined into the dispersion dominated (DIS) category. Moreover, the class (5) is replaced by the uncertain (UNC) class. Finally, in table 2, we show the whole continuum catalog, containing all the sources of interest in this thesis.

[3] The remaining sources are shown in appendix A.1

Name	**Redshift** (1)	$M_\star$ $log_{10}(M/M_\odot)$(2)	$M_{mol,gas}$ $log_{10}(M/M_\odot)$(3)	**[CII]** (4)	**Morph. class.** (5)
CANDELS-GOODSS-19	4.500	9.8	–	–	–
CANDELS-GOODSS-32	4.411	9.7	–	2	ROT
DEIMOS-COSMOS-396844	4.524	9.9	10.52 ± 0.30	1	ROT
DEIMOS-COSMOS-417567	5.670	9.8	–	2	UNC
DEIMOS-COSMOS-422677	4.438	9.9	–	2	–
DEIMOS-COSMOS-460378	5.390	10.3	–	–	–
DEIMOS-COSMOS-488399	5.670	10.2	10.51 ± 0.30	3	–
DEIMOS-COSMOS-493583	4.513	9.6	–	2	–
DEIMOS-COSMOS-494057	5.545	10.2	10.38 ± 0.30	1	ROT
DEIMOS-COSMOS-539609	5.182	9.4	10.07 ± 0.31	1	–
DEIMOS-COSMOS-552206	5.502	10.6	–	2	ROT
DEIMOS-COSMOS-683613	5.542	10.2	10.34 ± 0.31	3	UNC
DEIMOS-COSMOS-818760	4.561	10.6	–	2	MER
DEIMOS-COSMOS-848185	5.293	10.4	10.72 ± 0.30	3	DIS
DEIMOS-COSMOS-873756	4.546	10.3	10.34 ± 0.31	2	DIS
vuds-cosmos-5100822662	4.5205	10.2	–	2	MER
vuds-cosmos-5100969402	4.579	10.0	10.16 ± 0.32	3	–
vuds-cosmos-5100994794	4.580	9.7	10.19 ± 0.31	3	UNC
vuds-cosmos-5101218326	4.574	11.0	10.74 ± 0.30	3	DIS
vuds-cosmos-5180966608	4.530	10.8	10.30 ± 0.30	2	UNC

Table 2: Target list of the ALPINE galaxies continuum detected, analysed in the present thesis (20 galaxies over the 23 continuum detected sources in ALPINE). (1) Spectroscopic redshifts derived from the [CII] emission line (Le Fèvre et al. 2020). (2) Stellar mass measurement obtained from A. L. Faisst et al. (2020). (3) Molecular mass measurement gathered from Dessauges-Zavadsky et al. (2020). (4) Visual-based morphological classification of the targets based on the [CII] emission (Le Fèvre et al. 2020). (5) Morphological classification of the targets in the [CII] emission using a tilted ring model fitting code (G. C. Jones et al. 2021).

4.3 Characterization of the continuum catalog

We now define 3 different targets' categories: merger, resolved and point-sources.

- **Merger**. In this category is included only one source, $Deimos - Cosmos - 818760$, shown in figure 29. This target is defined as a tri-component merger in the [CII] frequency range (see G. C. Jones et al. 2020) but is not flagged in the continuum range as a multi-component object, as others excluded from this thesis' analysis. To retrieve a size measurement for each one of the two main components of the merger, called E and C, we decided to use a two component Gaussian fit using the $imfit$ task. However, we find that the fit process is unreliable for the E component of the merger, thus, we will only consider the C component, including it in the resolved category for further analysis.

- **Resolved**. This bracket, including the C component of $Deimos - Cosmos - 818760$, contains 7 sources [4], all that have been resolved by the fitting tasks. These sources are all detected with $SNR > 5$, except for $Deimos - Cosmos - 552206$, which is detected at $SNR = 4.5$.

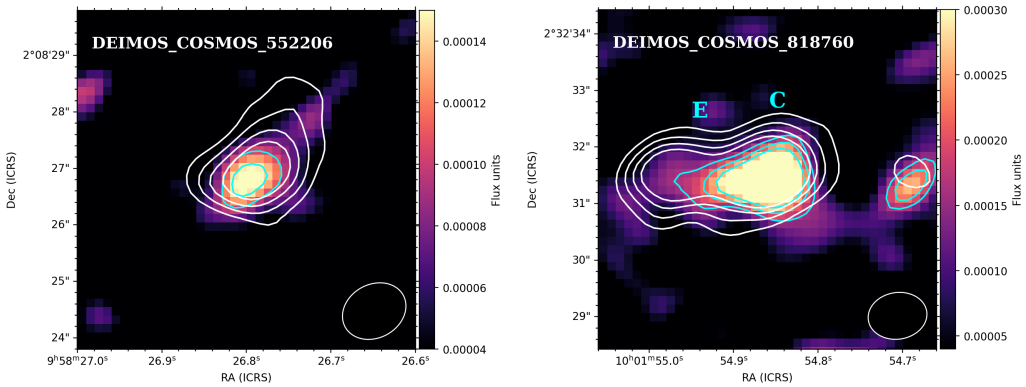

Figure 29: Continuum maps of two targets of the continuum catalog, in the same contour of image 28. In the left image is shown a resolved source, $Deimos - Cosmos - 552206$, detected with a $SNR \simeq 4.5$. In the right figure is pictured the merger target, $Deimos - Cosmos - 818760$, where are identified the two central components of this complex source, E and C.

- **Point-sources**. In this category are included all those targets for which the fitting processes could not produce a size measurement deconvolved from the beam. For targets with $3.5 < SNR < 5$, such as $Candels - Goodss - 32$, pictured in figure 30, the $imfit$ task itself define the target as a point source. For sources with $SNR > 5$, the $uvmodelfit$ task is able to estimate the the major axis a, but it provides an axes ratio q of value 1. This means that the source is partially resolved, along only one axis: in this case the source in consider a point source. $Candels - Goodss - 19$ is an example, shown in figure 30.

[4] These remaining sources are shown in appendix A.2

For both of these scenarios, we decided to set an upper limit on the angular sizes of these unresolved targets. This is given by the FWHM major and minor axes of the clean beam of each source. In this category are included 13 targets of the continuum catalog [5].

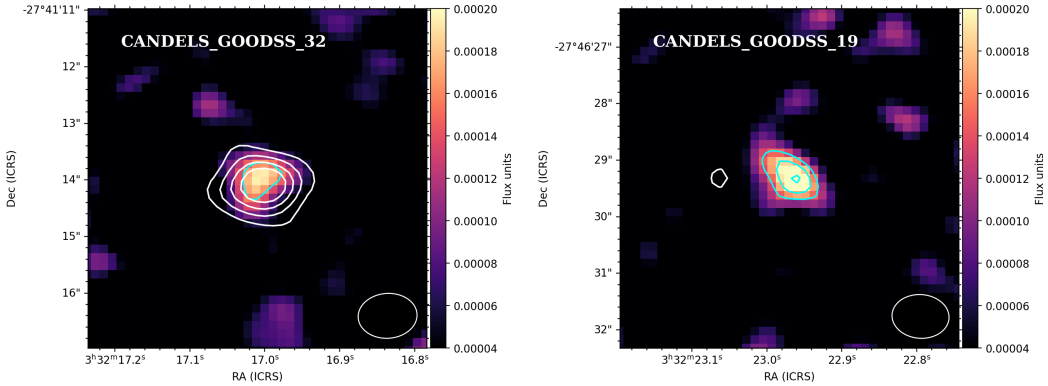

Figure 30: Continuum maps of two point sources of the continuum catalog, in the same contour of image 28. In the left image is shown $Candels - Goodss - 32$, detected with a $SNR \simeq 3.9$. In the right figure is pictured $Candels - Goodss - 19$, a continuum target with no [CII] detection, with a $SNR \simeq 5.4$.

4.4 Fitting result and its robustness

We have explained the criteria adopted for defining the continuum catalogue analysed in this thesis. To the 20 sources, we applied the procedure described in 3.3 in order to recover the continuum sizes. Table 3 show the fitting result of the sources, reporting the beam sizes, the sizes deconvolved with the beam and the integral continuum fluxes. In Figure 31, we show the plot of the angular sizes measurement (using equation 37) obtained computing the $imfit$ task results compared to the ones achieved with the $uvmodelfit$ task. As expected, the $imfit$ task produce a larger sizes estimate compared to $uvmodelfit$, thus confirming that $uvmodelfit$ provide more accurate results. In Figure 32 we compare the integrated fluxes of the sources in the continuum catalog found in literature (M. Béthermin et al. 2020) against the ones measured in this work. We find that, in general, the integrated fluxes measured in this work are comparable to the ones detected in literature, which confirms the reliability of our results.

[5] These remaining sources are shown in appendix A.3

Name	**Clean beam size**[*arcsec*]		**Size deconvolved with beam**[*arcsec*]		**Integrated Flux**
	Major Axis FWHM	Minor Axis FWHM	Major Axis FWHM	Minor Axis FWHM	[μJ]
CG-19	1.01	0.78	–	–	327 ± 40
CG-32	1.04	0.79	–	–	248 ± 41
DC-396844	1.28	0.77	0.64 ± 0.26	0.40 ± 0.29	374 ± 52
DC-417567	0.95	0.72	–	–	165 ± 20
DC-422677	0.98	0.80	–	–	245 ± 31
DC-460378	1.41	0.93	–	–	156 ± 30
DC-488399	1.22	0.99	–	–	207 ± 68
DC-493583	1.03	0.78	–	–	221 ± 78
DC-494057	1.01	0.86	–	–	181 ± 40
DC-539609	1.12	0.89	–	–	181 ± 24
DC-552206	1.17	0.95	0.99 ± 0.23	0.47 ± 0.27	241 ± 27
DC-683613	1.29	0.98	–	–	256 ± 76
DC-818760-C*	1.05	0.83	0.99 ± 0.25	0.66 ± 0.24	956 ± 102
DC-848185	0.92	0.85	1.19 ± 0.13	0.87 ± 0.17	503 ± 41
DC-873756	0.96	0.85	0.51 ± 0.04	0.44 ± 0.06	1271 ± 40
VC-5100822662	1.09	0.83	–	–	230 ± 51
VC-5100969402	0.98	0.81	–	–	238 ± 69
VC-5100994794	0.97	0.82	–	–	120 ± 24
VC-5101218326	1.20	0.83	1.09 ± 0.15	0.39 ± 0.19	487 ± 49
VC-5180966608	1.27	0.85	1.49 ± 0.17	0.34 ± 0.26	570 ± 57

Table 3: Table containing the results of the fitting processes. For the sources highlighted in bold, we report measurements using the *uvmodelfit* task. The targets in italics are sources with a $SNR > 5$ but reported as point sources by the *uvmodelfit* task, as described in text. * See text for detail.

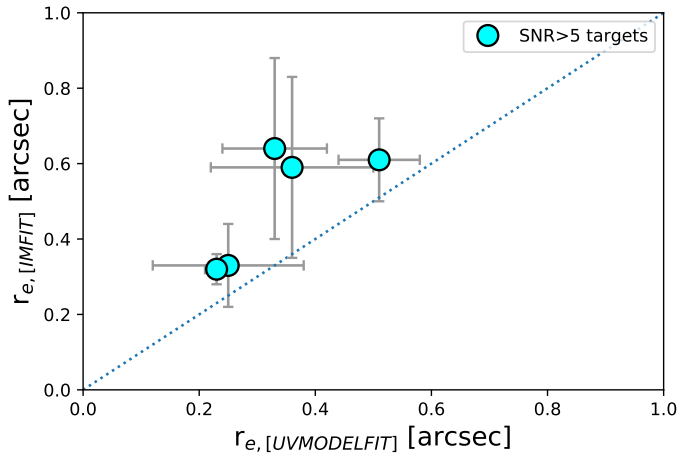

Figure 31: Plot of the $imfit$ task results compared to the $uvmodelfit$ task outputs for resolved sources with a $SNR > 5$. The dashed line represents the 1:1 line.

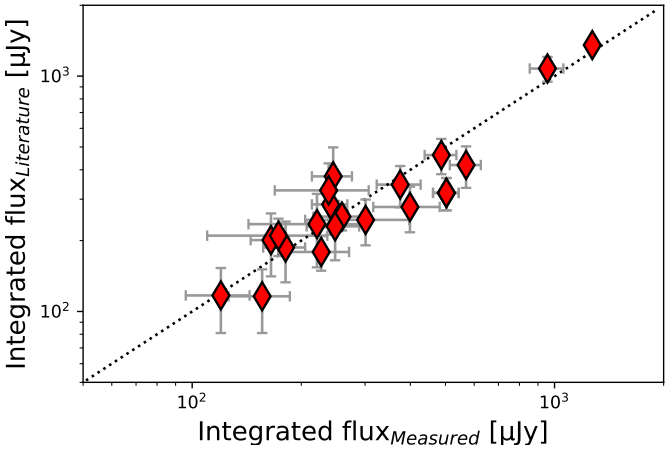

Figure 32: Plot of the integrated continuum fluxes measured in literature (M. Béthermin et al. 2020) against the integrated continuum fluxes obtained by the fitting tasks. The dashed line represents the 1:1 line.

5 Results & discussion

5.1 Dust sizes

In the current state of the art, two significant unresolved issues exist regarding the spatial extent of the dust continuum emission. Firstly, while several observational campaigns (Fujimoto et al. 2017, Calistro Rivera et al. 2018, Venemans et al. 2020) show that the dust emission, measured in the FIR rest-frame, is generally more compact than the emission associated with stars and gas, detected in the UV and [CII] respectively, simulation results (Cochrane et al. 2019) indicate that dust-based sizes are more extended than the stellar component.
Secondly, the evolution of galaxy size in the FIR rest-frame over the cosmic time and as a function of the stellar mass is still unconstrained. Some works support the idea of size decrease as a function of redshift (Gómez-Guijarro et al. 2022), whilst others find no significant evolution (Wang et al. 2022).
In this chapter, we compare our dust-based size measurements with detections in the [CII] and UV range for the same sources. In addition, we investigate whether or not an evolution of dust-based galaxy size exists as a function of cosmic time or as a function of stellar mass.

However, before presenting our results, two considerations must be made:

- **A consistent definition of galaxy size**
  To compare our results with findings from literature, we must define a consistent method to determine the size of a galaxy. Generally, size is intended as the effective radius r_e, which represents the radius containing half of the galaxy emission in a given band. Therefore, when we compare our results with other works, if an elliptical Gaussian profile has been used, we will compute the size measurement Using the procedure describe in section 3.3.

- **A difference in resolution may result in a different size**
  To resolve the structure of the dust emission (or of any compact component of a source), a certain resolving power is required, which, for interferometric observations, is related to the largest baseline used. ALMA can achieve a considerable resolving power ($\sim mas$), but high-resolution observations are less sensitive to extended, low surface brightness emission.
  While comparing observations performed at different resolutions, one must consider that since significant differences in size estimates may occur due to diverse scale sampling by different array configurations.
  In Figure 44, we test this effect by comparing [CII] size measurements at high resolution [$\sim$ 0.3"] (Venemans et al. 2020) with low resolution [$\sim$ 1"] (Decarli et al. 2018) of the same targets.
  In these two works, the authors performed an elliptical Gaussian fit with the $imfit$ CASA task, but the r_e definition differs one from the another: in Venemans et al. (2020), $r_e = \sqrt{a \cdot b}$, while in Decarli et al. (2018), $r_e = 0.5a$. As explained above, we recompute r_e as in equation 38 to coherently compare the results.
  We find that, in general, sizes measured from high-resolution observations are

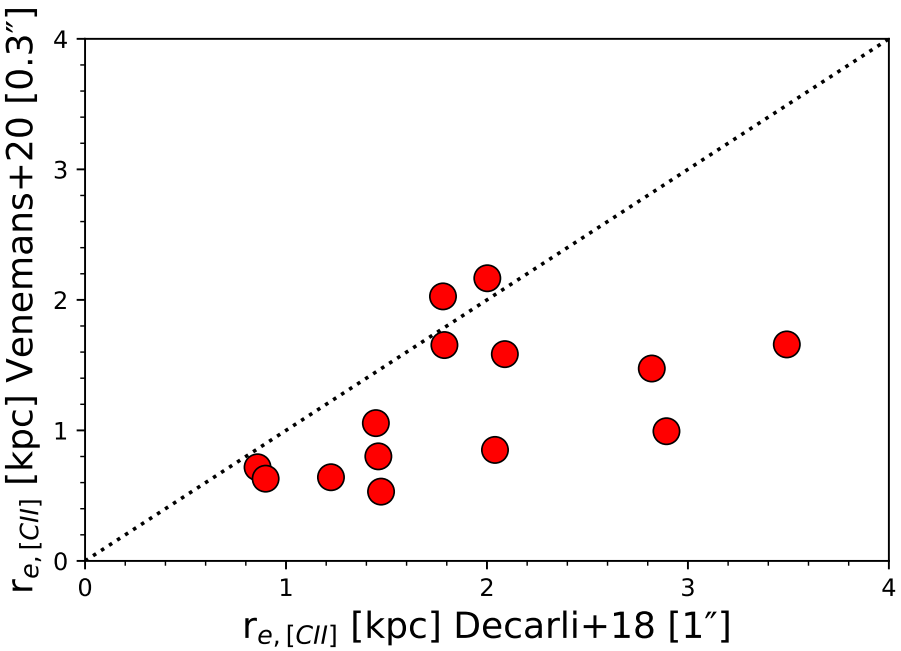

Figure 33: Comparison of [CII] effective radius measurements at high resolution (Venemans et al. 2020) and low resolution (Decarli et al. 2018) for the same quasars sources at redshift $z \gtrsim 6$. The dotted line represent the 1:1 line.

smaller than at lower resolution, by a median factor of $\sim 1.72 \pm 0.63$. From here on, to perform a more complete comparison, we will always provide the average beam size of every work presented.

5.1.1 Comparison between dust and [CII]-based sizes

In this section, we compare the FIR continuum sizes obtained in the present work, with the [CII] emission sizes obtained by Fujimoto et al. (2020) for the same ALPINE sources (diamonds in Figure 45). In Fujimoto et al. (2020), the effective radius for the [CII] emission ($r_{e,[CII]}$) are obtained using an exponential-disk profile, with Sérsic index of $n = 1$. Nevertheless, the authors find that the $r_{e,[CII]}$ values are consistent within $\sim 5\%$ with those obtained with a Sérsic index of 0.5, that is a Gaussian profile, as the one used in the present work.

Additionally, we remove from this comparison three out of six resolved sources and one out of ten unresolved source from the continuum catalog, since their $r_{e,[CII]}$ measurements are deemed as unreliable (see Fujimoto et al. 2020).
In Figure 45, we also include r_e results of [CII] and FIR, which traces gas and dust emission respectively, from other works (Izumi et al. 2018, Izumi et al. 2019, Venemans et al. 2020). In these papers, an elliptical Gaussian fit is performed to retrieve r_e, which we recalculate using the method described above.

From Figure 45, we obtain two main results:

- **The ALPINE sizes are the most extended ones**
  The ALPINE sources sizes, both in the [CII] and FIR emission, are the largest

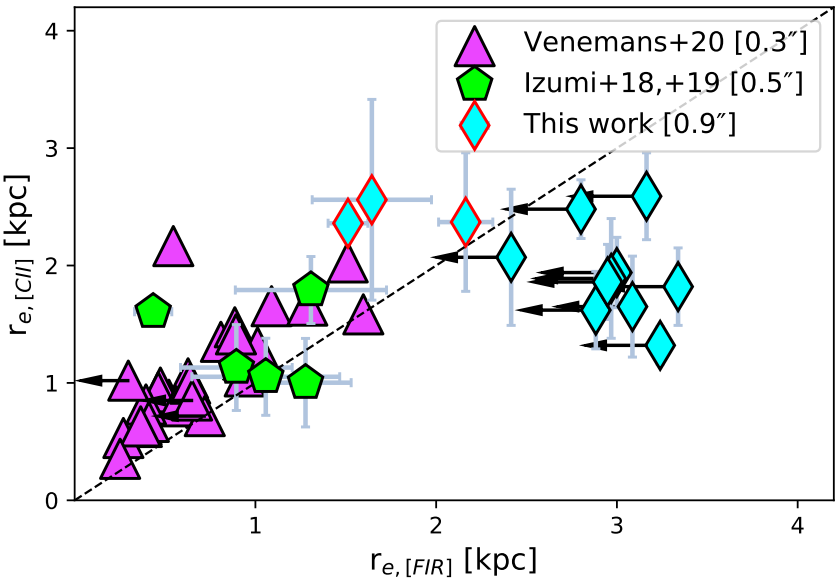

Figure 34: Comparison of the [CII] and FIR size measurements. We provide upper limits for unresolved sources: 3 from Venemans et al. (2020) and 9 from this work, both marked with arrows. The black dashed line represent the 1:1 line. In the legend, we provide the average beam size for each work. Resolved sources from this work are highlighted in thick red edges.

in the sample. While this result may be explained as due to different angular resolution, it can also be ascribed to intrinsic differences in the considered samples. Indeed, the works we considered include studies of very high redshifts ($z \geq 6$) quasars (QSOs), for which recent results suggest that they might be more compact than MS galaxies, such as in ALPINE (Li et al. 2021, Zhuang et al. 2022). Nevertheless, we decided to use these works as comparison since sizes from the [CII] and FIR emission were derived only for a few sources, in particular at such high redshifts.

- **The FIR emission is more compact than the [CII] emission**
  As confirmed by previous works, the dust size, traced by the FIR emission, is more compact than the gas size, traced by traced by the [CII] line, both in galaxies and quasars. For our resolved sources, we find that the $r_{e,CII}$ is larger than the $r_{e,FIR}$, where we estimate a size ratio of $\frac{r_{e,CII}}{r_{e,FIR}} \sim 1.40 \pm 0.29$, whereas in Gilli et al. (2022), where the authors compare the results of Venemans et al. (2020), Izumi et al. (2018) and Izumi et al. (2019), they find an average size ratio of ~ 1.5.
  The compactness of the dust continuum emission may depend on a gradient of the dust temperatures as a function of the radius (Calistro Rivera et al. 2018). Since the dust absorbed UV photons produced by stars and AGN, a stronger radiation field, as expected towards the centre of galaxies, may results in a decrease of the dust temperature towards large radii.

In Figure 47 we present the ratio between $r_{e,CII}$ and $r_{e,FIR}$ as a function of stellar mass. We do not find any positive nor negative trend in size ratio for increasing

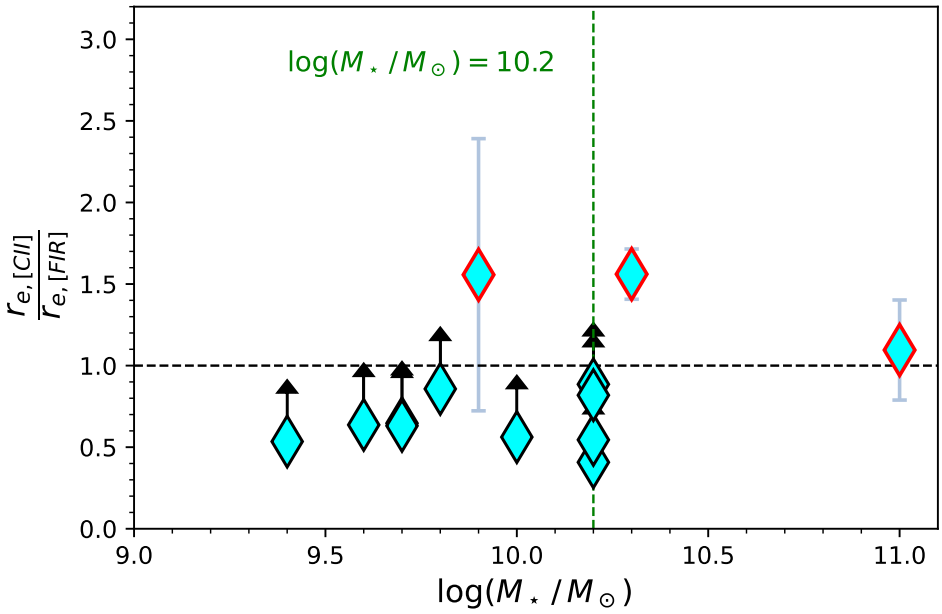

Figure 35: Ratio of $r_{e,CII}$ to $r_{e,FIR}$ as function of $M_\star$ for the ALPINE targets considered (12 sources). Upper limits for unresolved sources are marked with arrows, while resolved sources are highlighted in thick red edges.

stellar mass. Anyway, we can not draw any conclusions given the lack of sources at high stellar masses and the poor reliability of the size ratio at $\log\left(\frac{M_\star}{M_\odot}\right) < 10.2$ due to unresolved sources.

5.1.2 Stellar emission sizes as a function of FIR continuum radii

In Figure 36 we compare the $r_{e,FIR}$ obtained in this work with the effective radius measurements in the UV band from HST data, taken from Fujimoto et al. (2020). These last are obtained from the F160W and F814W filters of the Hubble Space Telescope, which, with these filter, can detect at very high redshifts ($4 < z < 6$) the stellar rest-frame UV emission. The $r_{e,F814W}$ and $r_{e,F160W}$ are derived as the $r_{e,CII}$ explained in section 5.1.1. In this analysis, we do not consider 55% of resolved and 35% of unresolved sources of this work since their $r_{e,[UV]}$ measurements are flagged as unreliable (see Fujimoto et al. 2020).
We find that dust-based size is generally more extended than the stellar emission, as opposed to findings of recent works (Fujimoto et al. 2017, Calistro Rivera et al. 2018, Nelson et al. 2019, Rujopakarn et al. 2019). We note that this result may be due to differences in PSFs between ALMA and HST, where the latter has much smaller value. Fujimoto et al. (2020) test this hypothesis, performing a Monte Carlo simulation for the rest-frame UV emission in the F814W map. They state that PSFs differences are not the cause of such compact stellar emission. Our result of a dust

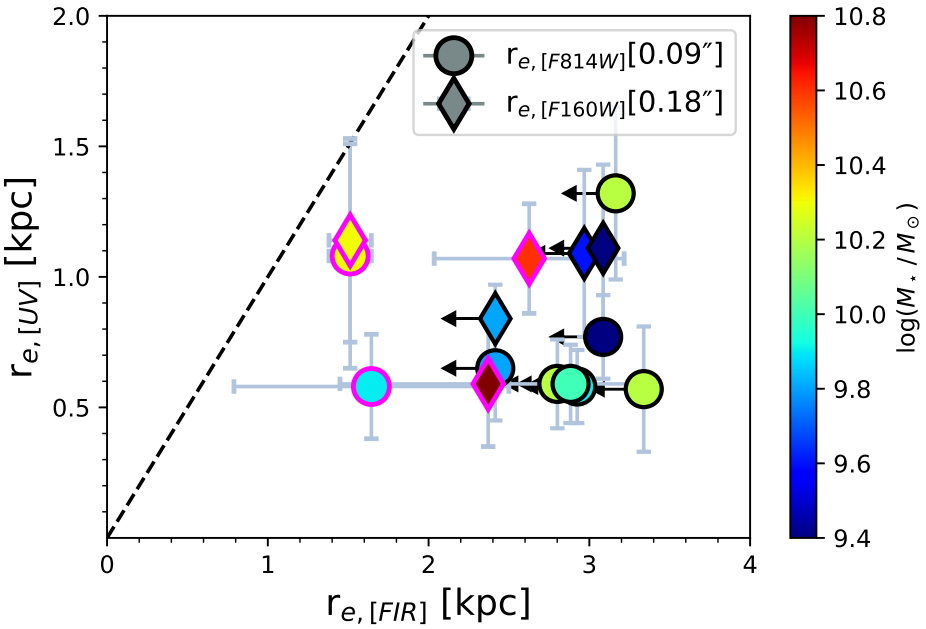

Figure 36: $r_{e,UV}$ as a function of $r_{e,FIR}$, in a $M_\star$ color scale (stellar mass estimates are obtained from A. L. Faisst et al. 2020). Upper limits for unresolved sources are marked with arrows, while resolved sources are highlighted with thick magenta edges. The black dashed line represent the 1:1 line and, in the legend, we report the average beam size for each observation.

size larger than the stellar one is in agreement with the results from simulations of star-forming galaxies in redshift range $1 < z < 5$ (Cochrane et al. 2019).
In Figure 37, we present the ratio between $r_{e,UV}$ and $r_{e,FIR}$ as a function of stellar mass. We find that, for the same sources, the $r_{e,F160W}/r_{e,FIR}$ are typically larger than $r_{e,F814W}/r_{e,FIR}$. This is discussed in Fujimoto et al. (2020), where Monte Carlo simulations confirm again that this result is not due to diverse PSFs but rather by dust absorption at different wavelengths, which affects the spatial morphology of the rest-frame UV emission.

Moreover, we compare our results with simulation of dust continuum size at different redshifts (Popping et al. 2022). The authors presents predictions for the spatial extent of the dust-continuum emission of MS galaxies, drawn from the TNG50 simulation, an high resolution variant of the IllustrinTNG simulation suite, at redshifts of $z = 1 - 5$. They couple the radiative transfer code $SKIRT$ (Camps et al. 2015) to the output of the TNG50 simulation to obtain dust sizes at the observed-frame of $850\mu m$ (Popping et al. 2022). We compare our findings with dust size measurements of Popping et al. (2022), but only for sources with stellar masses up to $\log\left(\frac{M_\star}{M_\odot}\right) = 10.1$, since their simulations do not extend over this value of stellar mass.
The authors compare the dust-continuum sizes with the stellar half-mass radius, where the latter appear to be more compact for increasing stellar mass, confirming

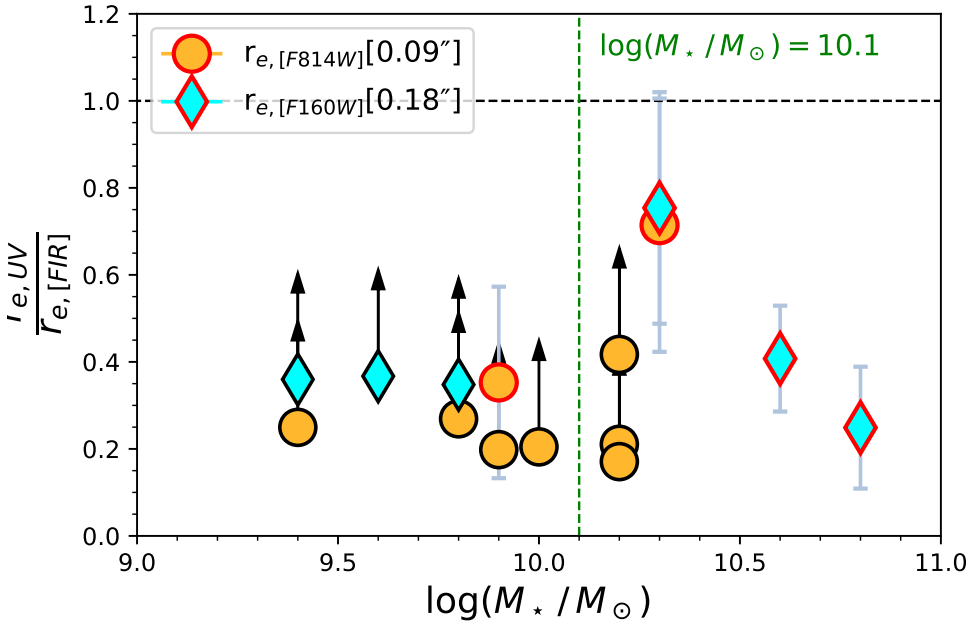

Figure 37: Ratio of $r_{e,UV}$ to $r_{e,FIR}$ as function of $M_\star$ for the ALPINE targets considered in the present analysis. Upper limits for unresolved sources are marked with arrows, while resolved sources are highlighted in thick red edges. In orange, we report the $r_{e,F814W}/r_{e,FIR}$, while in cyan, the $r_{e,F160W}/r_{e,FIR}$, with their respective average beam size.

our results. The same kind of agreement is not reached considering the 1.6 μm observed-frame emission stellar emission of the simulations: in his case, the 1.6 μm emission is more extended than the dust ones.

5.1.3 Dust-based size as a function of stellar mass

In this section we compare our relation between $r_{e,FIR}$ and the stellar masses, with other literature works:

- **Gómez-Guijarro et al. (2022)**:
  Here the authors propose a study of 88 galaxies at $1.5 < z < 4.5$ detected in the GOODS South field at $1.1mm$ at high and low resolution for a large range of stellar masses: $10 < \log\left(\frac{M_\star}{M_\odot}\right) < 11.4$. For 42 of these sources, divided in 26 at a low resolution in combination with high resolution data, referred as combined, (22 resolved and 4 unresolved) and 16 at low resolution (11 resolved and 5 unresolved), they report the $FWHM_{circ}$ obtained from fitting processes in the uv plane. To retrieve a comparable $r_{e,dust}$, we compute this $FWHM_{circ}$ in equation 38.

- **Wang et al. (2022)**;
  In this work, they investigate a large sample of normal star-forming galaxies at $0.4 < z < 3.6$ in the COSMOS field. The authors perform a stacking analysis

of their sources, dividing them in bins of redshift, SFR and stellar masses. Moreover, the authors obtain a $r_{e,dust}$ measurement for the stacked sources with an elliptical Gaussian profile, considering a conversion factor between r_e and $FWHM_{circ}$ of 0.41, comparable to the one used in our results;

- **Izumi et al. (2018), Izumi et al. (2019).**

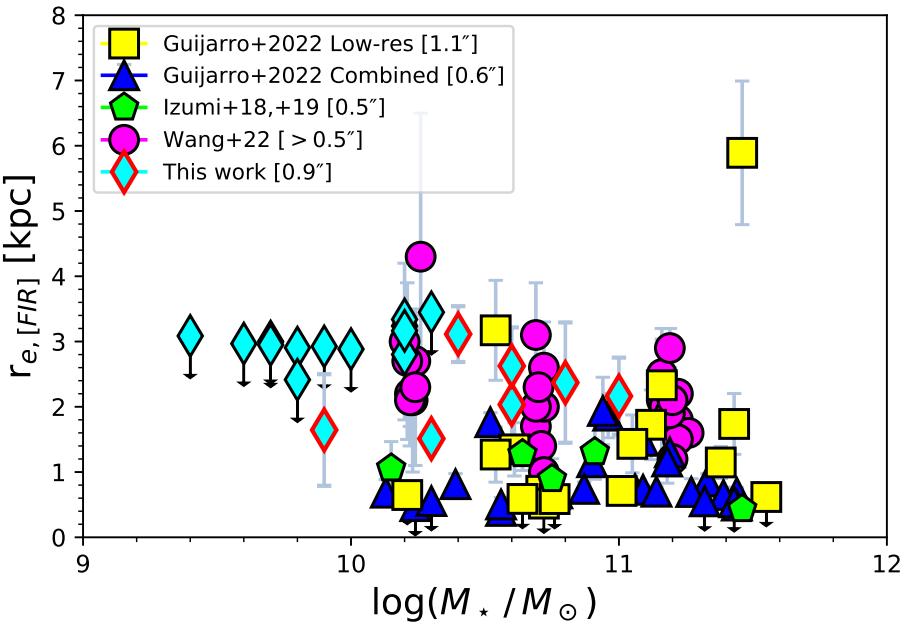

Figure 38: Plot of the $r_{e,FIR}$ measurements as a function of $M_\star$. Upper limits for unresolved sources are marked with arrows, while resolved sources from this work are highlighted in thick red edges. The different symbols refer to different samples as explained in the legend.

We find that $r_{e,FIR}$ of ALPINE galaxies, shown in Figure 38 as cyan diamonds, does not show any trend over stellar mass. Including also the other dataset, the effective radius smoothly decrease with increasing stellar mass. These results confirms simulation results from Popping et al. (2022).

To allow for a fairer comparison, we present $r_{e,FIR}$ over cosmic time, colour-coded with stellar mass, in Figure 39. Moreover, we compare these results with findings from Allen et al. (2017), a study of the 1.6 μm observed-frame emission for star-forming galaxies in a wide range of redshifts ($1< z <7$). The authors consider a mass-complete sample, focusing on galaxies with $\log\left(\frac{M_\star}{M_\odot}\right) > 10$: thus, care must be used when comparing Allen et al. (2017) results with objects that do not reach this stellar mass, in particular unresolved ALPINE galaxies.

From Figure 39 we conclude that the dust sizes do not evolve over redshift, as opposed to the UV spatial extent, which clearly shows evolution over cosmic time

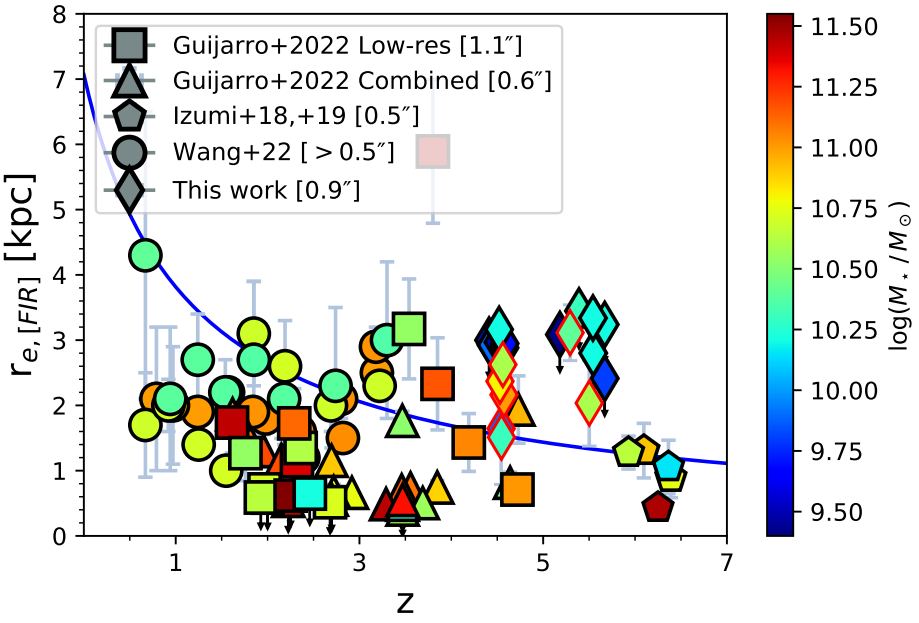

Figure 39: Comparison of $r_{e,FIR}$ measurements as a function of redshift, in a $M_\star$ color scale. Upper limits for unresolved sources are marked with arrows, while resolved sources from this work are highlighted in thick red edges. The blue curve represent the power-law relation between effective radius and redshift ($r_e = 7.07 \cdot (1+z)^{-0.89}$) obtained by Allen et al. (2017). The different symbols refer to different samples as explained in the legend.

(Allen et al. 2017). We confirm, as previously discussed, that $r_{e,FIR}$ for ALPINE galaxies are more extended than UV-based sizes.
We introduce the specific star formation rate ($sSFR = SFR/M_\star$) in Figure 40, which provides us with an insight on the the evolutionary stage of the individual objects. Considering the points from from Wang et al. (2022) and $r_{e,FIR}$ from this work, which are both sampling MS galaxies, we confirm, as expected, an increase of $sSFR$ for higher redshift (Feulner et al. 2005). For comparable values of $sSFR$, we do not find any significant evolution of $r_{e,FIR}$ over redshift. Additionally, for fixed redshift, we do not observe a significant increase in dust-based size for higher $sSFR$ or viceversa. To fully understand and explain these results, we must give some caveats:

- **Compared objects have different intrinsic characteristics**:
  Our results suffer from selection criteria towards brighter sources since ALPINE galaxies were selected to have an absolute UV magnitude of $M_{1500} = -20.2.$, which entails a $SFR > 10 M_\odot yr^{-1}$ (A. L. Faisst et al. 2020). Hence, when we compare characteristic of MS galaxies at different redshifts, we must keep in mind that the MS evolve in cosmic time, thus comparing parameters strictly related to the MS such as SFR or $M_\star$ may not yield reliable results.

- **Dust temperature greatly affects the shape of the dust emission**:

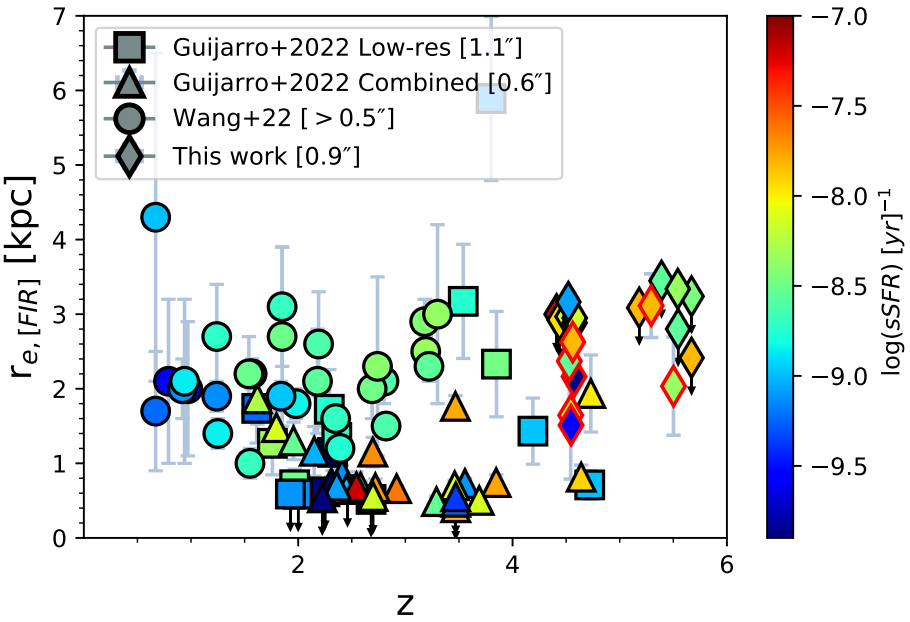

Figure 40: $r_{e,FIR}$ measurements as a function of redshift, in a $sSFR$ color scale. Upper limits for unresolved sources are marked with arrows, while resolved sources from this work are highlighted in thick red edges.

As we show in Figure 41a, emission in the FIR continuum is strongly related to dust temperature, where small variations of this parameter greatly affect the position of the peak of the SED. Moreover, recent literature find that dust temperature evolve over cosmic time: $T_d \propto (1+z)^{0.42}$ (Sommovigo et al. 2022). This means that the assumption of a single temperature, independent of redshift, should be regarded with caution.

- **Different works sample different rest-frames**:
  In order to compare our results with other works, it is crucial to understand at which rest-frame wavelengths the observations were carried on, which is related to redshift. As we show in Figure 41b, a galaxy SED strongly depends on redshift: hence, although the ALPINE survey, conducted in ALMA band 7, together with the A3Cosmos (Wang et al. 2022) and the GOODS-ALMA (Gómez-Guijarro et al. 2022) surveys, carried out in ALMA band 6-7 and band 6 respectively, observe a narrow range of frequencies ($211 - 373$ GHz), they all sample a different part of the rest-frame SED. While the ALPINE survey, at $4 < z < 6$ probes the peak of the dust emission at the 155 μm rest-frame, both the A3Cosmos and GOODS-ALMA surveys, detecting galaxies at lower redshifts, sample longer rest-frame wavelength, thus measuring the Rayleigh-Jeans regime of the grey body emission of the dust.

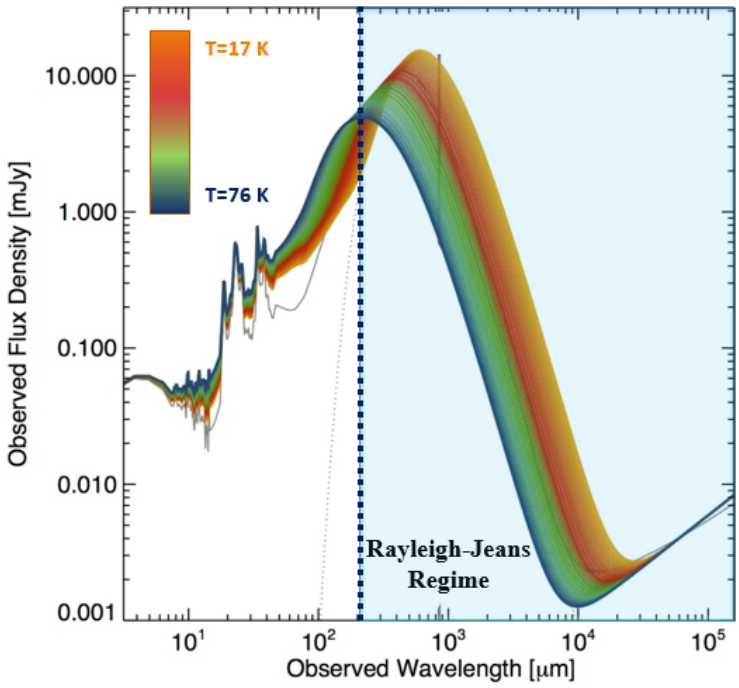

(a)

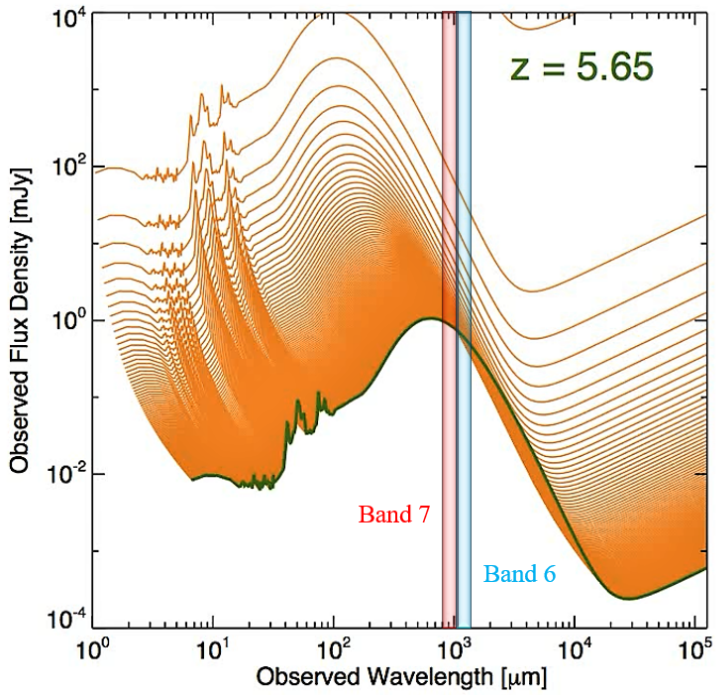

(b)

Figure 41: (a) Plot of a SED of a $z \sim 2$ dusty starburst that varies with dust temperature. The redshift and integrated $8 - 1000\mu m$ luminosity are fixed. The different curves are shown in a color scale, which are represented by a different temperature. The dotted blue line indicates the peak of dust emission for the highest dust temperature $T = 76K$ and the cyan shaded region indicates the Rayleigh-Jeans regime for the same curve. (b) Plot of a typical SED for a dusty starburst, where each curve express the SED at a different redshift. The green curve shows the SED at a redshift of $z = 5.65$, which represents the highest redshift for ALPINE galaxies in the continuum catalog. The red and blue shaded regions represents respectively the bands 7 and 6 of ALMA. (Credit: https://www.as.utexas.edu/~cmcasey/animated.html)

5.2 Minimum dust temperature and dust masses

Determining dust temperature, as we show in Figure 41a, is crucial to understand the physical state of the ISM at high-z. Moreover, dust temperature is fundamental to constrain dust mass, which can be used to determine the dust mass density (DMD) (Pozzi et al. 2021). In this section, we describe a method to determine the minimum dust temperature (see Gilli et al. 2022) for the continuum-detected ALPINE sources.

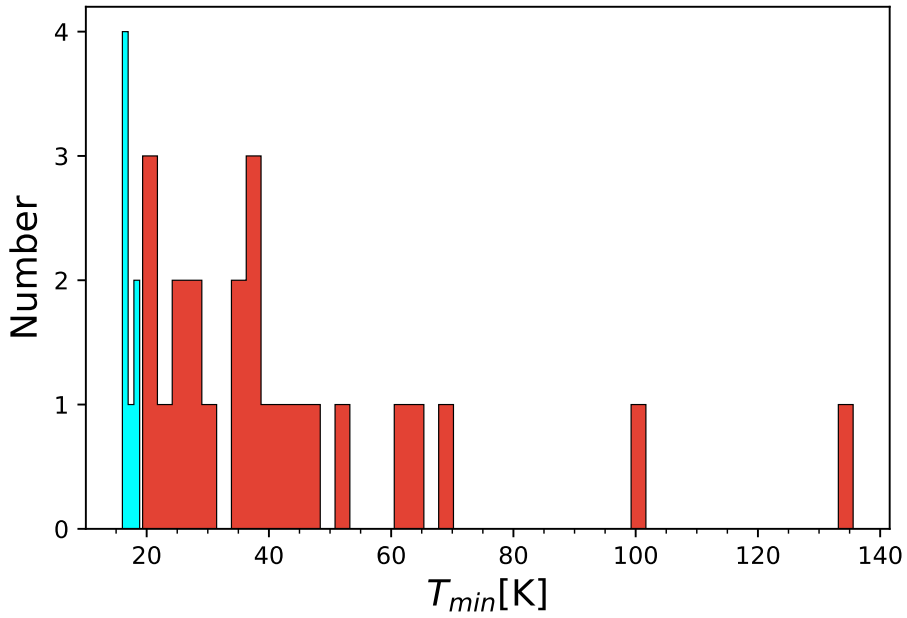

Figure 42: Histogram of dust minimum temperature. In red and cyan we show, respectively, minimum dust temperatures of high-z QSOs (Gilli et al. 2022) and MS galaxies (this work).

We consider for the dust emission, a general modified black body (MBB) at a single temperature (Gilli et al. 2022), as presented in 2.2.4. We can express the dust optical depth as function of its surface density $\Sigma_d = \frac{\tau_\nu}{\kappa_\nu}$, which again can be written as $\Sigma_d = \frac{M_d}{A}$, where M_d is the dust mass and $A = \pi r_e^2$ is the source physical area. Finally, we can express equation 21 in function of the dust mass:

$$M_d = -ln\left(1 - \frac{(1+z)^3 F_{\nu_{obs}}}{\Omega[B_\nu(T_d) - B_\nu(T_{CMB})]}\right)\frac{A}{\kappa_\nu} \tag{40}$$

Since the argument in the logarithm must be positive, rewriting the solid angle as $\Omega = \frac{A(1+z)^4}{D_L^2}$, where D_L is the luminosity distance, we obtain from equation 40:

$$B_\nu(T_d) > I_{\nu,min} = \frac{D_L^2 F_{\nu_{obs}}}{A(1+z)} + B_\nu(T_{CMB}) \tag{41}$$

from which we finally obtain an expression for the minimum dust temperature T_{min}, written as:

$$T_{min} = \frac{h\nu}{\kappa_B} \frac{1}{ln\left(1 + \frac{2h\nu^3}{c^2 I_{\nu,min}}\right)} \tag{42}$$

Using fluxes and sizes obtained from the fitting processes, we shall finally determine a minimum dust temperature for our sources. We can apply these equations only to the 7 resolved sources, since, opposed to unresolved sources, they provide a reliable size measurement. In Figure 42 we present our minimum dust temperature estimates, compared with results of high-z QSOs (Gilli et al. 2022)
We note that dust the temperatures obtained in this work are comparable with temperatures of the CMB at redshifts of the ALPINE survey ($T_{CMB} \sim 15 - 18K$). Our $T_{min,dust}$ are between $\sim 16 - 19K$ and are the lowest in the datasets of Figure 42. The temperature differences between our systems and the ones of Gilli et al. (2022) can be explained by considering that the dust temperatures obtained in this work are for normal, MS galaxies. Objects hosting an AGN, are expected to have a stronger radiation field.

Now, recalling equation 40, we can determine dust masses for the resolved sources of our continuum catalog. First, we assume a dust absorption coefficient $\kappa_\nu(\beta) = 0.77(\nu/352GHz)^\beta$ (Dunne et al. 2000), with the spectral index $\beta = 1.8$, which is the Galactic value from the Planck data (Planck Collaboration et al. 2011). Secondly, since we cannot use the minimum dust temperature found above, we must infer T_d assuming a SED of the dust emission at the redshifts of the ALPINE continuum catalog. M. Béthermin et al. (2020) derive a mean stacked SED of MS galaxies at similar redshifts of ALPINE, where they find a $T_d = 43 \pm 5K$ for sources in a redshift range of $z = 5 - 6$, which is the case for two out of the seven resolved sources of this work.

For targets with $z = 4 - 5$, the authors produce two different mean stacked SEDs, distinguishing them for different values of SFR. For $10 < SFR < 100 M_\odot/yr$, they find $T_d = 41 \pm 1K$, valid for three sources out of the seven resolved targets of this work, while the last two sources fall in the scenario of $SFR > 100 M_\odot/yr$, for which the authors find a dust temperature of $T_d = 47 \pm 2K$.
We present our results in Figure 43, comparing them with findings from Pozzi et al. (2021). We find that our findings differ from results of Pozzi et al. (2021), by a mean factor of 0.12 ± 0.06, which may be explained by the assumption of the dust temperature as explained below. The authors consider a MBB under the approximation of an optically thin regime ($\tau << 1$), using the following formula to retrieve dust masses:

$$M_{dust} = \frac{D_L^2 S_{\nu_{obs}}}{(1+z)\kappa_\nu B_\nu(T)} \tag{43}$$

We tested the possible factors responsible of the disagreement in the dust masses of the present work and those from Pozzi et al. (2021). On one hand, we find that a difference in dust size up to a factor of 5 would not change our dust masses. On the other hand, we find that the temperature is the driver of the different dust masses values. Indeed, while in Pozzi et al. (2021) the authors consider that the dust emission is ascribable to a cold dust component of $T_d = 25 - 35K$, similar to the one measured in the local universe, to compare their results with other works on

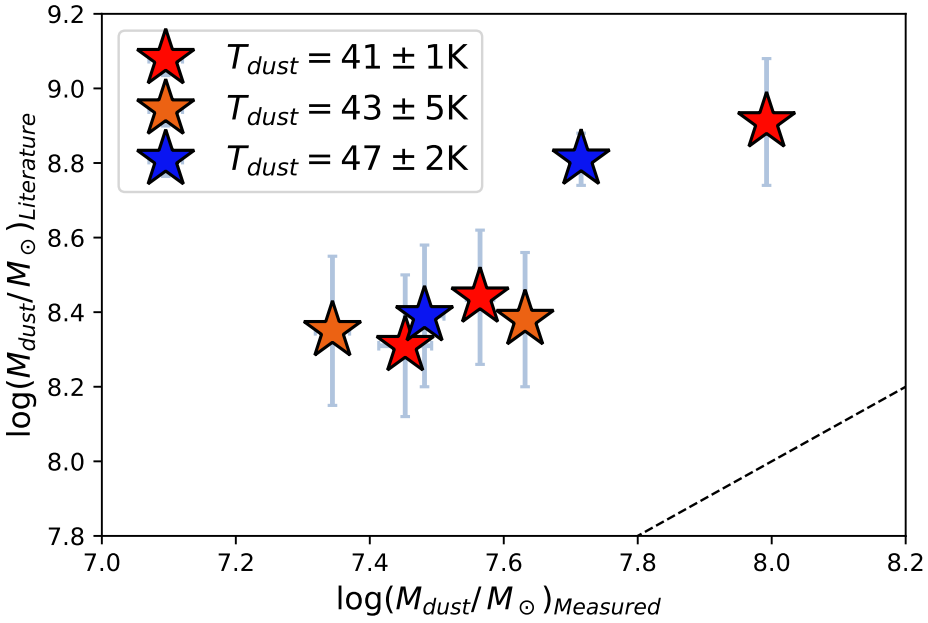

Figure 43: Comparison of dust mass obtained in this work with data from Pozzi et al. (2021). The black dashed line represent the 1:1 line. In the legend we show the different T_d used for each sources, as described in the text.

the DMD (Magnelli et al. 2020), in this work we consider warmer dust temperature. We confirm this by recomputing our dust masses, implementing the T_d used in Pozzi et al. (2021), for which we find a mean ratio of 0.76 ± 0.38. The dust masses presented in this work are estimated in the general case, with no hypothesis on the dust optical depth, while in Pozzi et al. (2021), the dust was assumed optically thin at $158\mu m$. The agreement between the two estimates when the same dust temperatures is assumed, confirm that the hypothesis related to the optical depth done in Pozzi et al. (2021) is correct.

6 Conclusions & future perspectives

The main goal of this thesis work was to define the spatial extent of the dust emission in high redshift galaxies and to estimate a lower limit on dust temperature, to constrain the dust masses. This enabled us to analyze galaxy size in an evolutionary context, to shed light on current uncertainties regarding the spatial extent of dust and stellar emission and to investigate the evolution of galaxy size as a function of cosmic time or stellar mass. In addition, we were able to determine minimum dust temperature at high-z ($z > 4$), which is currently poorly known, thus constraining the nature of the ISM at high redshift.

This was achieved by studying the 23 FIR-continuum detected main-sequence (MS) galaxies of the ALPINE survey, observed at high redshift ($4 < z < 6$). Starting from previously calibrated interferometric data, we performed imaging using the *tclean* CASA task. We later estimated dust size via a Gaussian fit in the image plane, using the $imfit$ CASA task, and for sources detected with a $SNR > 5$, we performed an additional Gaussian fit in the uv plane, using the $uvmodelfit$ CASA task. Out of the 23 FIR-continuum detected targets, only 20 have been taken into consideration in this work, since they have not been identified as mergers. Of these 20, 7 are spatially resolved.

We summarize the main results of this work as follows:

- By comparing the FIR continuum size with the [CII] emission size, obtained from Fujimoto et al. (2020), for the same ALPINE sources, we find that the latter is more extended than the continuum emission, on average by a factor of $\sim 1.40 \pm 0.29$. This result is confirmed by other studies (Gullberg et al. 2018, Fujimoto et al. 2019). The compactness of the dust emission may be related to a gradient of the dust temperature as a function of the radius (Calistro Rivera et al. 2018);

- We find that the FIR continuum sizes are generally more extended than the stellar spatial scale, obtained by Fujimoto et al. (2020), for the same ALPINE sources of this work. While this result is suggested by simulations (Cochrane et al. 2019), observations do not confirm these findings (Fujimoto et al. 2017, Rujopakarn et al. 2019);

- Comparing different galaxy populations at various redshifts (Izumi et al. 2018, Izumi et al. 2019, Gómez-Guijarro et al. 2022, Wang et al. 2022), we observe a decrease of the dust spatial extent as a function of stellar mass, confirmed by simulations (Popping et al. 2022). FIR continuum size does not show an evolution over redshift, as opposed to the stellar emission size (Allen et al. 2017).

- We estimate the minimum dust temperature for the resolved sources of this work, with values in the range of $T_{min,dust} \sim 16 - 19K$, barely above the CMB temperatures at these redshifts ($T_{CMB} \sim 15 - 18K$);

- We determine dust mass for the resolved sources of this work by assuming dust temperature in the range of $T_{dust} \sim 41 - 47K$, obtained from a stacked SED at

the redshift of ALPINE (M. Béthermin et al. 2020). In this scenario, we find the dust masses of the present thesis are almost a dex lower than the values reported in Pozzi et al. (2021) $\left\langle \frac{M_{dust,thiswork}}{M_{dust,Pozzi+21}} \right\rangle = 0.12 \pm 0.06$. This discrepancy is justified by the assumption for T_{dust}: assuming dust temperatures as in Pozzi et al. (2021) ($T_{dust} = 25 - 30K$), our results are comparable.

In the perspective of future observations, it may be relevant to extend the sample of MS galaxies at high redshifts ($z > 4$), since they have not been observed in statistically representative numbers (Le Fèvre et al. 2020). While ALPINE is one of the few surveys that achieved this, more than 50% of the continuum detected sources are unresolved: thus, follow-up observations of these sources at higher resolution would allow one to obtain a complete sample of resolved MS galaxies at $z > 4$.

As discussed before, dust temperatures at high-z are typically inferred by means of stacked spectra, obtained by the few photometric points available in observations. Therefore, in the near future, more photometric points need to be obtained, to derive more accurately the dust temperature.

Moreover, to obtain a more complete picture of galaxy evolution, by linking properties of local galaxy to the ones in the primordial universe, more extensive studies of MS galaxies at intermediate redshifts ($1 < z < 4$) should be performed.

Moreover, to make progress on the current issue regarding the spatial extent of dust and stellar emission, new high-resolution observations of galaxies will have to be performed with ALMA and the James Webb Space Telescope (JWST), respectively.

References

Allen, Rebecca J. et al. (Jan. 2017). "The Size Evolution of Star-forming Galaxies since z $\sim$ 7 Using ZFOURGE". In: 834.2, L11, p. L11. DOI: 10.3847/2041-8213/834/2/L11. arXiv: 1612.05262 [astro-ph.GA].

Álvarez-Márquez, J. et al. (Mar. 2016). "Dust properties of Lyman-break galaxies at z ~3". In: 587, A122, A122. DOI: 10.1051/0004-6361/201527190. arXiv: 1512.04120 [astro-ph.GA].

Asano, Ryosuke S. et al. (Mar. 2013). "Dust formation history of galaxies: A critical role of metallicity for the dust mass growth by accreting materials in the interstellar medium". In: *Earth, Planets and Space* 65.3, pp. 213–222. DOI: 10.5047/eps.2012.04.014. arXiv: 1206.0817 [astro-ph.GA].

Bell, Eric F. et al. (May 2005). "Toward an Understanding of the Rapid Decline of the Cosmic Star Formation Rate". In: 625.1, pp. 23–36. DOI: 10.1086/429552. arXiv: astro-ph/0502246 [astro-ph].

Béthermin, M. et al. (Nov. 2020). "The ALPINE-ALMA [CII] survey: Data processing, catalogs, and statistical source properties". In: 643, A2, A2. DOI: 10.1051/0004-6361/202037649. arXiv: 2002.00962 [astro-ph.GA].

Béthermin, Matthieu et al. (Jan. 2015). "Evolution of the dust emission of massive galaxies up to z = 4 and constraints on their dominant mode of star formation". In: 573, A113, A113. DOI: 10.1051/0004-6361/201425031. arXiv: 1409.5796 [astro-ph.GA].

Béthermin, Matthieu et al. (Nov. 2017). "The impact of clustering and angular resolution on far-infrared and millimeter continuum observations". In: 607, A89, A89. DOI: 10.1051/0004-6361/201730866. arXiv: 1703.08795 [astro-ph.GA].

Bouché, N. et al. (Aug. 2010). "The Impact of Cold Gas Accretion Above a Mass Floor on Galaxy Scaling Relations". In: 718.2, pp. 1001–1018. DOI: 10.1088/0004-637X/718/2/1001. arXiv: 0912.1858 [astro-ph.CO].

Bouwens, Rychard et al. (Oct. 2020). "The ALMA Spectroscopic Survey Large Program: The Infrared Excess of z = 1.5-10 UV-selected Galaxies and the Implied High-redshift Star Formation History". In: 902.2, 112, p. 112. DOI: 10.3847/1538-4357/abb830. arXiv: 2009.10727 [astro-ph.GA].

Burgarella, D. et al. (June 2013). "Herschel PEP/HerMES: the redshift evolution ($0 \leq z \leq 4$) of dust attenuation and of the total (UV+IR) star formation rate density". In: 554, A70, A70. DOI: 10.1051/0004-6361/201321651. arXiv: 1304.7000 [astro-ph.CO].

C., Cortes P. et al. (2022). *ALMA Technical Handbook,ALMA Doc. 9.3, ver. 1.0.* 2022, ALMA Technical Handbook, ALMA Doc. 9.3, ver. 1 ISBN 978-3-923524-66-2.

Calistro Rivera, Gabriela et al. (Aug. 2018). "Resolving the ISM at the Peak of Cosmic Star Formation with ALMA: The Distribution of CO and Dust Continuum in z $\sim$ 2.5 Submillimeter Galaxies". In: 863.1, 56, p. 56. DOI: 10.3847/1538-4357/aacffa. arXiv: 1804.06852 [astro-ph.GA].

Calura, F. et al. (Feb. 2017). "The dust-to-stellar mass ratio as a valuable tool to probe the evolution of local and distant star-forming galaxies". In: 465.1, pp. 54–67. DOI: 10.1093/mnras/stw2749. arXiv: 1610.08979 [astro-ph.GA].

Calura, Francesco et al. (Oct. 2003). "The Cosmic Evolution of the Galaxy Luminosity Density". In: 596.2, pp. 734–747. DOI: 10.1086/378195. arXiv: astro-ph/0307014 [astro-ph].

Camps, P. et al. (Mar. 2015). "SKIRT: An advanced dust radiative transfer code with a user-friendly architecture". In: *Astronomy and Computing* 9, pp. 20–33. DOI: 10.1016/j.ascom.2014.10.004. arXiv: 1410.1629 [astro-ph.IM].

Casasola, V. et al. (Sept. 2017). "Radial distribution of dust, stars, gas, and star-formation rate in DustPedia face-on galaxies". In: 605, A18, A18. DOI: 10.1051/0004-6361/201731020. arXiv: 1706.05351 [astro-ph.GA].

Chen, Chian-Chou et al. (Sept. 2017). "A Spatially Resolved Study of Cold Dust, Molecular Gas, H II Regions, and Stars in the z = 2.12 Submillimeter Galaxy ALESS67.1". In: 846.2, 108, p. 108. DOI: 10.3847/1538-4357/aa863a. arXiv: 1708.08937 [astro-ph.GA].

Cochrane, R. K. et al. (Sept. 2019). "Predictions for the spatial distribution of the dust continuum emission in $1 < z < 5$ star-forming galaxies". In: 488.2, pp. 1779–1789. DOI: 10.1093/mnras/stz1736. arXiv: 1905.13234 [astro-ph.GA].

Cochrane, R. K. et al. (May 2021). "Resolving a dusty, star-forming SHiZELS galaxy at z = 2.2 with HST, ALMA, and SINFONI on kiloparsec scales". In: 503.2, pp. 2622–2638. DOI: 10.1093/mnras/stab467. arXiv: 2102.07791 [astro-ph.GA].

Condon, James J. et al. (2016). "Essential Radio Astronomy". In.

Decarli, Roberto et al. (Feb. 2018). "An ALMA [C II] Survey of 27 Quasars at $z > 5.94$". In: 854.2, 97, p. 97. DOI: 10.3847/1538-4357/aaa5aa. arXiv: 1801.02641 [astro-ph.GA].

Demyk, K. (Jan. 2011). "Interstellar dust within the life cycle of the interstellar medium". In: *European Physical Journal Web of Conferences*. Vol. 18. European Physical Journal Web of Conferences, 03001, p. 03001. DOI: 10.1051/epjconf/20111803001.

Dessauges-Zavadsky, M. et al. (Nov. 2020). "The ALPINE-ALMA [C II] survey. Molecular gas budget in the early Universe as traced by [C II]". In: 643, A5, A5. DOI: 10.1051/0004-6361/202038231. arXiv: 2004.10771 [astro-ph.GA].

Draine, B. T. (Jan. 2003). "Interstellar Dust Grains". In: 41, pp. 241–289. DOI: 10.1146/annurev.astro.41.011802.094840. arXiv: astro-ph/0304489 [astro-ph].

Draine, B. T. et al. (Mar. 2007). "Infrared Emission from Interstellar Dust. IV. The Silicate-Graphite-PAH Model in the Post-Spitzer Era". In: 657.2, pp. 810–837. DOI: 10.1086/511055. arXiv: astro-ph/0608003 [astro-ph].

Draine, Bruce T. (2011). *Physics of the Interstellar and Intergalactic Medium*.

Dunne, Loretta et al. (June 2000). "The SCUBA Local Universe Galaxy Survey - I. First measurements of the submillimetre luminosity and dust mass functions". In: 315.1, pp. 115–139. DOI: 10.1046/j.1365-8711.2000.03386.x. arXiv: astro-ph/0002234 [astro-ph].

Enia, Andrea et al. (Mar. 2022). "A New Estimate of the Cosmic Star Formation Density from a Radio-selected Sample, and the Contribution of H-dark Galaxies at $z \geq 3$". In: 927.2, 204, p. 204. DOI: 10.3847/1538-4357/ac51ca. arXiv: 2202.00019 [astro-ph.CO].

Faisst, A. et al. (Jan. 2020). "Panchromatic study of the first galaxies with large ALMA programs". In: *Panchromatic Modelling with Next Generation Facilities*. Ed. by Médéric Boquien et al. Vol. 341, pp. 12–16. DOI: 10.1017/S1743921319001881. arXiv: 1901.01268 [astro-ph.GA].

Faisst, A. L. et al. (Apr. 2020). "The ALPINE-ALMA [C II] Survey: Multiwavelength Ancillary Data and Basic Physical Measurements". In: 247.2, 61, p. 61. DOI: 10.3847/1538-4365/ab7ccd. arXiv: 1912.01621 [astro-ph.GA].

Faisst, Andreas L. et al. (Nov. 2020). "ALMA characterizes the dust temperature of z $\sim$ 5.5 star-forming galaxies". In: 498.3, pp. 4192–4204. DOI: 10.1093/mnras/staa2545. arXiv: 2005.07716 [astro-ph.GA].

Faisst, Andreas L. et al. (June 2022). "ALPINE: A Large Survey to Understand Teenage Galaxies". In: *Universe* 8.6, p. 314. DOI: 10.3390/universe8060314. arXiv: 2206.03510 [astro-ph.GA].

Fakhouri, Onsi et al. (Aug. 2010). "The merger rates and mass assembly histories of dark matter haloes in the two Millennium simulations". In: 406.4, pp. 2267–2278. DOI: 10.1111/j.1365-2966.2010.16859.x. arXiv: 1001.2304 [astro-ph.CO].

Ferrara, A. et al. (Nov. 2016). "The problematic growth of dust in high-redshift galaxies". In: 463.1, pp. L112–L116. DOI: 10.1093/mnrasl/slw165. arXiv: 1606.07214 [astro-ph.GA].

Feulner, Georg et al. (Nov. 2005). "Specific Star Formation Rates to Redshift 5 from the FORS Deep Field and the GOODS-S Field". In: 633.1, pp. L9–L12. DOI: 10.1086/498109. arXiv: astro-ph/0509197 [astro-ph].

Fraternali, Filippo (Jan. 2017). "Gas Accretion via Condensation and Fountains". In: *Gas Accretion onto Galaxies*. Ed. by Andrew Fox et al. Vol. 430. Astrophysics and Space Science Library, p. 323. DOI: 10.1007/978-3-319-52512-9_14. arXiv: 1612.00477 [astro-ph.GA].

Fujimoto, Seiji et al. (Nov. 2017). "Demonstrating a New Census of Infrared Galaxies with ALMA (DANCING-ALMA). I. FIR Size and Luminosity Relation at z = 0-6 Revealed with 1034 ALMA Sources". In: 850.1, 83, p. 83. DOI: 10.3847/1538-4357/aa93e6. arXiv: 1703.02138 [astro-ph.GA].

Fujimoto, Seiji et al. (Dec. 2019). "First Identification of 10 kpc [C II] 158 μm Halos around Star-forming Galaxies at z = 5-7". In: 887.2, 107, p. 107. DOI: 10.3847/1538-4357/ab480f. arXiv: 1902.06760 [astro-ph.GA].

Fujimoto, Seiji et al. (Sept. 2020). "The ALPINE-ALMA [C II] Survey: Size of Individual Star-forming Galaxies at z = 4-6 and Their Extended Halo Structure". In: 900.1, 1, p. 1. DOI: 10.3847/1538-4357/ab94b3. arXiv: 2003.00013 [astro-ph.GA].

Giacconi, Riccardo et al. (Apr. 2002). "Chandra Deep Field South: The 1 Ms Catalog". In: 139.2, pp. 369–410. DOI: 10.1086/338927.

Gilli, R. et al. (Oct. 2022). "Supermassive black holes at high redshift are expected to be obscured by their massive host galaxies' interstellar medium". In: 666, A17, A17. DOI: 10.1051/0004-6361/202243708. arXiv: 2206.03508 [astro-ph.GA].

Gómez-Guijarro, C. et al. (Feb. 2022). "GOODS-ALMA 2.0: Source catalog, number counts, and prevailing compact sizes in 1.1 mm galaxies". In: 658, A43, A43. DOI: 10.1051/0004-6361/202141615. arXiv: 2106.13246 [astro-ph.GA].

Gruppioni, C. et al. (Nov. 2020). "The ALPINE-ALMA [CII] survey. The nature, luminosity function, and star formation history of dusty galaxies up to z 6". In: 643, A8, A8. DOI: 10.1051/0004-6361/202038487. arXiv: 2006.04974 [astro-ph.GA].

Gullberg, B. et al. (May 2018). "The Dust and [C II] Morphologies of Redshift ∼4.5 Sub-millimeter Galaxies at ∼200 pc Resolution: The Absence of Large Clumps in the Interstellar Medium at High-redshift". In: 859.1, 12, p. 12. DOI: 10.3847/1538-4357/aabe8c. arXiv: 1804.03663 [astro-ph.GA].

Güver, Tolga et al. (Dec. 2009). "The relation between optical extinction and hydrogen column density in the Galaxy". In: 400.4, pp. 2050–2053. DOI: 10.1111/j.1365-2966.2009.15598.x. arXiv: 0903.2057 [astro-ph.GA].

Hasinger, G. et al. (May 2018). "The DEIMOS 10K Spectroscopic Survey Catalog of the COSMOS Field". In: 858.2, 77, p. 77. DOI: 10.3847/1538-4357/aabacf. arXiv: 1803.09251 [astro-ph.GA].

Hodge, J. A. et al. (Dec. 2016). "Kiloparsec-scale Dust Disks in High-redshift Luminous Submillimeter Galaxies". In: 833.1, 103, p. 103. DOI: 10.3847/1538-4357/833/1/103. arXiv: 1609.09649 [astro-ph.GA].

Hodge, J. A. et al. (Dec. 2020). "High-redshift star formation in the Atacama large millimetre/submillimetre array era". In: *Royal Society Open Science* 7.12, 200556, p. 200556. DOI: 10.1098/rsos.200556. arXiv: 2004.00934 [astro-ph.GA].

Indebetouw, R. et al. (Feb. 2014). "Dust Production and Particle Acceleration in Supernova 1987A Revealed with ALMA". In: 782.1, L2, p. L2. DOI: 10.1088/2041-8205/782/1/L2. arXiv: 1312.4086 [astro-ph.SR].

Ivison, R. J. et al. (Nov. 2002). "Deep radio imaging of the SCUBA 8-mJy survey fields: submillimetre source identifications and redshift distribution". In: 337.1, pp. 1–25. DOI: 10.1046/j.1365-8711.2002.05900.x. arXiv: astro-ph/0206432 [astro-ph].

Izumi, Takuma et al. (June 2018). "Subaru High-z Exploration of Low-Luminosity Quasars (SHELLQs). III. Star formation properties of the host galaxies at z $\gtrsim$ 6 studied with ALMA". In: 70.3, 36, p. 36. DOI: 10.1093/pasj/psy026. arXiv: 1802.05742 [astro-ph.GA].

Izumi, Takuma et al. (Dec. 2019). "Subaru High-z Exploration of Low-Luminosity Quasars (SHELLQs). VIII. A less biased view of the early co-evolution of black holes and host galaxies". In: 71.6, 111, p. 111. DOI: 10.1093/pasj/psz096. arXiv: 1904.07345 [astro-ph.GA].

Jiménez-Andrade, E. F. et al. (May 2019). "Radio continuum size evolution of star-forming galaxies over 0.35 ¡ z ¡ 2.25". In: 625, A114, A114. DOI: 10.1051/0004-6361/201935178. arXiv: 1903.12217 [astro-ph.GA].

Jones, A. P. (May 2004). "Dust Destruction Processes". In: *Astrophysics of Dust*. Ed. by Adolf N. Witt et al. Vol. 309. Astronomical Society of the Pacific Conference Series, p. 347.

Jones, G. C. et al. (Jan. 2020). "The ALPINE-ALMA [C II] survey: a triple merger at z ∼ 4.56". In: 491.1, pp. L18–L23. DOI: 10.1093/mnrasl/slz154. arXiv: 1908.07777 [astro-ph.GA].

Jones, G. C. et al. (Nov. 2021). "The ALPINE-ALMA [C II] Survey: kinematic diversity and rotation in massive star-forming galaxies at z 4.4-5.9". In: 507.3, pp. 3540–3563. DOI: 10.1093/mnras/stab2226. arXiv: 2104.03099 [astro-ph.GA].

Kennicutt Robert C., Jr. (Jan. 1998). "Star Formation in Galaxies Along the Hubble Sequence". In: 36, pp. 189–232. DOI: 10.1146/annurev.astro.36.1.189. arXiv: astro-ph/9807187 [astro-ph].

Lagache, G. et al. (Jan. 2018). "The [CII] 158 μm line emission in high-redshift galaxies". In: 609, A130, A130. DOI: 10.1051/0004-6361/201732019. arXiv: 1711.00798 [astro-ph.GA].

Lang, Philipp et al. (July 2019). "Revealing the Stellar Mass and Dust Distributions of Submillimeter Galaxies at Redshift 2". In: 879.1, 54, p. 54. DOI: 10.3847/1538-4357/ab1f77. arXiv: 1905.06960 [astro-ph.GA].

Laporte, N. et al. (Mar. 2017). "Dust in the Reionization Era: ALMA Observations of a z = 8.38 Gravitationally Lensed Galaxy". In: 837.2, L21, p. L21. DOI: 10.3847/2041-8213/aa62aa. arXiv: 1703.02039 [astro-ph.GA].

Le Fèvre, O. et al. (Apr. 2015). "The VIMOS Ultra-Deep Survey: ~10 000 galaxies with spectroscopic redshifts to study galaxy assembly at early epochs 2 ¡ z 6". In: 576, A79, A79. DOI: 10.1051/0004-6361/201423829. arXiv: 1403.3938 [astro-ph.CO].

Le Fèvre, O. et al. (Nov. 2020). "The ALPINE-ALMA [CII] survey. Survey strategy, observations, and sample properties of 118 star-forming galaxies at 4 ¡ z ¡ 6". In: 643, A1, A1. DOI: 10.1051/0004-6361/201936965. arXiv: 1910.09517 [astro-ph.CO].

Leśniewska, Aleksandra et al. (Apr. 2019). "Dust production scenarios in galaxies at z ∼6-8.3". In: 624, L13, p. L13. DOI: 10.1051/0004-6361/201935149. arXiv: 1904.11185 [astro-ph.GA].

Li, Junyao et al. (Sept. 2021). "The Sizes of Quasar Host Galaxies in the Hyper Suprime-Cam Subaru Strategic Program". In: 918.1, 22, p. 22. DOI: 10.3847/1538-4357/ac06a8. arXiv: 2105.06568 [astro-ph.GA].

Madau, Piero et al. (Aug. 2014). "Cosmic Star-Formation History". In: 52, pp. 415–486. DOI: 10.1146/annurev-astro-081811-125615. arXiv: 1403.0007 [astro-ph.CO].

Magnelli, Benjamin et al. (Mar. 2020). "The ALMA Spectroscopic Survey in the HUDF: The Cosmic Dust and Gas Mass Densities in Galaxies up to z ∼ 3". In: 892.1, 66, p. 66. DOI: 10.3847/1538-4357/ab7897. arXiv: 2002.08640 [astro-ph.GA].

Mathis, J. S. et al. (Oct. 1977). "The size distribution of interstellar grains." In: 217, pp. 425–433. DOI: 10.1086/155591.

Mathis, John S. (Jan. 1997). "Composition and Size of Interstellar Dust". In: *From Stardust to Planetesimals*. Ed. by Yvonne J. Pendleton. Vol. 122. Astronomical Society of the Pacific Conference Series, p. 87.

McMullin, J. P. et al. (Oct. 2007). "CASA Architecture and Applications". In: *Astronomical Data Analysis Software and Systems XVI*. Ed. by R. A. Shaw et al. Vol. 376. Astronomical Society of the Pacific Conference Series, p. 127.

Michałowski, M. J. et al. (Nov. 2010). "Dust grain growth in the interstellar medium of 5 ¡ z ¡ 6.5 quasars". In: 522, A15, A15. DOI: 10.1051/0004-6361/201014902. arXiv: 1006.5466 [astro-ph.CO].

Nelson, Erica J. et al. (Jan. 2019). "Millimeter Mapping at z ∼ 1: Dust-obscured Bulge Building and Disk Growth". In: 870.2, 130, p. 130. DOI: 10.3847/1538-4357/aaf38a. arXiv: 1801.02647 [astro-ph.GA].

Pallottini, A. et al. (July 2022). "A survey of high-z galaxies: SERRA simulations". In: 513.4, pp. 5621–5641. DOI: 10.1093/mnras/stac1281. arXiv: 2201.02636 [astro-ph.GA].

Planck Collaboration et al. (Dec. 2011). "Planck early results. XXV. Thermal dust in nearby molecular clouds". In: 536, A25, A25. DOI: 10.1051/0004-6361/201116483. arXiv: 1101.2037 [astro-ph.GA].

Popping, Gergö et al. (Mar. 2022). "The dust-continuum size of TNG50 galaxies at z = 1-5: a comparison with the distribution of stellar light, stars, dust, and H_2". In: 510.3, pp. 3321–3334. DOI: 10.1093/mnras/stab3312. arXiv: 2101.12218 [astro-ph.GA].

Pozzi, F. et al. (Feb. 2020). "The dust mass function from z ∼0 to z ∼2.5". In: 491.4, pp. 5073–5082. DOI: 10.1093/mnras/stz2724. arXiv: 1909.11333 [astro-ph.GA].

Pozzi, F. et al. (Sept. 2021). "The ALPINE-ALMA [CII] survey. Dust mass budget in the early Universe". In: 653, A84, A84. DOI: 10.1051/0004-6361/202040258. arXiv: 2105.14789 [astro-ph.GA].

Puglisi, A. et al. (June 2019). "The Main Sequence at z ∼ 1.3 Contains a Sizable Fraction of Galaxies with Compact Star Formation Sizes: A New Population of Early Post-starbursts?" In: 877.2, L23, p. L23. DOI: 10.3847/2041-8213/ab1f92. arXiv: 1905.02958 [astro-ph.GA].

Riechers, Dominik A. et al. (Nov. 2017). "Rise of the Titans: A Dusty, Hyperluminous "870 μm Riser" Galaxy at z ∼ 6". In: 850.1, 1, p. 1. DOI: 10.3847/1538-4357/aa8ccf. arXiv: 1705.09660 [astro-ph.GA].

Rodighiero, Giulia et al. (Jan. 2023). "JWST unveils heavily obscured (active and passive) sources up to z 13". In: 518.1, pp. L19–L24. DOI: 10.1093/mnrasl/slac115. arXiv: 2208.02825 [astro-ph.GA].

Rujopakarn, W. et al. (Dec. 2016). "VLA and ALMA Imaging of Intense Galaxy-wide Star Formation in z ∼ 2 Galaxies". In: 833.1, 12, p. 12. DOI: 10.3847/0004-637X/833/1/12. arXiv: 1607.07710 [astro-ph.GA].

Rujopakarn, W. et al. (Sept. 2019). "ALMA 200 pc Resolution Imaging of Smooth Cold Dusty Disks in Typical z ∼ 3 Star-forming Galaxies". In: 882.2, 107, p. 107. DOI: 10.3847/1538-4357/ab3791. arXiv: 1904.04507 [astro-ph.GA].

Saintonge, Amélie et al. (Aug. 2022). "The Cold Interstellar Medium of Galaxies in the Local Universe". In: 60, pp. 319–361. DOI: 10.1146/annurev-astro-021022-043545. arXiv: 2202.00690 [astro-ph.GA].

Schreiber, C. et al. (Jan. 2018). "Dust temperature and mid-to-total infrared color distributions for star-forming galaxies at 0 ¡ z ¡ 4". In: 609, A30, A30. DOI: 10.1051/0004-6361/201731506. arXiv: 1710.10276 [astro-ph.GA].

Scoville, N. et al. (Sept. 2007). "The Cosmic Evolution Survey (COSMOS): Overview". In: 172.1, pp. 1–8. DOI: 10.1086/516585. arXiv: astro-ph/0612305 [astro-ph].

Sérsic, J. L. (Feb. 1963). "Influence of the atmospheric and instrumental dispersion on the brightness distribution in a galaxy". In: *Boletin de la Asociacion Argentina de Astronomia La Plata Argentina* 6, pp. 41–43.

Sommovigo, L. et al. (Sept. 2020). "Warm dust in high-z galaxies: origin and implications". In: 497.1, pp. 956–968. DOI: 10.1093/mnras/staa1959. arXiv: 2004.09528 [astro-ph.GA].

Sommovigo, L. et al. (July 2022). "The ALMA REBELS Survey: cosmic dust temperature evolution out to z 7". In: 513.3, pp. 3122–3135. DOI: 10.1093/mnras/stac302. arXiv: 2202.01227 [astro-ph.GA].

Stacey, G. J. et al. (Dec. 2010). "A 158 μm [C II] Line Survey of Galaxies at z ~1-2: An Indicator of Star Formation in the Early Universe". In: 724.2, pp. 957–974. DOI: 10.1088/0004-637X/724/2/957. arXiv: 1009.4216 [astro-ph.CO].

Talia, Margherita et al. (Mar. 2021). "Illuminating the Dark Side of Cosmic Star Formation Two Billion Years after the Big Bang". In: 909.1, 23, p. 23. DOI: 10.3847/1538-4357/abd6e3. arXiv: 2011.03051 [astro-ph.CO].

Tamura, Yoichi et al. (Mar. 2019). "Detection of the Far-infrared [O III] and Dust Emission in a Galaxy at Redshift 8.312: Early Metal Enrichment in the Heart of the Reionization Era". In: 874.1, 27, p. 27. DOI: 10.3847/1538-4357/ab0374. arXiv: 1806.04132 [astro-ph.GA].

Valiante, Rosa et al. (Sept. 2011). "The origin of the dust in high-redshift quasars: the case of SDSS J1148+5251". In: 416.3, pp. 1916–1935. DOI: 10.1111/j.1365-2966.2011.19168.x. arXiv: 1106.1418 [astro-ph.CO].

Venemans, Bram P. et al. (Dec. 2020). "Kiloparsec-scale ALMA Imaging of [C II] and Dust Continuum Emission of 27 Quasar Host Galaxies at z $\sim$ 6". In: 904.2, 130, p. 130. DOI: 10.3847/1538-4357/abc563. arXiv: 2010.14874 [astro-ph.GA].

Voigt, L. M. et al. (May 2010). "Limitations of model-fitting methods for lensing shear estimation". In: 404.1, pp. 458–467. DOI: 10.1111/j.1365-2966.2010.16300.x. arXiv: 0905.4801 [astro-ph.CO].

Walter, Fabian et al. (Mar. 2022). "ALMA 200 pc Imaging of a z 7 Quasar Reveals a Compact, Disk-like Host Galaxy". In: 927.1, 21, p. 21. DOI: 10.3847/1538-4357/ac49e8. arXiv: 2201.06396 [astro-ph.GA].

Wang, Tsan-Ming et al. (Apr. 2022). "A^{3}COSMOS: A census on the molecular gas mass and extent of main-sequence galaxies across cosmic time". In: 660, A142, A142. DOI: 10.1051/0004-6361/202142299. arXiv: 2201.12070 [astro-ph.GA].

Weiß, A. et al. (June 2007). "Highly-excited CO emission in APM 08279+5255 at z = 3.9". In: 467.3, pp. 955–969. DOI: 10.1051/0004-6361:20066117. arXiv: astro-ph/0702669 [astro-ph].

Yamasawa, Daisuke et al. (July 2011). "The Role of Dust in the Early Universe. I. Protogalaxy Evolution". In: 735.1, 44, p. 44. DOI: 10.1088/0004-637X/735/1/44. arXiv: 1104.0728 [astro-ph.GA].

Young, Monica (2020). *60-SECOND ASTRO NEWS: MATURE INFANT GALAXIES & A POSSIBLY ROGUE PLANET*. URL: https://skyandtelescope.org/astronomy-news/60-second-astronomy-news-distant-galaxies-rogue-planet/ (visited on 10/30/2020).

Younger, Joshua D. et al. (Nov. 2008). "The Physical Scale of the Far-Infrared Emission in the Most Luminous Submillimeter Galaxies". In: 688.1, pp. 59–66. DOI: 10.1086/591931. arXiv: 0807.2243 [astro-ph].

Zaroubi, Saleem (Jan. 2013). "The Epoch of Reionization". In: *The First Galaxies*. Ed. by Tommy Wiklind et al. Vol. 396. Astrophysics and Space Science Library, p. 45. DOI: 10.1007/978-3-642-32362-1_2. arXiv: 1206.0267 [astro-ph.CO].

Zhuang, Ming-Yang et al. (Aug. 2022). "The Star-forming Main Sequence of the Host Galaxies of Low-redshift Quasars". In: 934.2, 130, p. 130. DOI: 10.3847/1538-4357/ac7aaf. arXiv: 2208.01301 [astro-ph.GA].

A Additional continuum maps

In here are presented the continuum maps of the remaining continuum emitters divided in three classes: multi-component objects, resolved and point-sources.

A.1 Multi-component objects

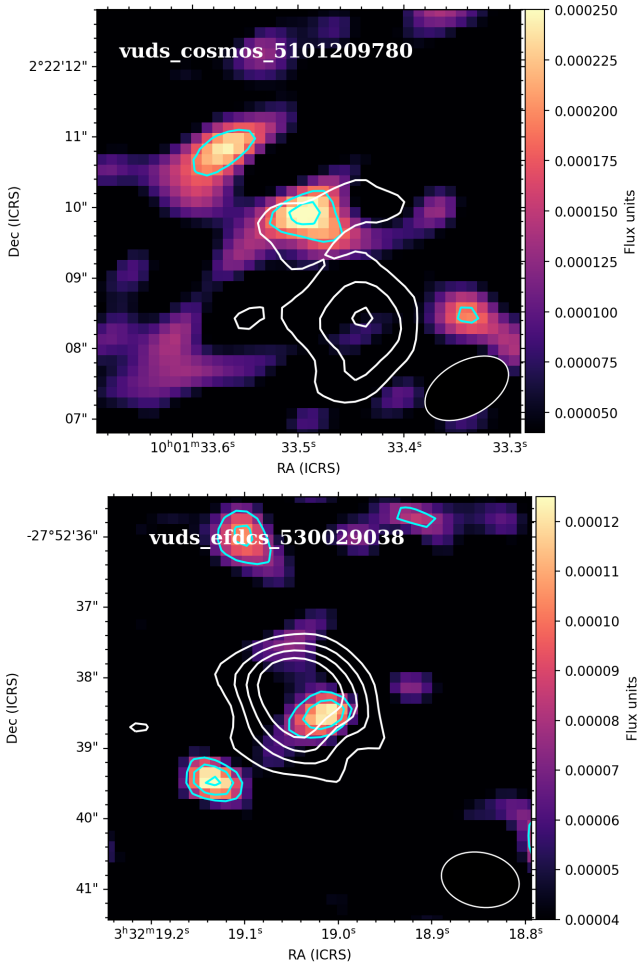

Figure 44: Continuum maps of multi-component objects, in the same contour of image 28.

A.2 Resolved

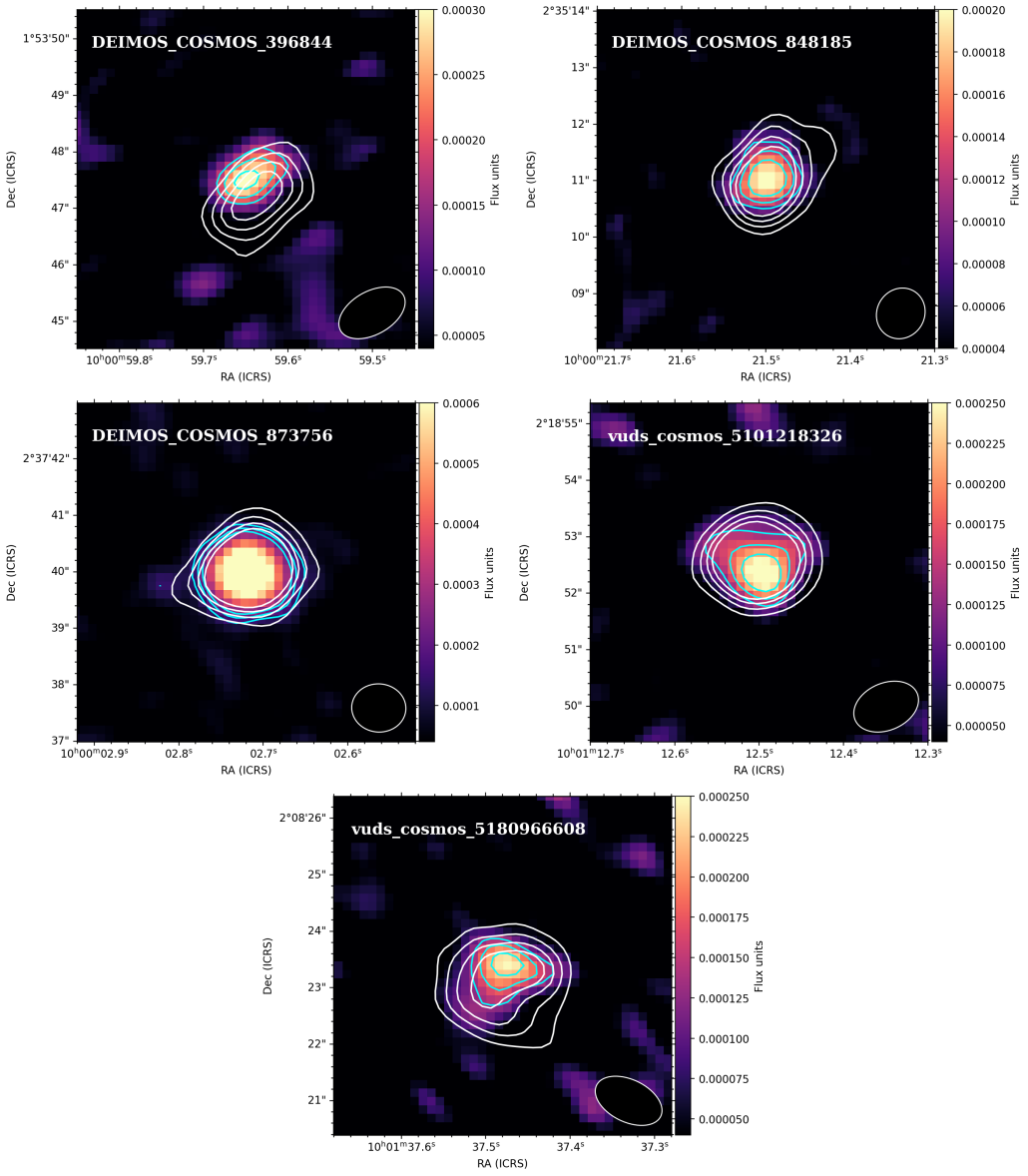

Figure 45: Continuum maps of resolved objects, in the same contour of image 28.

A.3 Point-sources

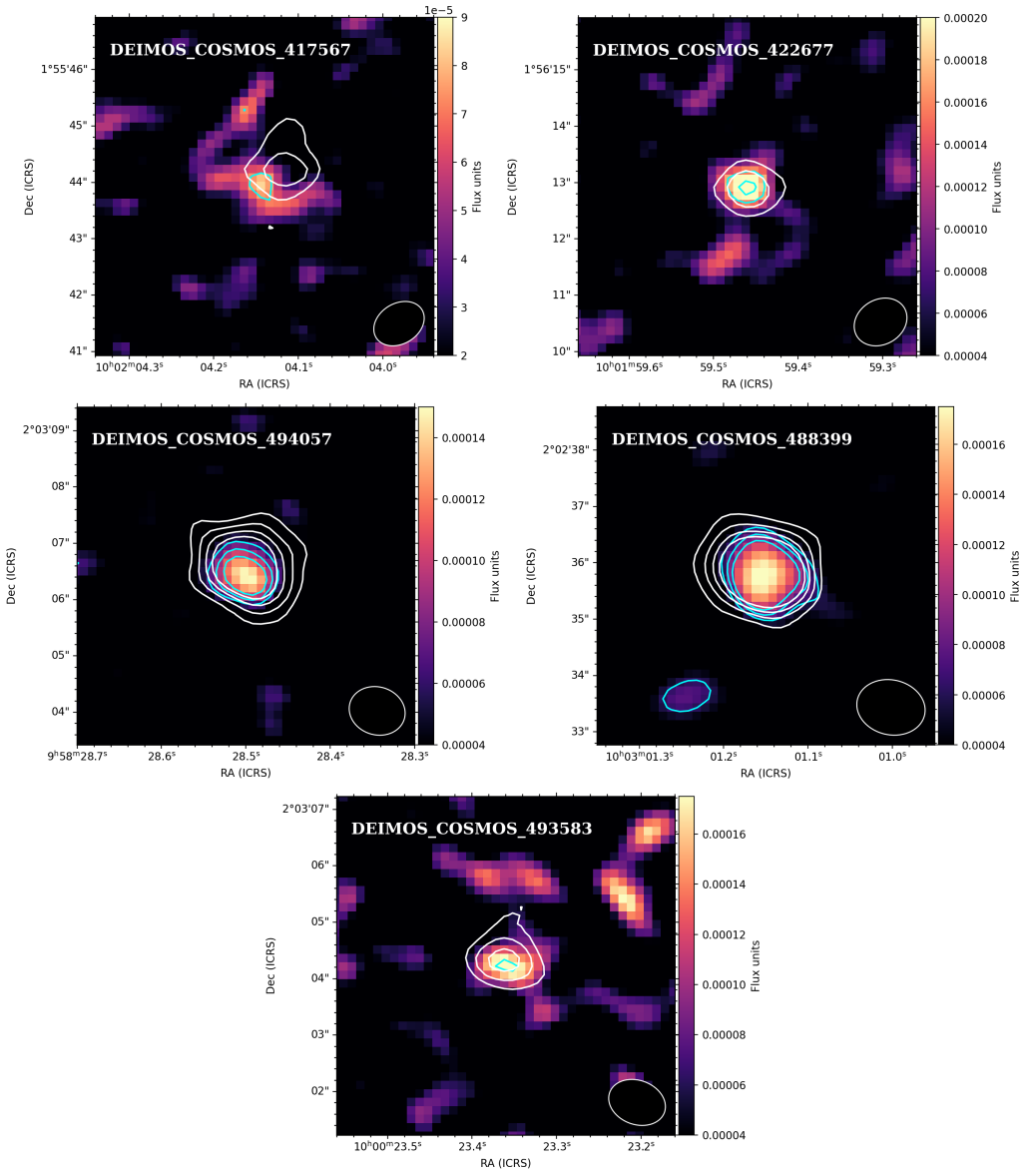

Figure 46: Continuum maps of point-sources sources, in the same contour of image 28.

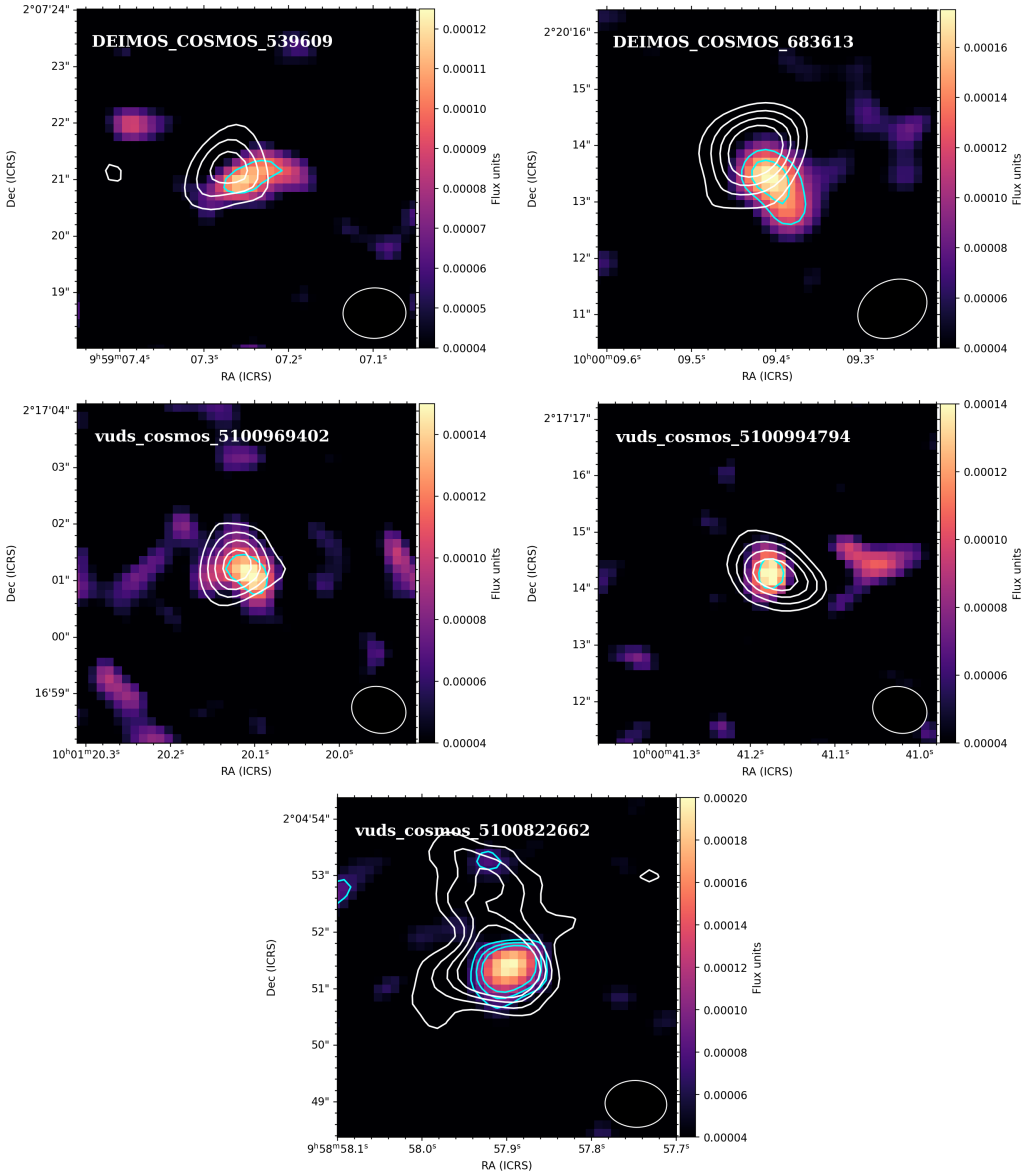

Figure 47: Continuum maps of point-sources sources, in the same contour of image 28.